DEVELOPMENT OF A MINI-PIG MODEL OF RADIATION-INDUCED BRAIN INJURY

by

Whitney Diep Perez

A Dissertation

Submitted to the Faculty of Purdue University

In Partial Fulfillment of the Requirements for the degree of

Doctor of Philosophy

School of Health Sciences

West Lafayette, Indiana

May 2022

THE PURDUE UNIVERSITY GRADUATE SCHOOL
STATEMENT OF COMMITTEE APPROVAL

Dr. Ulrike Dydak, Chair

School of Health Sciences

Dr. Keith Stantz

School of Health Sciences

Dr. Matthew Scarpelli

School of Health Sciences

Dr. Ilektra Athanasiadi

Department of Small Animal Clinical Sciences at Virginia Tech

Dr. Carlos Pérez-Torres

Academy of Integrated Science at Virginia Tech

Approved by:

Dr. Aaron Bowman

To my husband and my son

ACKNOWLEDGMENTS

It takes a village to raise a PhD student, and I would like to thank everyone that has helped to make this achievement possible. First and foremost, I would like to thank Dr. Carlos Pérez-Torres for serving as my research advisor these past four years. Your mentorship and guidance were both an indispensable part of my journey in becoming a scientist and a professional outside-the-box thinker. I would also like to express my great appreciation to the rest of my committee members: Dr. Ulrike Dydak, Dr. Keith Stantz, Dr. Ilektra Athanasiadi, and Dr. Matthew Scarpelli. Dr. Dydak, you were my first research mentor, teaching me about MRI and MATLAB before I even earned a bachelor's degree. Now, you are overseeing the final steps of my doctoral studies. Six years have passed since I was given the opportunity to work in your lab, and I will forever be thankful that you have opened the doors to MRI research for me. Dr. Stantz, thank you for encouraging me to pursue my research ideas, especially when they became far-fetched. More importantly, thank you for your professional support as I dipped my toes into the world of AAPM. Dr. Athanasiadi, this dissertation would not exist without your expertise and guidance. I am entirely grateful for our collaboration and your continued support. Dr. Scarpelli, I would like to express my thanks for joining my committee during such a late and unanticipated time.

I would also like to acknowledge the herculean task that my lab members, colleagues, and friends have taken on during these past four years as a part of my professional support network. First, I would like to give a big thanks to my fellow lab members, Dr. Daniel McIlrath and Dr. Andrew Boria. Although our lab group remained small, we made up for it in our philosophical tangents. It's been a privilege working alongside you both during our time together. I am extremely grateful for the serendipity that allowed me to cross paths with my professional colleagues, Dr. Xiaopeng Zhou, Dr. Sa Liu, and Dr. Mack Richards. Dr. Zhou, thank you for your expertise and advice during my research; it has been a pleasure working with you. Dr. Liu and Dr. Richards, thank you both for your patience and encouragement throughout my time as your teaching assistant; it has made all the difference. Last but not least, I would like to say thank you to a few special people that have supported my journey throughout these years: Pingyu Xia, Sana Tabassum, Mychaela Coyne, Xinxin Zhang, and Nicholas Farley. I would not be where I am today if not for your friendship.

Finally, I would like to express my heartfelt gratitude for the immense support of my family, particularly my husband, Mike Perez. He has been an integral part of this whole ordeal; he was at my side when I submitted my graduate school applications, when I experienced a nervous breakdown prior to my oral preliminary exam, and when I decided to take on dissertation-writing and motherhood within the same year.

TABLE OF CONTENTS

LIST OF TABLES

LIST OF FIGURES

LIST OF ABBREVIATIONS

ADC	Apparent Diffusion Coefficient
CC	Corpus Callosum
CI	Conformity Index
CT	Computed Tomography
DTI	Diffusion Tensor Imaging
DVH	Dose Volume Histogram
FA	Fractional Anisotropy
GI	Gradient Index
Glx	Glutamate + Glutamine
GM	Gray Matter
HI	Homogeneity Index
H&E	Hematoxylin and Eosin
IC	Internal Capsule
ICRU	International Commission on Radiation Units and Measurements
IHC	Immunohistochemistry
IMRT	Intensity-Modulated Radiation Therapy
LFB	Luxol Fast Blue
mI	Myo-inositol
MRI	Magnetic Resonance Imaging
MRS	Magnetic Resonance Spectroscopy
MU	Monitor Units
NAA	N-acetylaspartate
OAR	Organs at Risk
PTV	Planning Target Volume
RIBI	Radiation-Induced Brain Injury
ROI	Region of Interest
T1W	T1-Weighted
T2W	T2-Weighted
tCho	Glycerophosphocholine + Phosphocholine
tCr	Creatine + Phosphocreatine
WBRT	Whole Brain Radiotherapy
WM	White Matter

ABSTRACT

While radiation therapy is a standard treatment modality for managing primary and metastatic brain tumors, it causes irreversible and progressive long-term side effects that decrease the quality of life for pediatric brain tumor survivors. These side effects, known as radiation-induced brain injury (RIBI) and which occur at least 6 months post-treatment, create challenges in education, employment, and social relationships throughout the patients' lifetime. With the prognosis for pediatric cancer patients constantly improving, long-term side effects such as RIBI pose a major clinical problem for post-treatment care. To create and evaluate treatments for this clinical injury, it is critical to understand how this condition forms and develops. However, this cannot be done in patients due to the invasive nature of cranial biopsies. The current scientific understanding behind the pathophysiology of these late-delayed forms of RIBI is therefore built upon studies of pre-clinical animal models. Such experimental models, typically of healthy rodents, are not currently capable of accurately replicating the radiological and histological changes seen in human patients. This inconsistency limits the efficacy of preclinical discoveries when translated to clinical trials. To address this issue, we chose to establish a mini-pig model for RIBI using a standard clinical approach of radiation delivery and follow-up imaging. Our hypothesis is that cranial irradiation of the mini-pig brain will elucidate the clinical magnetic resonance imaging (MRI) signatures of RIBI, which will then correspond to characteristic changes in diffusion properties, metabolite profiles, immune constituents, and glial and neuronal cell subpopulations as evidenced by advanced MRI techniques and histopathology. As such, results from Aim 1 have highlighted not only incongruencies between rodent models and clinical findings, but also various inconsistencies in current assessment techniques of late-delayed RIBI in patients. Additionally, results from Aim 2 have established the feasibility of a mini-pig model of RIBI based on the current clinical standard of diagnosis. Finally, results from Aim 3 describe characteristic changes in diffusion properties and histological appearances as well as novel changes in metabolite concentrations within our mini-pig model late-delayed RIBI. In conclusion, this intermediate animal model of RIBI can replicate the clinical condition and may ultimately provide valuable insight into the pathophysiology of RIBI.

CHAPTER 1. INTRODUCTION

1.1 Cranial Radiation Therapy

Radiation therapy is an indispensable treatment modality for treating, managing, and preventing intracranial tumors. High-energy ionizing radiation is delivered either from a medical linear accelerator or from radioactive sources to a pre-specified, tumor-dependent treatment area within the patient's brain. Radiation delivered into a restricted volume is known as partial brain radiotherapy, while administration throughout the entire brain is called whole brain radiotherapy (WBRT) [1]. As the high-energy particles reach the target site, they induce injury either directly by causing double-stranded breaks in DNA or induce indirect damage through the formation of free radicals which then damage the DNA [2]. Due to the indiscriminate nature of both direct and indirect DNA damage, non-cancerous cells are also inevitably at risk of radiation-induced damage. This limits the amount of radiation dose that can be administered to a patient; however, a certain amount of radiation dose must be justified in order to maintain tumor control. WBRT remains an important treatment modality for brain cancer patients with aggressive or inoperable tumors, small cell lung cancer patients with multiple metastatic brain lesions, and acute lymphocytic leukemia patients that require prophylactic cranial irradiation [3,4]. Unfortunately, irradiation of such a large portion of healthy brain tissue puts the patient at risk for normal tissue damage. With the prognosis for brain tumor patients progressively improving, renewed attention has thus been placed on these long-term effects of radiation therapy due to their detrimental impact on quality of life.

1.2 Radiation-Induced Brain Injury

Normal tissue injuries caused by cranial radiation therapy typically manifest in a time-dependent manner and are thereby classified as acute, early-delayed, and late-delayed radiation-induced brain injury (RIBI) [5]. Acute RIBI occurs during or shortly after radiation treatment; patients may report symptoms of headaches, nausea, and dizziness due to increased edema and disruption of the blood-brain barrier [6,7]. Early-delayed RIBI occurs <6 months after radiation therapy; patients may report symptoms of somnolence, fatigue, and nausea due to transient demyelination and edema resorption [6]. It has been observed that acute and early-delayed RIBI resolve spontaneously or with steroid administration. Therefore, these early injuries do not have a

significant long-term impact on the patient's quality of life [8]. Lastly, late-delayed RIBI occurs >6 months post-therapy; patients may report symptoms of cognitive impairment. Although there are many reports of potential pathophysiological drivers of late-delayed RIBI, including necrosis, demyelination, vascular abnormalities, cerebral atrophy, and hippocampal injury [7,9,10], the inherent cause of such cognitive dysfunction remains unclear. Nonetheless, the irreversible and progressive nature of late-delayed RIBI creates a critical problem for post-treatment care of long-term survivors [1,6].

1.3 Magnetic Resonance Techniques to Evaluate Radiation-Induced Brain Injury

Acquisition of magnetic resonance images and spectroscopic data is one approach in overcoming the invasive nature of using biopsy samples to understand the radiation response of both the tumor and the surrounding normal tissue. Anatomical magnetic resonance images, such as pre- and post-contrast T1-weighted (T1W) images and T2-weighted (T2W) images, are acquired as part of the clinical standard of care to follow up on post-irradiation changes. Essentially, T1W images have different weightings for its acquisition parameters than T2W images, which allow for basic differences in image brightness and contrast. Because of these weighting factors, T1W and T2W images are predominantly determined by T1 and T2 properties of tissue, respectively. Together, T1W and T2W images are useful for differentiating between different types of late-delayed RIBI, such as focal and diffuse lesions.

Diffusion tensor imaging is a quantitative imaging technique that detects the Brownian motion of water protons. Within an unrestricted space or low levels of surrounding cellularity, water can diffuse in any direction. Examples of this scenario include cerebral spinal fluid or edema, in which water will have a high apparent diffusion coefficient (ADC; mm^2/s) and a low fractional anisotropy (FA) value [11]. Water within a restricted region, such as healthy white matter tracts, will have a high FA value and a low ADC. This is indicative of bidirectional diffusion and low rates of isotropic diffusion, respectively. Together, FA and ADC values are useful in characterizing the microstructural integrity of white matter since a deviation in its highly directional diffusion or low isotropic diffusion rates can be indicative of potential injury.

Proton-based magnetic resonance spectroscopy is a quantitative *in vivo* measurement technique that detects metabolite compositions within millimolar concentrations. Each metabolite is detected at different and particular frequencies due to dissimilarities in their local chemical

environments [12]. Examples of detectable metabolites within the brain include N-acetylaspartate (NAA), choline-containing compounds (tCho), creatine-containing compounds (tCr), glutamate and glutamine (Glx), and myo-inositol (mI). Respectively, these metabolites can be used as markers for neuronal density or function (NAA), cellular proliferation (tCho), energy metabolism (tCr), excitatory neurotransmission (Glx), and glial cell density (mI) [13]. Together, changes in these metabolites can serve as specific markers of late-delayed RIBI.

MRI, DTI, and MRS each involve unique capabilities to noninvasively visualize and quantify *in vivo* changes within the brain. These imaging modalities have therefore been extensively used in countless post-treatment studies for both humans and rodents. Such studies are further described in Chapter 2.

1.3 Specific Aims

The overall purpose of this dissertation is to formally address the discrepancies between the evidence produced by current rodent models of late-delayed RIBI and the observations recorded in human studies of late-delayed RIBI. Specifically, Chapter 2 establishes similarities and dissimilarities between humans and rodents after cranial radiation therapy through a systematic review of the literature. Chapter 3 describes the preliminary development of a pre-clinical model of late-delayed RIBI using mini-pigs. Chapter 4 provides a characterization of said mini-pig model using clinically translatable noninvasive imaging and measurement techniques. The corresponding aims for these chapters are provided below, respectively:

Aim 1: To determine the accuracy of current rodent models of late-delayed radiation-induced brain injury with respect to the data derived from human patients at least 6 months post-treatment.

Aim 2: To establish the feasibility of a mini-pig model of late-delayed radiation-induced brain injury based on the current clinical standard of diagnosis.

Aim 3: To examine characteristic changes in diffusion properties, metabolite concentrations, and histological appearances within our mini-pig model late-delayed radiation-induced brain injury.

1.4 References

1. Lee Y-W, Cho H-J, Lee W-H, Sonntag WE. Whole Brain Radiation-Induced Cognitive Impairment: Pathophysiological Mechanisms and Therapeutic Targets. Biomolecules and Therapeutics. 2012;20:357–70.

2. Baskar R, Dai J, Wenlong N, Yeo R, Yeoh K-W. Biological response of cancer cells to radiation treatment. Front Mol Biosci [Internet]. 2014 [cited 2022 Mar 11];1. Available from: http://journal.frontiersin.org/article/10.3389/fmolb.2014.00024/abstract

3. Gaspar LE, Prabhu RS, Hdeib A, McCracken DJ, Lasker GF, McDermott MW, et al. Congress of Neurological Surgeons Systematic Review and Evidence-Based Guidelines on the Role of Whole Brain Radiation Therapy in Adults With Newly Diagnosed Metastatic Brain Tumors. Neurosurg. 2019;84:E159–62.

4. Mehta MP. The controversy surrounding the use of whole-brain radiotherapy in brain metastases patients. Neuro-Oncology. 2015;17:919–23.

5. Tofilon PJ, Fike JR. The Radioresponse of the Central Nervous System: A Dynamic Process. Radiation Research. 2000;153:357–70.

6. Durand T, Bernier M-O, Léger I, Taillia H, Noël G, Psimaras D, et al. Cognitive outcome after radiotherapy in brain tumor. Current Opinion in Oncology. 2015;27:510–5.

7. Walker AJ, Ruzevick J, Malayeri AA, Rigamonti D, Lim M, Redmond KJ, et al. Postradiation imaging changes in the CNS: how can we differentiate between treatment effect and disease progression? Future Oncology. 2014;10:1277–97.

8. Greene-Schloesser D, Robbins ME, Peiffer AM, Shaw EG, Wheeler KT, Chan MD. Radiation-induced brain injury: A review. Front Oncol [Internet]. 2012 [cited 2022 Mar 11];2. Available from: http://journal.frontiersin.org/article/10.3389/fonc.2012.00073/abstract

9. Dietrich J, Monje M, Wefel J, Meyers C. Clinical Patterns and Biological Correlates of Cognitive Dysfunction Associated with Cancer Therapy. The Oncologist. 2008;13:1285–95.

10. Sundgren PC. MR Spectroscopy in Radiation Injury. AJNR Am J Neuroradiol. 2009;30:1469–76.

11. Le Bihan D, van Zijl P. From the diffusion coefficient to the diffusion tensor. NMR Biomed. 2002;15:431–4.

12. van der Graaf M. In vivo magnetic resonance spectroscopy: basic methodology and clinical applications. Eur Biophys J. 2010;39:527–40.

13. Rae CD. A Guide to the Metabolic Pathways and Function of Metabolites Observed in Human Brain 1H Magnetic Resonance Spectra. Neurochem Res. 2014;39:1–36.

CHAPTER 2. NEUROCOGNITIVE AND RADIOLOGICAL CHANGES AFTER CRANIAL RADIATION THERAPY IN HUMANS AND RODENTS: A SYSTEMATIC REVIEW

A version of this chapter has been accepted for publication in *The International Journal of Radiation Biology* and is currently awaiting online publication as of the submission of this dissertation chapter.

2.1 Introduction

Radiation therapy is a practical and critical tool to manage intracranial tumors due to its ability to non-invasively treat cases of metastatic or deeply seated brain tumors [1]. As high-energy radiation particles are delivered to the tumor site, a fraction of this energy will inevitably be deposited within the healthy brain tissue along the radiation beam's path and immediately adjacent to the tumor. As a consequence of normal tissue irradiation, many patients undergoing cranial radiation therapy experience neurological side effects. Indeed, long-term side effects of cranial irradiation have been reported to occur in 50%-90% of adult patients [2] and up to 50% of pediatric patients [3]. It has been shown that these radiation-induced brain injuries ultimately lead to a decrease in quality of life after cancer therapy [4,5]. The prognosis and severity of these side effects, however, depends on the time of clinical expression and are therefore generally categorized as acute, early-delayed, and late-delayed brain injury [2]. The acute and early-delayed effects, which usually occurs from a few days up to 6 months after irradiation, are transient and typically self-resolve. Late-delayed radiation effects, which usually occurs from 6 months up to an indefinite number of years after therapy, do not self-resolve. Due to increasing survival outcomes for brain tumor patients [6], and thus a growing population of long-term survivors, this late-delayed form of radiation induced-brain injury (RIBI) is the primary concern in terms of radiation-induced neurotoxicity.

Depending in part on the radiotherapy treatment paradigm, late-delayed RIBI can present as a focal or diffuse pathology [7,8]. Radiation necrosis presents as a focal lesion with increased vascular permeability and edema on magnetic resonance imaging (MRI) [9]. The cognitive dysfunctions associated with radiation necrosis include seizures, focal weakness, language impairment, and blurred vision [10,11]. Although radiation necrosis maintains high clinical relevance within late-delayed effects of RIBI, it is not the primary focus of this review as its

incidence is usually small (roughly 5%). The more common form of RIBI presents as a diffuse lesion characterized by a homogeneous enhancement throughout the subcortical white matter without increased vascular permeability or edema [12]. The cognitive impairments associated with this form of RIBI include, but are not limited to, deficits in attention, memory, executive functioning, language, and psychomotor skills [13,14]. Other diffuse radiological abnormalities such as cerebral volume loss, cerebral microbleeds, changes in white matter diffusion metrics, and changes in the neurometabolic profile have also been suggested to be associated with the aforementioned cognitive impairments [15–17].

The current scientific understanding behind the pathophysiology of these late-delayed forms of RIBI is built upon studies of pre-clinical animal models. Results of these experimental models, typically of healthy rodents, have revealed a multitude of dynamic processes within rodent brains after the delivery of radiation. These include, but are not limited to, the impairment of hippocampal neurogenesis [18–20], loss of neuronal function [21–23], depletion of oligodendrocyte progenitor cells [21,23], chronic neuroinflammation [1,21,24], and damage to microvascular endothelium [25,26]. However, it remains unclear how these biological mechanisms underlie the clinical and radiological presentations of late-delayed RIBI.

While the field of RIBI research has provided a wealth of literature on patient outcomes and animal modeling, it is important to evaluate how these findings fit together to form a complete understanding of RIBI development. The objective of this systematic review of the literature is to first establish an interdisciplinary understanding of the current clinical evidence of RIBI, and then confirm rodent model accuracy with respect to current clinical end points. Therefore, the three key questions we have set out to answer in this systematic review are:

1) What are the current cognitive and radiological assessments used to evaluate late-delayed RIBI?;

2) What are the relationships between and within cognitive and radiological findings of late-delayed RIBI in humans?; and

3) How well do rodent models of RIBI replicate to the cognitive and radiological evidence observed in humans?

2.2 Methods

2.2.1 Search strategy

This systematic review adheres to the guidelines described in the Preferred Reporting Items for Systematic Reviews and Meta-Analyses (PRISMA) Statement [27]. The initial pool of studies pertaining to clinically or radiologically detected radiation injury of the brain in humans or rodents were first collected through PubMed, Web of Science, and Scopus using the search string listed in Appendix A. The search criteria were further limited by language (English), time of publication (January 1980 to January 2022), and publication status (full text must be available). Case reports, editorials without original data, and review articles were further excluded from the pool of initial studies. Additional studies were included into this pool by manually hand-searching references of included studies.

2.2.2 Study selection

A preliminary screening of the titles and abstracts was performed based on the following inclusion criteria: (1) patients must be treated with cranial radiation therapy; (2) rodent models must receive a clinically relevant dose of ionizing radiation to a disease-free brain; (3) outcome is measured by a neurocognitive or neuroimaging assessment after a specified period of time post-irradiation: at least 1 month for rodents and 6 months for patients; (4) neurocognitive assessments must evaluate global cognitive functioning or one of the following domains: complex attention, executive functioning, learning and memory, perceptual-motor function, and language; (5) neuroimaging techniques must attempt to identify at least one of the following radiation-induced changes: cerebral atrophy, cerebral microbleeds, radiation-induced leukoencephalopathy, changes in diffusion metrics, and changes in metabolic profile. Respectively, these criteria function to (1) establish patient data as the ground truth; (2) verify deficits or lesions within rodent brains are exclusively due to a radiation-induced normal tissue injury; (3) ensure that the deficits or lesions measured are indeed late-delayed effects and not acute effects of RIBI; (4) limit neurocognitive outcomes to the domains in which impairments are most commonly reported; (5) limit neuroimaging outcomes to those previously reported to be associated with neurocognitive impairment.

This limitation in neurocognitive and neuroimaging outcomes was performed due to the wide range of possible albeit infrequent side effects that could potentially occur after radiation treatment. Neurocognitive assessments therefore focused on changes in the domains of language, executive function, learning and memory, complex attention, perceptual-motor function, and general cognitive ability according to previously reported guidelines [28,29]. Furthermore, neuroimaging outcomes are focused on those that have been shown to be related to neurocognitive impairment, such as cerebral atrophy, cerebral microbleeds, radiation-induced leukoencephalopathy, changes in diffusion metrics, and changes in metabolic profile [16,30,31]. All evidence and definitions of neurocognitive or radiological RIBI have been left to the interpretation of the original authors.

Accepted studies based on this title and abstract screening were retrieved and saved to Zotero, our reference management database of choice. The full text of these studies was then read to ensure quality of study methodology and to confirm adherence to inclusion criteria.

2.2.3 Data extraction and analysis

Data was extracted from the studies that fulfilled the inclusion and exclusion criteria. Details of study characteristics were extracted, which included species, age, sex, sample size, health status, irradiated volume, total dose, and dose per fraction. Details of the relevant findings were extracted, which included outcome measurement techniques, time of outcome detection, and classification of outcome. For studies that contain groups with an experimental treatment arm, only the group that has received solely radiation is considered for this review. Some studies may set forth the objective of measuring both cognitive and radiological RIBI, however fail to find evidence of either one or the other; only the successfully detected form of RIBI will be incorporated as evidence in this review. Studies that do not provide the techniques for cognitive or radiological RIBI assessment will not be considered in our results. These collected data were then organized and combined according to the authors' categorization of evidence (cognitive or radiological RIBI, rodent or human) in order to visualize their relationships and diversity [32].

2.3 Results

2.3.1 Description of search results

The literature search identified a total of 2,647 studies. After the removal of duplicates, 1,722 studies remained. Abstract screening based on the inclusion criteria excluded 1,562 studies, leaving a remaining total of 158 studies to undergo full-text assessment. Five studies were excluded due to either insufficient evidence of RIBI or omission of RIBI assessment protocols, leaving a final group of 153 studies included in this systematic review. A summary of this systematic search of the literature, as well as the enumeration of included studies, is provided in Fig 1. The comprehensive collection of details extracted from these studies, such as patient demographics and treatment protocols, can be found in Table A.1 (for human studies) and Table A.2 (for rodent studies).

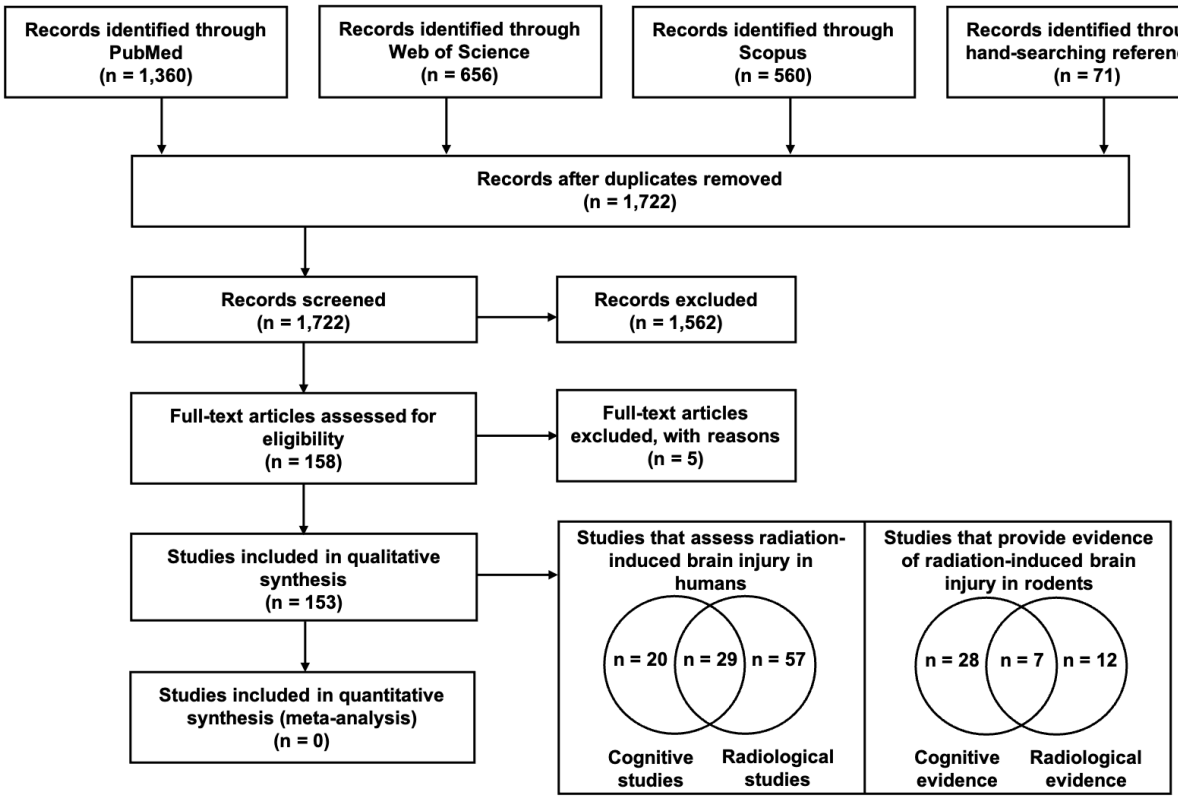

Figure 1. PRISMA flowchart for the identification and selection of studies.

2.3.2 It is unclear whether the various relationships between domains of cognitive impairment in human studies reflect ground truth or research interests

We found a total of 49 studies that sought to investigate cognitive RIBI within a human cohort. The following trends were found in patients receiving cranial radiation therapy: 1) impaired cognitive functioning occurs in the domains of complex attention [5,33–53], learning and memory [5,33,35,37–40,43,44,51,52,54–61], executive function [5,38–40,42,42,43,46,47,49–52], perceptual-motor function [5,39,49–51,62], or language [39,43,56,63,64]; 2) reduced aptitude occurs for general cognitive abilities such as academic achievement, intellectual ability, and neurocognitive functioning [4,33–36,38,40–43,45–48,52,54,65–76]; and 3) cognitive impairment does not occur in isolation, but rather spans across multiple cognitive domains.

Within this pool of 49 studies, there were 120 cumulative attempts to measure cognitive domain deficits after cranial radiotherapy. Only 94 of these 120 efforts were successful; the majority of viable evidence lies within the domains of complex attention, learning and memory, and general cognitive ability, while the minority lies within executive function, language, and perceptual-motor function (Fig 2a). Interestingly, some studies that attempt to comprehensively assess multiple cognitive domains detected little to no forms of cognitive impairment from their battery of assessments [44,77–80]. Other comprehensive studies had more success in measuring cognitive impairments and were able to detect deficits using at least half of their battery of assessments [43,46,49]. Pooling together these 94 cases of successfully detected deficits, about 90% of the current viable evidence of cognitive impairment in human studies are composed of changes in general cognitive ability, complex attention, learning and memory, or executive function with little consideration for the assessment of language and perceptual-motor function (Fig 2b). Furthermore, it can be observed that these 94 cases of cognitive deficits do not occur in isolation, but rather encompasses multiple domains (Fig 2c). Studies that show cognitive deficits occurring in a single domain did not attempt to measure changes in any other cognitive domains. This is relevant for all isolated cases of general cognitive ability but excludes one case of memory and learning and one case of complex attention.

While there is a multitude of evidence for the impairment of cognitive domains, these results differ due to their heterogeneity of assessments (Fig 3). In our dataset, for example, we find that 24% of all human cognitive impairments are related to complex attention, which are measured by 9 different types of assessments. Even if these deficits in cognition are summarized and

categorized into domains, the type of assessment used to detect injury only provides a fraction of the overall answer. For instance, Correa et al. uses the Digit Span test to measure selective attention while Edelmann et al. uses the Grooved Pegboard test to measure processing speed. These measurements of selective attention and processing speed both fall under the category of complex attention, but they describe different aspects of the attention domain. Although we can picture general relationships about the types of cognitive RIBI cases and their interconnections, we cannot be sure whether these trends represent the inherent characteristics of RIBI or are rather a reflection of the field's vested interest in particular RIBI subcategories.

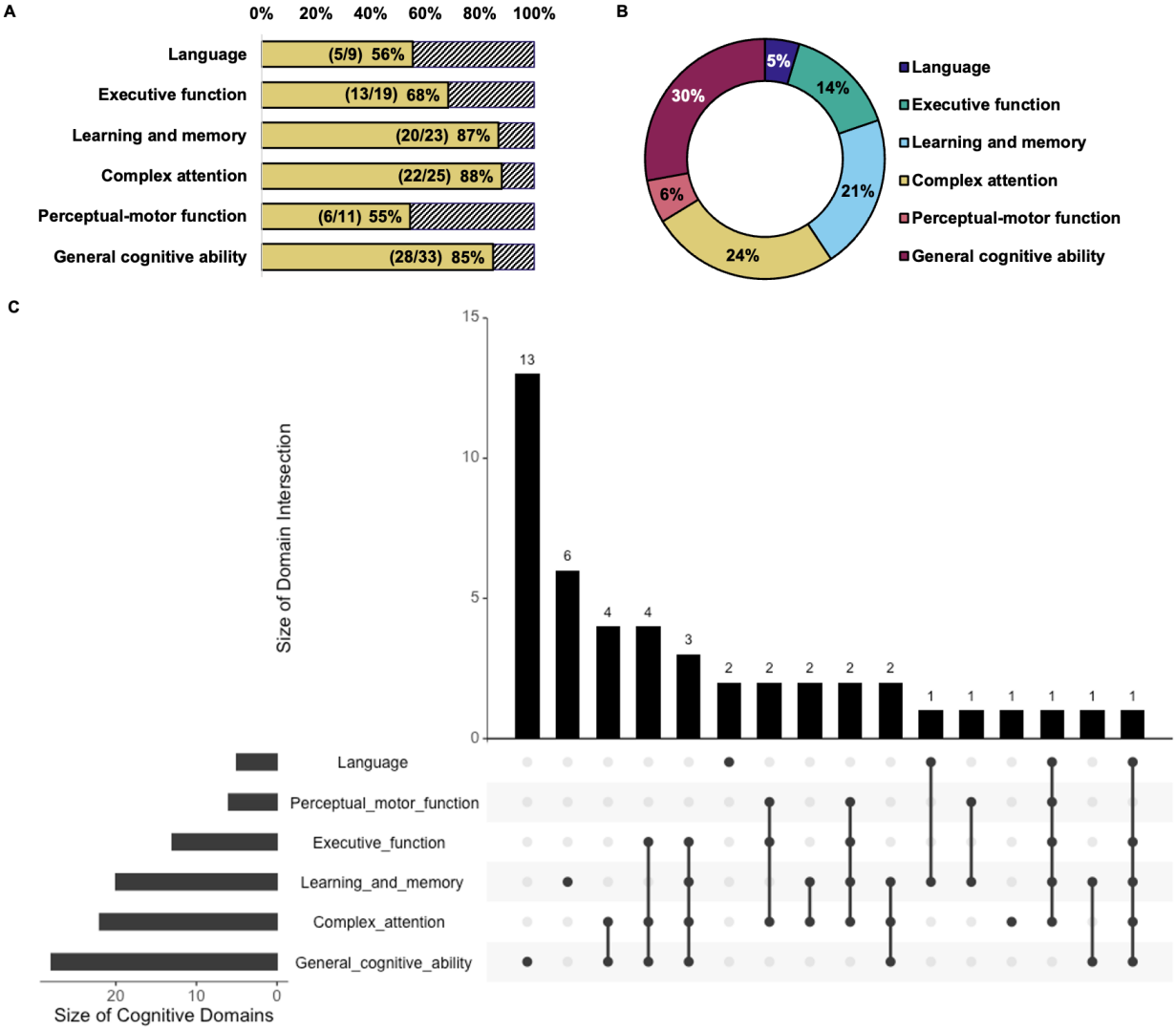

Figure 2. Current evidence on radiation-induced cognitive impairment in human studies. (a) Number of attempts and success rate for specific cognitive deficits associated with brain irradiation. Each domain-specific success rate is determined by comparing the number of cases that successfully detects cognitive deficits within its respective domain to the number of cases that sought out with the objective of detecting cognitive deficits within its respective domain. Studies may have multiple cases of domain-specific cognitive deficits. (b) Domain-specific prevalence rates as determined by comparing the number of cases that successfully detects cognitive deficits within its respective domain to the number of cases that successfully detects cognitive deficits for all domains. (c) Interaction between cognitive domains. The 'Size of Domain Intersection' enumerates the studies that present evidence of their respective combination of cognitive deficit cases. The 'Size of Cognitive Domains' enumerates the successfully detected cases of cognitive deficits within its respective domain.

Figure 3. Assessments performed in human studies to measure changes in cognition after cranial radiotherapy. Illustrated in each subfigure are techniques that successfully detected changes in cognition for the domains of: (a) language, (b) executive function, (c) learning and memory, (d) complex attention, (e) perceptual-motor function, (f) general cognitive ability.

2.3.3 Trends can be easily deduced from human studies of MRI-detectable radiation injuries due to the generality of neuroimaging techniques

We found a total of 86 studies that sought to investigate radiological RIBI within a single human cohort. The following trends were found in patients receiving cranial radiation therapy: 1) changes in diffusion present as decreases in fractional anisotropy and increases in mean diffusivity, longitudinal diffusivity, or perpendicular diffusivity within global white matter (WM) or WM regions such as the fornix, cingulum bundle, corpus callosum, uncinate fasciculus, ventral cingulum, genu, and splenium [38,40,42,43,56,62,69,73,79,81–92]; 2) the majority of cerebral atrophy studies measure the change in WM volumes, which are shown to decrease post-irradiation [33–39,57,64,67,76,93–96]; 3) the total number of cerebral microbleeds detected within a patient increases with time after cranial irradiation [61,92,97–101]; 4) WM hyperintensities, also known as leukoencephalopathy, localizes within the periventricular regions of the brain [40,41,68,102–105]; and 5) a loss of neuronal density and/or function, reflected by a decrease in N-acetylaspartate normalized to creatine (NAA/Cr) in MR spectroscopy (MRS) [39,75,84,93,106–110].

Further studies provide findings of radiological RIBI development that do not fit within these trends. One of such observations is that while many studies suggest cerebral atrophy mainly affects the loss of WM volume, other studies describe cerebral atrophy as a loss of cortical thickness [111,112], a reduction of gray matter volume [89,113,114], or a decrease in whole brain volume without a change in WM volume [115]. Furthermore, one study reports that there was no significant difference in cerebral volume between the patients and controls over time [78]. Another observation pertains to the conflicting evidence in the permanence of microbleeds. Indeed, it has been shown that microbleeds may disappear during clinical follow-up [92,103] or that microbleeds could be detected at all follow-up examinations upon appearance [61,98,100]. Finally, there are still discrepancies in establishing a clinically feasible metabolic characteristic for RIBI. As previously mentioned, many MRS studies show that NAA/Cr decreases after cranial irradiation with the assumption that Cr remains stable over time. Due to a limited number of studies, however, the change in Cr has yet to be determined. A handful of studies show that it decreases within the irradiated brain [106,109], however it is uncertain whether this is due to increasing age or irradiation. Due to a limited number of studies, the change in myoinositol normalized to creatine has yet to be determined. However, one study [107] shows that it increases within the irradiated brain. Due to conflicting results, the effect of choline normalized to creatine remains inconclusive.

Indeed, studies have reported increases [107], decreases [75,106,108], or no changes [67,84,93,110] in choline normalized to creatine post-irradiation.

Within this pool of 86 studies, there were 109 cumulative attempts to measure MRI-detectable changes after cranial radiotherapy from which 103 were successful in detecting radiation-induced changes (Fig 4a). Pooling together these 103 cases of successfully detected lesions, about 90% of the current viable evidence of MRI-detectable injuries in human studies are composed of changes in cerebral atrophy, cerebral microbleeds, leukoencephalopathy, changes in diffusion metrics with minor evidence for the assessment of changes in metabolite profile (Fig 4b). Furthermore, the relationships between different forms of radiological RIBI are more discrete than cognitive RIBI: most of these cases of radiologically detected lesions occur in isolation (Fig 4c). The studies in which these radiological lesions are shown to occur by themselves did not attempt to measure other MRI-detectable changes.

While there is a multitude of evidence for radiological RIBI, these results do not differ as much in the heterogeneity of assessments compared to cognitive RIBI (Fig 5). In our dataset, for example, we find that 27% of all radiologically detected lesions in humans are related to cerebral atrophy, which are measured by 9 different types of assessments. However, these variations in assessment types are different from those used for cognitive RIBI. The assessment types for radiological RIBI differ by level of detail provided compared to assessment types for cognitive RIBI. For instance, 25% of cerebral atrophy studies used only T1-weighted imaging while 21% used a combination of T1-weighted, T2-weighted, and proton density images. Volume loss will still be measured in these two circumstances, regardless of which combination of MRI protocols is used. The difference, however, is that the accuracy ascribed to cerebral volume loss is strengthened as more techniques are used. In other words, the different types of cognitive RIBI assessments measures different aspects of cognitive domain impairment while different types of radiological RIBI assessments measure the same result with different levels of exactness. While we can form a general deduction about the types of radiological RIBI cases (Fig 4b) and connections of radiological RIBI (Fig 4c), firm numerical end points cannot be concluded for all aforementioned studies due to discrepancies in study methodology and data presentation.

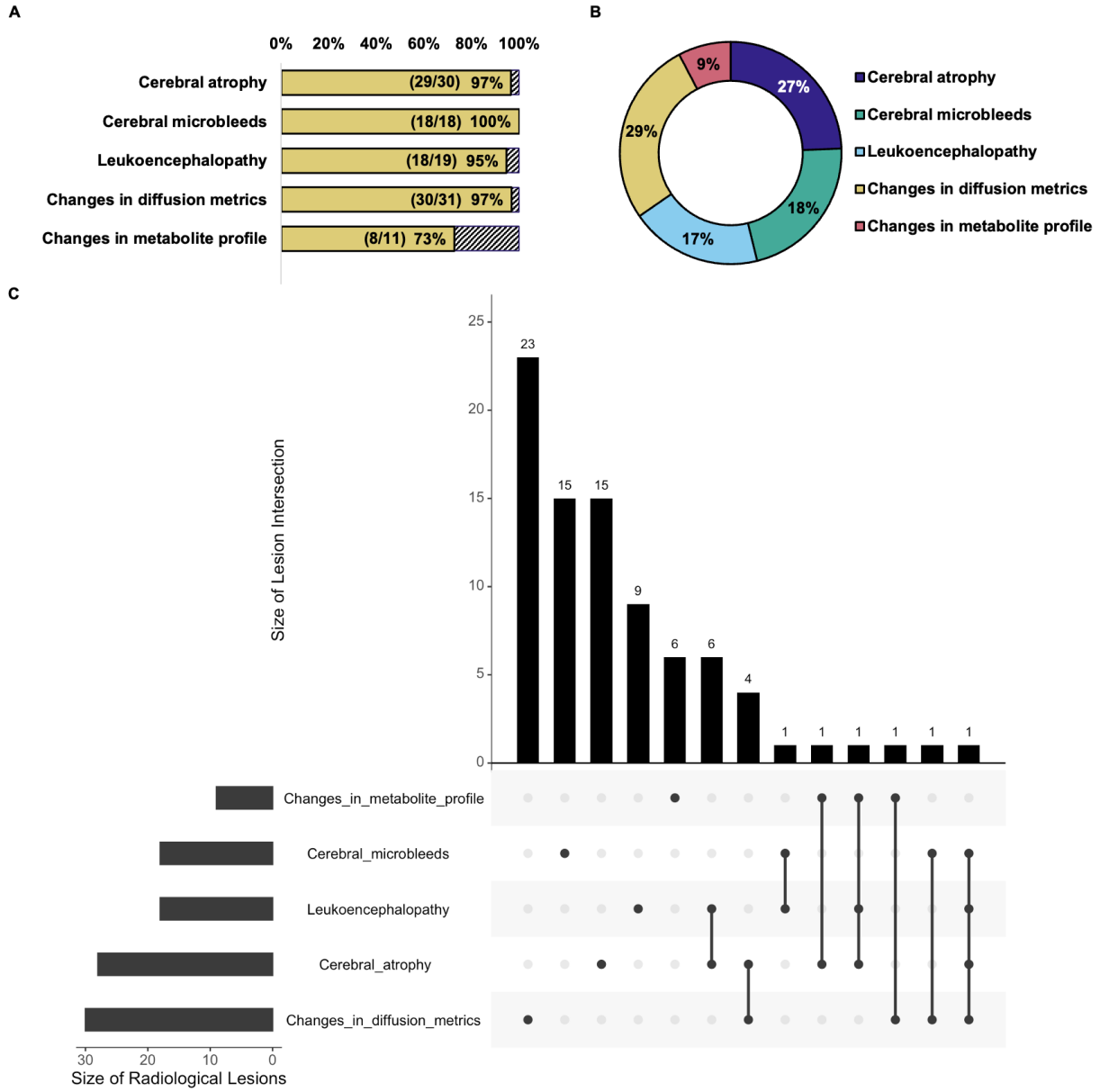

Figure 4. Current evidence on radiation-induced abnormalities as detected by magnetic resonance imaging in human studies. (a) Number of attempts and success rate for specific radiological lesions associated with brain irradiation. Each lesion-specific success rate is determined by comparing the number of cases that successfully detected its respective radiological lesion to the number of cases that sought out with the objective of detecting its respective radiological lesion. Studies may have multiple cases of radiologically detected lesions. (b) Lesion prevalence rates as determined by comparing the number of cases for each successfully detected radiological lesion to the number of cases for all successfully detected radiological lesions. (c) Interaction between types of radiological lesions. The 'Size of Lesion Intersection' enumerates the studies that present evidence of their respective combination of radiologically detected cases. The 'Size of Radiological Lesions' enumerates the successfully detected cases of the respective radiologically detected lesions.

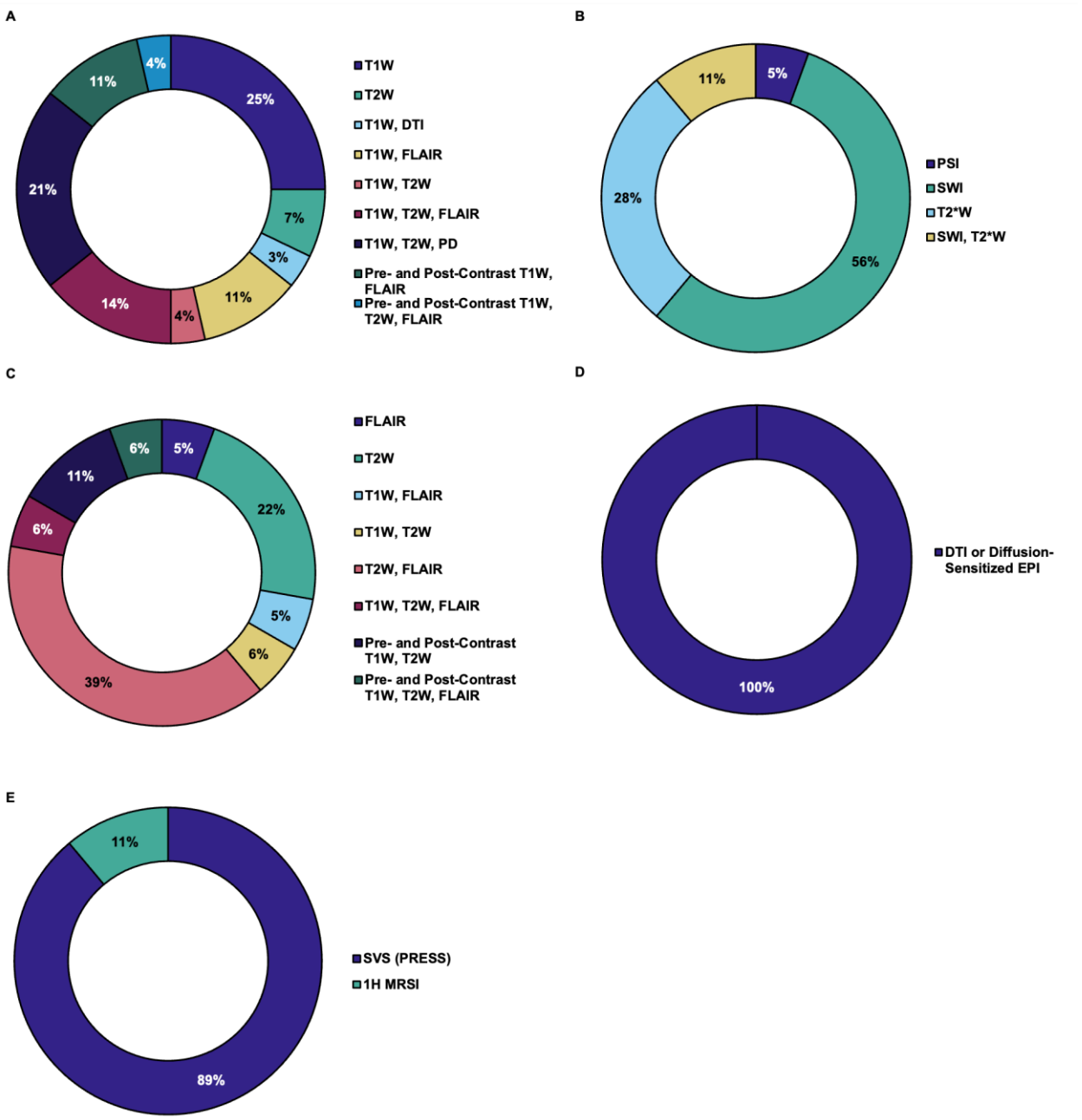

Figure 5. Magnetic resonance imaging techniques performed in human studies to detect lesions after cranial radiotherapy. Illustrated in each subfigure are techniques that successfully detected lesion types such as: (a) cerebral atrophy, (b) cerebral microbleeds, (c) leukoencephalopathy, (d) changes in diffusion metrics, (e) changes in metabolic profile.

2.3.4 There is an association between cognitive and radiological radiation-induced brain injury, but their causative relationship remains unclear

We found a total of 29 studies that provided evidence of both cognitive and radiological RIBI within a single human cohort. The design, evidence type, and results of each study are provided in Table A.3. The following relationships between radiological lesions and cognitive impairments were found in these patients that underwent cranial radiation therapy: 1) loss of intracranial volume is associated with poor cognitive status [33–36,38,40,49,50,57,59,67,76]; 2) abnormalities in diffusion imaging is associated with poor cognitive status [38,40,42–44,56,59,62,64,69,73]; 3) WM hyperintensities (leukoencephalopathy) are associated with poor cognitive status [5,40,49,67]; and 4) cerebral microbleeds are associated with cognitive decline [40,51,61].

While these general relationships have been elucidated, it is imperative to also consider other findings of cognitive and radiological RIBI development from the systematic review that do not fit within these trends. While there is evidence that cerebral microbleeds are associated with worse cognitive function, three other similar studies included in this systematic review report that there were no clinical or neurocognitive symptoms related to cerebral microbleeds [77,99,116]. For leukoencephalopathy, the study by Aoyama et al. reports that only patients with severe white matter injury show clinically meaningful signs of cognitive deterioration. However, this cognitive outcome was assessed using the mini-mental state examination, which is not as sensitive towards post-treatment changes in cognition compared to comprehensive neuropsychological tests [14]. Most importantly, many of these studies do not investigate the temporal relationship between cognitive and radiological RIBI. There are four studies that focus on teasing apart this temporal relationship by describing it from an imaging biomarker perspective, showing that changes in diffusion metrics precede and predict cognitive outcomes [44,56,59,69]. However, one study provides evidence that white matter hyperintensities precede the onset of cognitive decline over a period of 6 years post-irradiation [37]. Due to a lack of further evidence on the temporal relationship between cognitive and radiological RIBI, in addition to a lack of large studies with well-designed methodologies, there remains to be a consensus on whether radiologically detected injuries develop in tandem, precede, or follow cognitive impairment.

While many components of cognitive and radiological RIBI have been shown to be interconnected, there are certain relationships that draw more interest from the research field than

others. A large proportion of evidence on the association between cognitive and radiological RIBI stems from cerebral atrophy and its relationship to the domain of complex attention (Fig 6a). However, this trend may not be reflective of the true etiology of RIBI. That is, these number of papers may also reflect the research field's current interest in studying cerebral atrophy and its relationship to different cognitive domains. Similar thinking can be applied to other types of radiological RIBI, such as radiation-induced leukoencephalopathy and changes in diffusion metrics, and their respective relationships with cognitive outcomes. Upon controlling for collaborative groups, a change in distribution of associations between cognitive and radiological RIBI can be found; interestingly, the largest proportion now stems from changes in diffusion metrics and its relationship to the domain of learning and memory (Fig 6b). However, the inherent issue of inhomogeneous assessments of the connection between cognitive and radiological RIBI still remains, making it unclear whether one relationship is inherently more important than the other. Therefore, further comprehensive assessment of the cognitive and radiological RIBI relationship is needed to elucidate their role in causation of neurological deterioration.

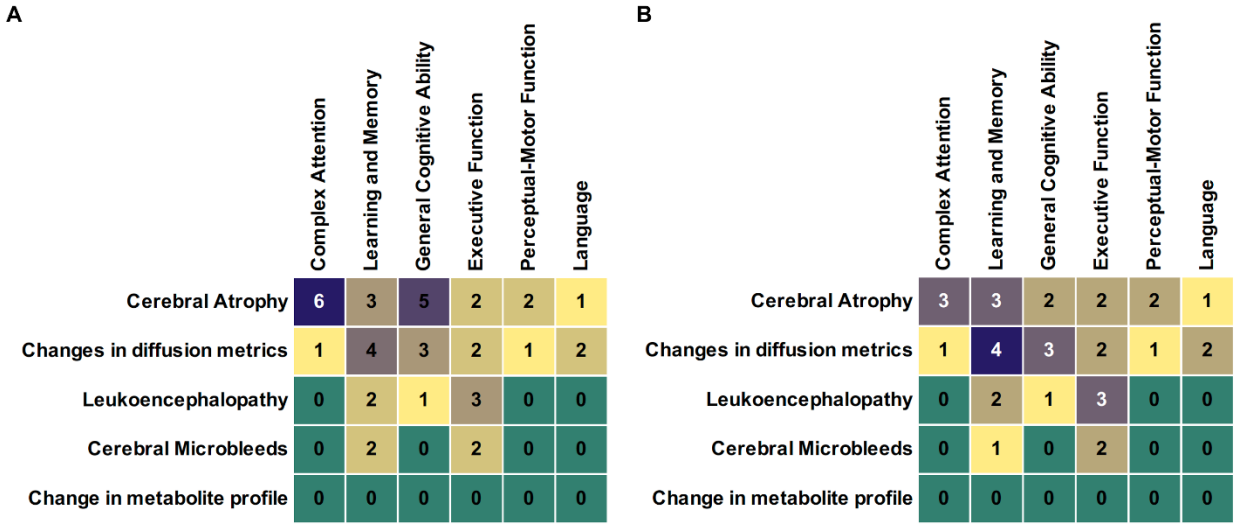

Figure 6. Associations between human studies containing evidence of both cognitive and radiological radiation-induced brain injuries. Number of (a) studies and (b) research groups that have shown both cognitive and radiological RIBI in the same cohort. Dark blue values indicate a higher number of studies with respect to the entire distribution while teal values indicate a lower number of studies.

2.3.5 Clinical findings are not fully represented in rodent models

We found a total of 35 studies that provided evidence of cognitive RIBI within a rodent sample. These rodent studies exclusively reflect either learning and memory [117–149] or executive function [150,151]; they do not replicate the interconnection of cognitive impairments measured in humans (Fig 7a). Much like in the human studies, a variety of behavioral assays are used to evaluate impairment in hippocampal-dependent learning and memory (Fig 7b). While this cognitive domain is found to be impaired in human patients, there is a clear mismatch between the focus of cognitive assessment in human studies versus rodent studies (Fig 7c). Similar to the issues that emerged in human studies, it is unclear whether these trends are a result of either 1) the true characteristic of cognitive impairment in rodents, or 2) the inherent interests of researchers modeling cognitive RIBI in humans. In other words, it is uncertain whether our findings originate from the assumption that either 1) rodent brains can only produce hippocampal-dependent learning and memory impairments post-irradiation, or 2) rodent brains produce hippocampal-dependent learning and memory impairments post-irradiation because that is the only area of injury that we are measuring. As at least one group has found non-hippocampal-dependent cognitive deficits in rodent RIBI models, the latter assumption is more likely than the former.

We found a total of 19 studies that provided evidence of radiological RIBI within a rodent sample. These rodent studies identified radiologically detectable lesions such as changes in metabolite profile [123,142,152–158], cerebral atrophy [136,148–151,155,159,160], and changes in diffusion metrics [150,151,155,161–163]; the majority of these lesions are detected in isolation (Fig 8a). Furthermore, although the imaging techniques used to detect these changes are similar to the protocols used for humans (Fig 8b), the distribution of MRI-detectable lesions in rodent models do not fully reflect the human injury (Fig 8c). While neuroimaging studies of successful models of cognition show evidence of cerebral atrophy using anatomical MRI [136,155,159,160] and DTI techniques [148,150,151], there are currently no rodent models that provide evidence of radiation-induced leukoencephalopathy after undergoing similar neuroimaging protocols as RIBI patients. Likewise, there are no studies that perform neuroimaging protocols to detect cerebral microbleeds within the rodent brain, likely due to the increased susceptibility artifacts when scanning rodent brains. With respect to rodent models measuring microstructural and metabolic changes, evidence is limited in number and remains inconclusive. While some rodent models show a post-treatment decrease in FA, others show FA remain unchanged post-treatment [136,148,150,152] despite the

occurrence of other cognitive changes within the same cohort. Furthermore, while there is evidence of metabolic-related changes in rodent brains, the evidence contains many discrepancies. Neuroimaging assessments in models of cognition show conflicting evidence of metabolic changes within the rodent brain post-irradiation. NAA/Cr has been shown to increase [123,152], decrease [142,153,154,156–158], or have no change post-irradiation [124]. Glutamate and glutamine normalized to creatine have been shown to increase [123], decrease [142,158], or have no change post-irradiation [124,154]. Choline normalized to creatine has been shown to increase [158], decrease [153,157], or have no change post-irradiation [154,156]. Myoinositol normalized to creatine has been shown to increase [156,158], decrease [123,152], or have no change [124] post-irradiation.

We found 7 studies that provided evidence of both cognitive and radiological RIBI within a rodent sample. The design, evidence type, and results of each study are presented in Table A.4. Two studies describe the relationship between changes in executive functioning and diffusion metrics within rodents [150,151] while the other five studies present the connection between learning and memory impairments and either cerebral atrophy [136,148,149] or changes in metabolite profile [123,142]. While these rodent studies have successfully detected cognitive and radiological changes post-irradiation, the current rodent models of RIBI do not holistically replicate the research findings currently exhibited in human cases.

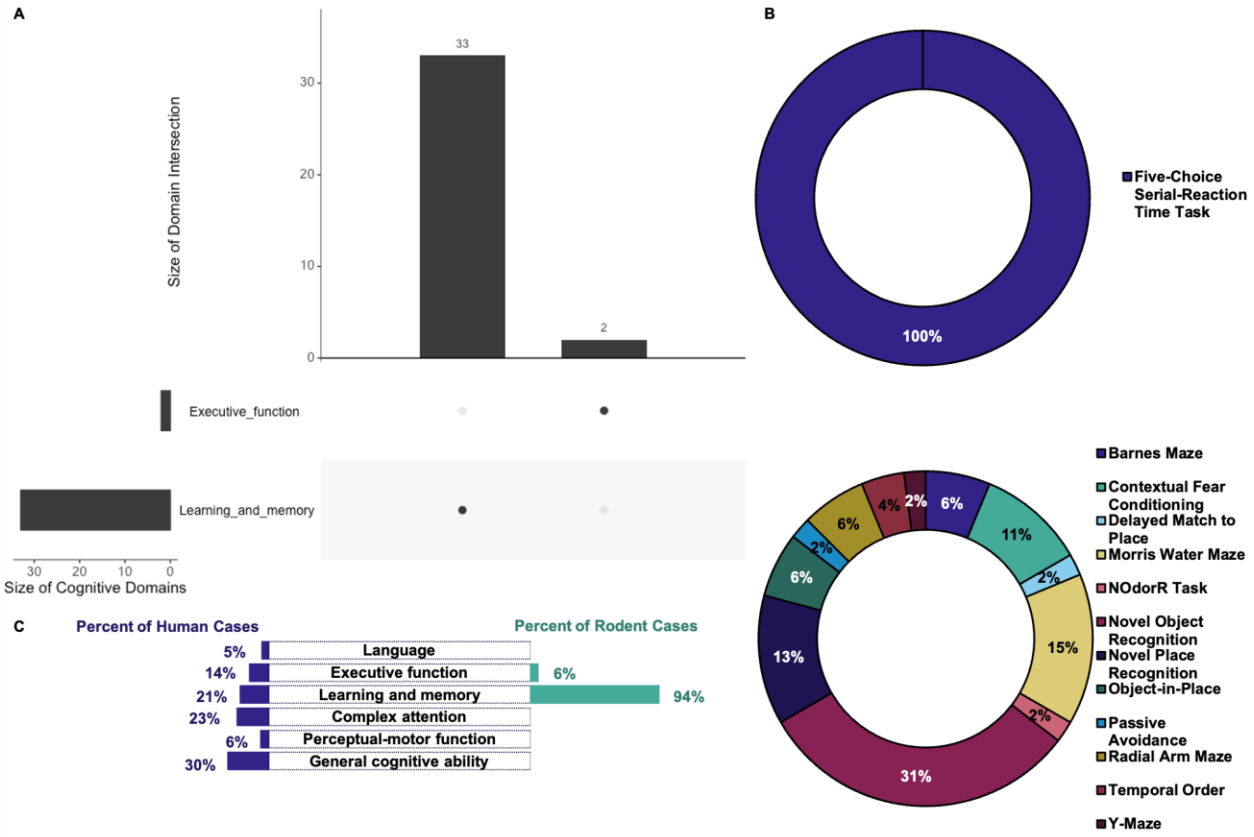

Figure 7. Current evidence on radiation-induced cognitive impairment in rodent studies. (a) Interaction between cognitive domains. The 'Size of Domain Intersection' enumerates the studies that present evidence of their respective combination of cognitive deficit cases. The 'Size of Cognitive Domains' enumerates the successfully detected cases of cognitive deficits within its respective domain. (b) Techniques that successfully detected changes in cognition for the domains of (top) executive function and (bottom) learning and memory. (c) Distribution of cognitive domains assessed in rodents and humans after brain irradiation.

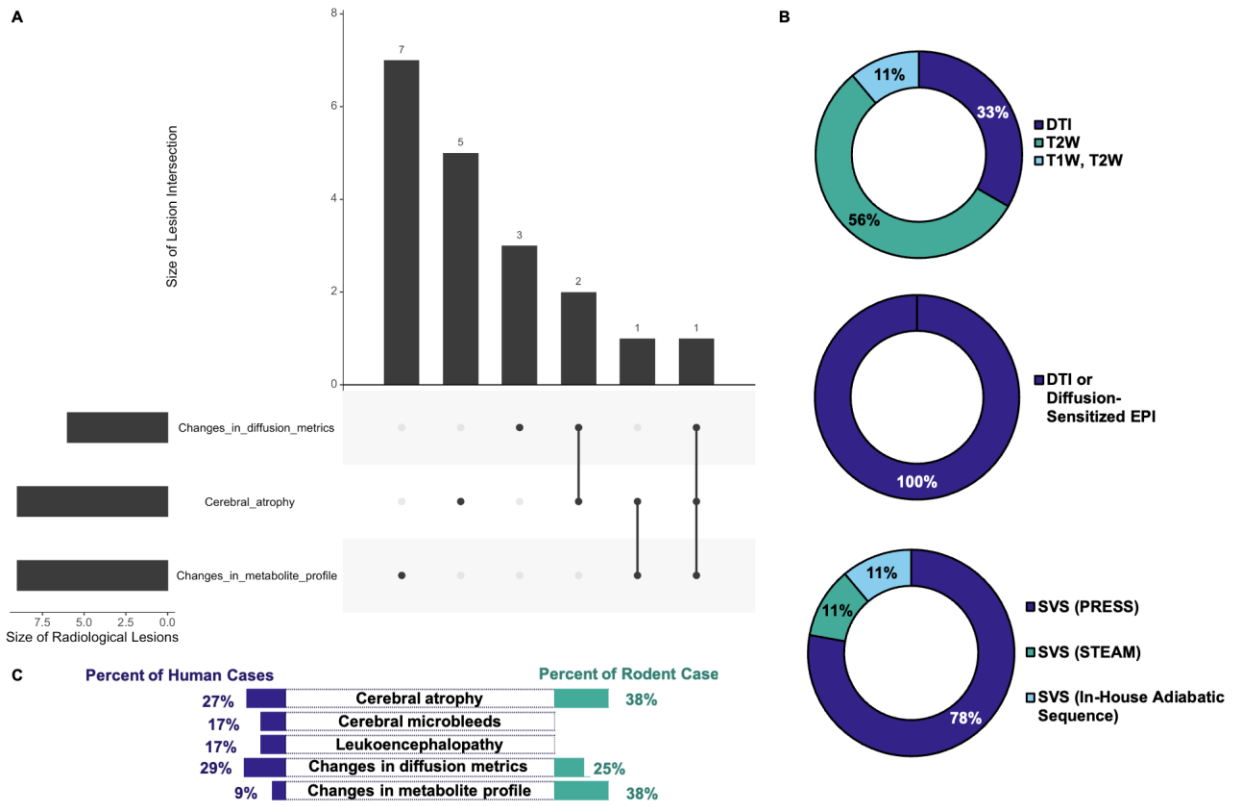

Figure 8. Current evidence on radiation-induced lesions detectable by magnetic resonance imaging in rodent studies. (a) Interaction between types of radiological lesions. The 'Size of Lesion Intersection' enumerates the studies that present evidence of their respective combination of radiologically detected cases. The 'Size of Radiological Lesions' enumerates the successfully detected cases of the respective radiologically detected lesions. (b) Techniques that successfully detected changes in (top) cerebral atrophy, (middle) diffusion metrics, and (bottom) metabolite profile. (c) Distribution of radiological lesions assessed in rodents and humans after brain irradiation.

2.4 Discussion

This systematic review of the literature was conducted to evaluate the characteristics of current late-delayed RIBI studies, elucidate the connections between cognitive and radiological forms of late-delayed RIBI, and report the accuracy of current rodent models. Regarding the features of human cognitive RIBI, there are many attempts to measure deficits within the domains of general cognitive ability, complex attention, or learning and memory. In comparison, there are not as many attempts to measure changes in language, perceptual-motor function, or executive function. Additionally, the success rate of cognitive domain deficit detection generally reflects the number of attempts to measure cognitive domain deficits. That is, the domain deficits that

contribute the entirety of cognitive RIBI consist of those that are more widely sought out to assessed, such as general cognitive ability and complex attention. Regarding the features of human radiological RIBI, there are many attempts to measure cerebral atrophy, cerebral microbleeds, leukoencephalopathy, and changes in diffusion metrics. However, there are not as many attempts to measure changes in metabolite profile. Additionally, each type of radiological lesion has a perfect success rate except for cerebral atrophy.

With respect to the trends between cognitive and radiological RIBI, our results show that there is a high distribution of studies that focus on the association between cerebral atrophy and complex attention. However, certain associations between cognitive domain deficits (e.g., perceptual-motor function and language) and radiologically detected lesions (e.g., leukoencephalopathy, cerebral microbleeds, and changes in metabolite profile) remain largely undefined. It is thus unclear whether these trends are due to implicit relationships between cognitive and radiological RIBI or to predispositions in research interests.

Incongruency is further reflected in the current preclinical models of RIBI. Results from rodent studies show that there are a limited number of models that have successfully replicated characteristics of cognitive and radiological RIBI as it would occur in a human. In the case of cognitive impairment, it is shown in this review that most rodent models of cognition replicate hippocampal-dependent learning and memory — only one of the many aspects of human cognitive impairment. Further consideration of cognitive assessments performed in rodent studies suggests that the high number of results for hippocampal-dependent memory impairment may be driven by a lack of comprehensive assays in rodent models of RIBI. Additionally, results from rodent models of neuroimaging are not completely consistent with what is observed in humans. Most of the evidence for radiological RIBI in rodents is derived from cases of cerebral atrophy and changes in metabolite profile, with a minor contribution from changes in diffusion metrics. While these radiological lesions are also present in humans, there is no current evidence that rodents are capable of exhibiting further characteristic lesions observed in humans, such as radiation-induced leukoencephalopathy and cerebral microbleeds. However, the lack of cerebral microbleed detection may be driven by a lack of MR techniques and hardware compatible with small animals.

The primary limitation of our systematic review is a lack of quantitative analysis of our results. However, a meta-analysis could not be performed due to the heterogeneity of study methodology and data presentation. There was a wide variety of study designs, patient

demographics, outcome measurement techniques, and follow-up times after treatment. In some studies, particular components of methodology were completely omitted. Furthermore, other study characteristics such as irradiated volume, total dose, number of treatment fractions, and raw outcome scores were not consistently provided within the methods. Regarding heterogeneity in the presentation of data, many human studies with mixed patient demographics (e.g., mixed treatment cohorts of radiotherapy only and radiotherapy with chemotherapy) present results in an unstratified manner such that it was difficult to deduce which side effects were derived from radiotherapy. Additionally, some studies reported wide ranges of outcome measurement (e.g., 6-60 months post-treatment) without stratification of results in regard to its specific time point of presentation. Due to these challenges in combining and comparing the collected data in a systematic fashion, it became clear that a meta-analysis would not provide an accurate insight into the current data.

A limitation of our qualitative analysis of the literature is that patient demographics, irradiated volume, and radiation dose were not considered in the analysis of late-delayed effects of RIBI. This is because treatment effects were not given with respect to patient age or sex, but rather as an entire cohort. Additionally, there were high variations in treatment protocols, which are unique to the patient's disease presentation and progression. For these reasons, the late-delayed effects of RIBI were investigated holistically based on the evidence made available by a systematic review of the literature. Additionally, we do not know how many inconclusive or negative findings have been discovered but not published. It is also possible that other studies concerning the late-delayed effects of RIBI in humans and rodents were published but were not within the scope of our search strategy.

Evidence from our review shows that rodent models are limited in replicating the multitude of cognitive impairments observed in humans due to constraints in the availability of verified cognitive assessments. A suggestion would be to consider the use of alternative cognitive assessments for rodent models that have been performed outside the field of RIBI. For instance, rodent studies of space radiation-induced cognitive impairment have successfully modeled metacognitive and hypothesis-generating tasks that were previously assumed to be primate-specific [164]. Aside from rodent models, intermediate animal models may also have the potential to replicate human outcomes. Notably, non-human primates [165–167], swine [168], and dogs [169] have been shown to be feasible large animal models of RIBI. Overall, it may be ideal to

consider either alternative cognitive assessments for rodent models or different model systems in order to replicate the human characteristics of cognitive and radiological RIBI more closely.

An additional suggestion for future research is to create a protocol of standardized assessments in order to maintain reproducible results in multi-center clinical trials of RIBI therapeutics. Our systematic review shows there are many successful methods to assess impairment within a neurocognitive domain: 5 different tests identified language impairment, 9 for executive function, 13 for learning and memory, 9 for complex attention, 6 for perceptual-motor function, and 11 for general cognitive ability. While this diversity in assessment type allows for different facets of cognitive impairment to be measured and analyzed, it also creates issues in maintaining consistency within the field of RIBI. Along with standardization, it is also important that these assessments accommodate the practicalities of clinical follow-up procedures. For instance, these evaluations should be simple without sacrificing sensitivity and able to be quickly performed by non-specialists [170].

Lastly, it is important to begin incorporating the use of more advanced MRI techniques in human studies of RIBI, such as functional MRI [171] and functional connectivity [172]. As noted above, cognitive deficits have been identified in rodent space radiation models at doses much lower than those explored for RIBI. These deficits are believed to occur without overt structural changes. Similarly, some rodent RIBI reports indicate cognitive deficits without corresponding structural changes [173,174]. However, as we noted in our section regarding the relationship between cognitive and radiological deficits, no human study of RIBI that has evaluated both cognitive and radiological changes have found cognitive deficits without corresponding radiological changes. There are multiple possible explanations for this discrepancy between human cases and rodent models. But if thought is that the cognitive deficits that characterize RIBI are due to functional changes that precede the structural changes, then the use of functional imaging can help make that clearer. Together, the use of more sensitive imaging techniques and standardized neurocognitive assessments would provide a greatly needed holistic approach to understanding the complete spectrum of late-delayed RIBI in brain cancer survivors.

2.5 Conclusions

In summary, the associations between and within cognitive and radiological RIBI often rely on the type of assessment chosen to detect it. Indeed, inhomogeneous assessments of RIBI

subcomponents can result in inhomogeneous manifestations of RIBI subcomponents. This theme of heterogeneity eventually pervades into preclinical animal modeling, creating rodent studies that assay only certain subcomponents of RIBI. Rather than placing consideration for only certain subcomponents of RIBI, perhaps it is just as important to evaluate the totality of known effects to realize the full consequence of RIBI.

2.6 Acknowledgements

This publication was made possible, in part, thanks to financial support from the Ralph W. and Grace M. Showalter Research Trust at Purdue University.

2.7 References

1. Lee Y-W, Cho H-J, Lee W-H, Sonntag WE. Whole Brain Radiation-Induced Cognitive Impairment: Pathophysiological Mechanisms and Therapeutic Targets. Biomolecules and Therapeutics. 2012;20:357–70.

2. Greene-Schloesser D, Robbins ME. Radiation-induced cognitive impairment-from bench to bedside. Neuro-Oncology. 2012;14:iv37–44.

3. Ajithkumar T, Price S, Horan G, Burke A, Jefferies S. Prevention of radiotherapy-induced neurocognitive dysfunction in survivors of paediatric brain tumours: the potential role of modern imaging and radiotherapy techniques. The Lancet Oncology. 2017;18:e91–100.

4. Corn BW, Moughan J, Knisely JPS, Fox SW, Chakravarti A, Yung WKA, et al. Prospective Evaluation of Quality of Life and Neurocognitive Effects in Patients With Multiple Brain Metastases Receiving Whole-Brain Radiotherapy With or Without Thalidomide on Radiation Therapy Oncology Group (RTOG) Trial 0118. International Journal of Radiation Oncology*Biology*Physics. 2008;71:71–8.

5. Correa DD, Shi W, Abrey LE, DeAngelis LM, Omuro AM, Deutsch MB, et al. Cognitive functions in primary CNS lymphoma after single or combined modality regimens. Neuro-Oncology. 2012;14:101–8.

6. Siegel RL, Miller KD, Jemal A. Cancer statistics, 2018: Cancer Statistics, 2018. CA: A Cancer Journal for Clinicians. 2018;68:7–30.

7. Valk PE, Dillon WP. Radiation Injury of the Brain. 1991;18.

8. Soussain C, Ricard D, Fike JR, Mazeron J-J, Psimaras D, Delattre J-Y. CNS complications of radiotherapy and chemotherapy. The Lancet. 2009;374:1639–51.

9. Vellayappan B, Tan CL, Yong C, Khor LK, Koh WY, Yeo TT, et al. Diagnosis and Management of Radiation Necrosis in Patients With Brain Metastases. Front Oncol. 2018;8:395.

10. Giglio P, Gilbert MR. Cerebral Radiation Necrosis. The Neurologist. 2003;9:180–8.

11. Diaz AZ, Choi M. Radiation-Associated Toxicities in the Treatment of High-Grade Gliomas. Seminars in Oncology. 2014;41:532–40.

12. Zhong X, Huang B, Feng J, Yang W, Liu H. Delayed leukoencephalopathy of non-small cell lung cancer patients with brain metastases underwent whole brain radiation therapy. J Neurooncol. 2015;125:177–81.

13. Sundgren PC, Cao Y. Brain Irradiation: Effects on Normal Brain Parenchyma and Radiation Injury. Neuroimaging Clinics of North America. 2009;19:657–68.

14. Cramer CK, Cummings TL, Andrews RN, Strowd R, Rapp SR, Shaw EG, et al. Treatment of Radiation-Induced Cognitive Decline in Adult Brain Tumor Patients. Curr Treat Options in Oncol. 2019;20:42.

15. Kłos J, van Laar PJ, Sinnige PF, Enting RH, Kramer MCA, van der Weide HL, et al. Quantifying effects of radiotherapy-induced microvascular injury; review of established and emerging brain MRI techniques. Radiotherapy and Oncology. 2019;140:41–53.

16. Robbins ME, Brunso-Bechtold JK, Peiffer AM, Tsien CI, Bailey JE, Marks LB. Imaging Radiation-Induced Normal Tissue Injury. Radiation Research. 2012;177:449–66.

17. Haller S, Vernooij MW, Kuijer JPA, Larsson E-M, Jäger HR, Barkhof F. Cerebral Microbleeds: Imaging and Clinical Significance. Radiology. 2018;287:11–28.

18. Dietrich J, Monje M, Wefel J, Meyers C. Clinical Patterns and Biological Correlates of Cognitive Dysfunction Associated with Cancer Therapy. The Oncol. 2008;13:1285–95.

19. Capilla-Gonzalez V, Bonsu JM, Redmond KJ, Garcia-Verdugo JM, Quiñones-Hinojosa A. Implications of irradiating the subventricular zone stem cell niche. Stem Cell Research. 2016;16:387–96.

20. Fike JR, Rosi S, Limoli CL. Neural Precursor Cells and Central Nervous System Radiation Sensitivity. Seminars in Radiation Oncology. 2009;19:122–32.

21. Burns TC, Awad AJ, Li MD, Grant GA. Radiation-induced brain injury: low-hanging fruit for neuroregeneration. FOC. 2016;40:E3.

22. Wilke C, Grosshans D, Duman J, Brown P, Li J. Radiation-induced cognitive toxicity: pathophysiology and interventions to reduce toxicity in adults. Neuro-Oncology. 2018;20:597–607.

23. Greene-Schloesser D, Moore E, Robbins ME. Molecular Pathways: Radiation-Induced Cognitive Impairment. Clinical Cancer Research. 2013;19:2294–300.

24. Lumniczky K, Szatmári T, Sáfrány G. Ionizing Radiation-Induced Immune and Inflammatory Reactions in the Brain. Front Immunol [Internet]. 2017 [cited 2018 Sep 17];8. Available from: https://www.ncbi.nlm.nih.gov/pmc/articles/PMC5418235/

25. Kim JH, Brown SL, Jenrow KA, Ryu S. Mechanisms of radiation-induced brain toxicity and implications for future clinical trials. J Neurooncol. 2008;87:279–86.

26. Warrington JP, Ashpole N, Csiszar A, Lee YW, Ungvari Z, Sonntag WE. Whole Brain Radiation-Induced Vascular Cognitive Impairment: Mechanisms and Implications. J Vasc Res. 2013;50:445–57.

27. Moher D, Liberati A, Tetzlaff J, Altman DG, for the PRISMA Group. Preferred reporting items for systematic reviews and meta-analyses: the PRISMA statement. BMJ. 2009;339:b2535–b2535.

28. Sachdev PS, Blacker D, Blazer DG, Ganguli M, Jeste DV, Paulsen JS, et al. Classifying neurocognitive disorders: the DSM-5 approach. Nat Rev Neurol. 2014;10:634–42.

29. Janss AJ, Mazewski C, Patterson B. Guidelines for Treatment and Monitoring of Adult Survivors of Pediatric Brain Tumors. Curr Treat Options in Oncol. 2019;20:10.

30. Lupo JM, Nelson SJ. Advanced Magnetic Resonance Imaging Methods for Planning and Monitoring Radiation Therapy in Patients With High-Grade Glioma. Seminars in Radiation Oncology. 2014;24:248–58.

31. Greene-Schloesser D, Robbins ME, Peiffer AM, Shaw EG, Wheeler KT, Chan MD. Radiation-induced brain injury: A review. Frontiers in Oncology [Internet]. 2012 [cited 2018 Apr 14];2. Available from: http://journal.frontiersin.org/article/10.3389/fonc.2012.00073/abstract

32. Lex A, Gehlenborg N, Strobelt H, Vuillemot R, Pfister H. UpSet: Visualization of Intersecting Sets. IEEE Trans Visual Comput Graphics. 2014;20:1983–92.

33. Mulhern RK, Palmer SL, Reddick WE, Glass JO, Kun LE, Taylor J, et al. Risks of Young Age for Selected Neurocognitive Deficits in Medulloblastoma Are Associated With White Matter Loss. JCO. 2001;19:472–9.

34. Mulhern RK, Merchant TE, Gajjar A, Reddick WE, Kun LE. Late neurocognitive sequelae in survivors of brain tumours in childhood. The Lancet Oncology. 2004;5:399–408.

35. Reddick WE, White HA, Glass JO, Wheeler GC, Thompson SJ, Gajjar A, et al. Developmental model relating white matter volume to neurocognitive deficits in pediatric brain tumor survivors. Cancer. 2003;97:2512–9.

36. Reddick WE, Taghipour DJ, Glass JO, Ashford J, Xiong X, Wu S, et al. Prognostic factors that increase the risk for reduced white matter volumes and deficits in attention and learning for survivors of childhood cancers: Reduced WMV in Childhood Cancer Survivors. Pediatr Blood Cancer. 2014;61:1074–9.

37. Armstrong CL, Hunter JV, Ledakis GE, Cohen B, Tallent EM, Goldstein BH, et al. CME Late cognitive and radiographic changes related to radiotherapy. 2002;10.

38. Edelmann MN, Krull KR, Liu W, Glass JO, Ji Q, Ogg RJ, et al. Diffusion tensor imaging and neurocognition in survivors of childhood acute lymphoblastic leukaemia. Brain. 2014;137:2973–83.

39. Follin C, Erfurth EM, Johansson A, Lätt J, Sundgren PC, Österberg K, et al. Impaired brain metabolism and neurocognitive function in childhood leukemia survivors despite complete hormone supplementation in adulthood. Psychoneuroendocrinology. 2016;73:157–65.

40. Bompaire F, Lahutte M, Buffat S, Soussain C, Ardisson AE, Terziev R, et al. New insights in radiation-induced leukoencephalopathy: a prospective cross-sectional study. Supportive Care in Cancer. 2018;26:4217–26.

41. Moretti R, Torre P, Antonello RM, Cattaruzza T, Cazzato G, Bava A, et al. Neuropsychological evaluation of late-onset post-radiotherapy encephalopathy: a comparison with vascular dementia. Journal of the Neurological Sciences. 2005;229–230:195–200.

42. Schuitema I, Deprez S, Van Hecke W, Daams M, Uyttebroeck A, Sunaert S, et al. Accelerated Aging, Decreased White Matter Integrity, and Associated Neuropsychological Dysfunction 25 Years After Pediatric Lymphoid Malignancies. JCO. 2013;31:3378–88.

43. Simó M, Vaquero L, Ripollés P, Jové J, Fuentes R, Cardenal F, et al. Brain damage following prophylactic cranial irradiation in lung cancer survivors. Brain Imaging and Behavior. 2016;10:283–95.

44. Chapman CH, Tong Z, Cao Y. Diffusion tensor imaging predicts cognitive function change following partial brain radiotherapy for low-grade and benign tumors. Radiotherapy and Oncology. 2016;7.

45. Butler RW, Fairclough DL, Katz ER, Kazak AE, Noll RB, Thompson RD, et al. Intellectual functioning and multi-dimensional attentional processes in long-term survivors of a central nervous system related pediatric malignancy. Life Sciences. 2013;93:611–6.

46. Anderson V, Godber T, Smibert E, Ekert H. Neurobehavioural sequelae following cranial irradiation and chemotherapy in children: an analysis of risk factors. Pediatric Rehabilitation. 1997;1:63–76.

47. Schatz J, Kramer JH, Ablin AR, Matthay KK. Processing Speed, Working Memory, and IQ: A Developmental Model of Cognitive Deficits Following Cranial Radiation Therapy. Neuropsychology. 2000;14:189–200.

48. Schuitema I, de Sonneville L, Kaspers G, van der Pal H, Uyttebroeck A, van den Bos C, et al. Executive Dysfunction 25 Years after Treatment with Cranial Radiotherapy for Pediatric Lymphoid Malignancies. J Int Neuropsychol Soc. 2015;21:657–69.

49. Douw L, Klein M, Fagel SS, van den Heuvel J, Taphoorn MJ, Aaronson NK, et al. Cognitive and radiological effects of radiotherapy in patients with low-grade glioma: long-term follow-up. The Lancet Neurology. 2009;8:810–8.

50. Rashid A, Ram AN, Kates WR, Redmond KJ, Wharam M, Mark Mahone E, et al. A prospective study of corpus callosum regional volumes and neurocognitive outcomes following cranial radiation for pediatric brain tumors. Childs Nerv Syst. 2017;33:965–72.

51. Roddy E, Sear K, Felton E, Tamrazi B, Gauvain K, Torkildson J, et al. Presence of cerebral microbleeds is associated with worse executive function in pediatric brain tumor survivors. Neuro Oncol. 2016;now163.

52. Krull KR, Brinkman TM, Li C, Armstrong GT, Ness KK, Srivastava DK, et al. Neurocognitive Outcomes Decades After Treatment for Childhood Acute Lymphoblastic Leukemia: A Report From the St Jude Lifetime Cohort Study. JOURNAL OF CLINICAL ONCOLOGY. 2013;12.

53. Schatz J, Kramer JH, Ablin AR, Matthay KK. Visual attention in long-term survivors of leukemia receiving cranial radiation therapy. 2004;10.

54. Mulhern RK, Kovnar E, Langston J, Carter M, Fairclough D, Leigh L, et al. Long-term survivors of leukemia treated in infancy: factors associated with neuropsychologic status. 1992;8.

55. Chang EL, Wefel JS, Hess KR, Allen PK, Lang FF, Kornguth DG, et al. Neurocognition in patients with brain metastases treated with radiosurgery or radiosurgery plus whole-brain irradiation: a randomised controlled trial. The Lancet Oncology. 2009;10:1037–44.

56. Chapman CH, Buchtel H, Lawrence TS. Diffusion Tensor Imaging of Normal-Appearing White Matter as Biomarker for Radiation-Induced Late Delayed Cognitive Decline. 2012;82:8.

57. Riggs L, Bouffet E, Laughlin S, Laperriere N, Liu F, Skocic J, et al. Changes to Memory Structures in Children Treated for Posterior Fossa Tumors. J Int Neuropsychol Soc. 2014;20:168–80.

58. Armstrong CL, Fisher MJ, Li Y, Lustig RA, Belasco JB, Minturn JE, et al. Neuroplastic Response After Radiation Therapy for Pediatric Brain Tumors: A Pilot Study. International Journal of Radiation Oncology*Biology*Physics. 2016;95:991–8.

59. Tringale KR, Nguyen TT, Karunamuni R, Seibert T, Huynh-Le M-P, Connor M, et al. Quantitative Imaging Biomarkers of Damage to Critical Memory Regions Are Associated With Post–Radiation Therapy Memory Performance in Brain Tumor Patients. International Journal of Radiation Oncology*Biology*Physics. 2019;105:773–83.

60. Brown PD, Gondi V, Pugh S, Tome WA, Wefel JS, Armstrong TS, et al. Hippocampal Avoidance During Whole-Brain Radiotherapy Plus Memantine for Patients With Brain Metastases: Phase III Trial NRG Oncology CC001. JCO. 2020;38:1019–29.

61. Morrison MA, Mueller S, Felton E, Jakary A, Stoller S, Avadiappan S, et al. Rate of radiation-induced microbleed formation on 7T MRI relates to cognitive impairment in young patients treated with radiation therapy for a brain tumor. Radiotherapy and Oncology. 2021;154:145–53.

62. Redmond KJ, Hildreth M, Sair HI, Terezakis S, McNutt T, Kleinberg L, et al. Association of Neuronal Injury in the Genu and Body of Corpus Callosum After Cranial Irradiation in Children With Impaired Cognitive Control: A Prospective Study. International Journal of Radiation Oncology*Biology*Physics. 2018;101:1234–42.

63. MacLean WE, Noll RB, Stehbens JA, Kaleita TA, Schwartz E, Whitt JK, et al. Neuropsychological Effects of Cranial Irradiation in Young Children With Acute Lymphoblastic Leukemia 9 Months After Diagnosis. Archives of Neurology. 1995;52:156–60.

64. Tibbs MD, Huynh-Le M-P, Karunamuni R, Reyes A, Macari AC, Tringale KR, et al. Microstructural Injury to Left-Sided Perisylvian White Matter Predicts Language Decline After Brain Radiation Therapy. International Journal of Radiation Oncology*Biology*Physics. 2020;108:1218–28.

65. Twaddle V, Britton PG, Craft AC, Noble TC, Kernahan J. Intellectual function after treatment for leukaemia or solid tumours. Archives of Disease in Childhood. 1983;58:949–52.

66. Radcliffe J, Bunin GR, Sutton LN, Goldwein JW, Phillips‖ PC. Cognitive deficits in long-term survivors of childhood medulloblastoma and other noncortical tumors: Age-dependent effects of whole brain radiation. International Journal of Developmental Neuroscience. 1994;12:327–34.

67. Davidson A, Tait DM, Payne GS, Hopewell JW, Leach MO, Watson M, et al. Magnetic resonance spectroscopy in the evaluation of neurotoxicity following cranial irradiation for childhood cancer. BJR. 2000;73:421–4.

68. Omuro AMP, Ben-Porat LS, Panageas KS, Kim AK, Correa DD, Yahalom J, et al. Delayed Neurotoxicity in Primary Central Nervous System Lymphoma. Arch Neurol [Internet]. 2005 [cited 2021 Jan 20];62. Available from: http://archneur.jamanetwork.com/article.aspx?doi=10.1001/archneur.62.10.1595

69. Khong P-L, Leung LHT, Fung ASM, Fong DYT, Qiu D, Kwong DLW, et al. White Matter Anisotropy in Post-Treatment Childhood Cancer Survivors: Preliminary Evidence of Association With Neurocognitive Function. JCO. 2006;24:884–90.

70. Aoyama H, Tago M, Kato N, Toyoda T, Kenjyo M, Hirota S, et al. Neurocognitive Function of Patients with Brain Metastasis Who Received Either Whole Brain Radiotherapy Plus Stereotactic Radiosurgery or Radiosurgery Alone. International Journal of Radiation Oncology*Biology*Physics. 2007;68:1388–95.

71. Tang Y, Luo D, Rong X, Shi X, Peng Y. Psychological Disorders, Cognitive Dysfunction and Quality of Life in Nasopharyngeal Carcinoma Patients with Radiation-Induced Brain Injury. Lim M, editor. PLoS ONE. 2012;7:e36529.

72. Merchant TE, Schreiber JE, Wu S, Lukose R, Xiong X, Gajjar A. Critical Combinations of Radiation Dose and Volume Predict Intelligence Quotient and Academic Achievement Scores After Craniospinal Irradiation in Children With Medulloblastoma. International Journal of Radiation Oncology*Biology*Physics. 2014;90:554–61.

73. King TZ, Wang L, Mao H. Disruption of White Matter Integrity in Adult Survivors of Childhood Brain Tumors: Correlates with Long-Term Intellectual Outcomes. Frasch MG, editor. PLoS ONE. 2015;10:e0131744.

74. Roth AK, Ris MD, Orobio J, Xue J, Mahajan A, Paulino AC, et al. Cognitive mediators of adaptive functioning outcomes in survivors of pediatric brain tumors treated with proton radiotherapy. Pediatr Blood Cancer [Internet]. 2020 [cited 2021 Jan 20];67. Available from: https://onlinelibrary.wiley.com/doi/abs/10.1002/pbc.28064

75. Alirezaei Z, Amouheidari A, Hassanpour M, Davanian F, Iraji S, Shokrani P, et al. Early Detection of Radiation-Induced Injury and Prediction of Cognitive Deficit by MRS Metabolites in Radiotherapy of Low-Grade Glioma. Bunevicius A, editor. BioMed Research International. 2021;2021:1–13.

76. Lin X, Tang L, Li M, Wang M, Guo Z, Lv X, et al. Irradiation-related longitudinal white matter atrophy underlies cognitive impairment in patients with nasopharyngeal carcinoma. Brain Imaging and Behavior. 2021;15:2426–35.

77. Phillips NS, Hillenbrand CM, Mitrea BG, Yan J, Li C, Scoggins MA, et al. Cerebral microbleeds in adult survivors of childhood acute lymphoblastic leukemia treated with cranial radiation. Sci Rep. 2020;10:692.

78. Agbahiwe H, Rashid A, Horska A, Mahone EM, Lin D, McNutt T, et al. A prospective study of cerebral, frontal lobe, and temporal lobe volumes and neuropsychological performance in children with primary brain tumors treated with cranial radiation: Brain Volumes and Neuropsychological Assessment. Cancer. 2017;123:161–8.

79. Bian Y, Meng L, Peng J, Li J, Wei R, Huo L, et al. Effect of radiochemotherapy on the cognitive function and diffusion tensor and perfusion weighted imaging for high-grade gliomas: A prospective study. Sci Rep. 2019;9:5967.

80. Waber DP, Silverman LB, Catania L, Mautz W, Rue M, Gelber RD, et al. Outcomes of a Randomized Trial of Hyperfractionated Cranial Radiation Therapy for Treatment of High-Risk Acute Lymphoblastic Leukemia: Therapeutic Efficacy and Neurotoxicity. JCO. 2004;22:2701–7.

81. Nagesh V, Ross BD, Cao Y. RADIATION-INDUCED CHANGES IN NORMAL-APPEARING WHITE MATTER IN PATIENTS WITH CEREBRAL TUMORS: A DIFFUSION TENSOR IMAGING STUDY. 2008;70:9.

82. Haris M, Kumar S, Raj MK, Das KJM, Sapru S, Behari S, et al. Serial diffusion tensor imaging to characterize radiation-induced changes in normal-appearing white matter following radiotherapy in patients with adult low-grade gliomas. Radiat Med. 2008;26:140–50.

83. Rueckriegel SM, Driever PH, Blankenburg F, Lüdemann L, Henze G, Bruhn H. Differences in Supratentorial Damage of White Matter in Pediatric Survivors of Posterior Fossa Tumors With and Without Adjuvant Treatment as Detected by Magnetic Resonance Diffusion Tensor Imaging. International Journal of Radiation Oncology*Biology*Physics. 2010;76:859–66.

84. Xiong WF, Qiu SJ, Wang HZ, Lv XF. 1H-MR spectroscopy and diffusion tensor imaging of normal-appearing temporal white matter in patients with nasopharyngeal carcinoma after irradiation: Initial experience. J Magn Reson Imaging. 2013;37:101–8.

85. Hope TR, Vardal J, Bjørnerud A, Larsson C, Arnesen MR, Salo RA, et al. Serial diffusion tensor imaging for early detection of radiation-induced injuries to normal-appearing white matter in high-grade glioma patients: Tracking early RBI with DTI. J Magn Reson Imaging. 2015;41:414–23.

86. Connor M, Karunamuni R, McDonald C, White N, Pettersson N, Moiseenko V, et al. Dose-dependent white matter damage after brain radiotherapy. Radiotherapy and Oncology. 2016;121:209–16.

87. Duan F, Cheng J, Jiang J, Chang J, Zhang Y, Qiu S. Whole-brain changes in white matter microstructure after radiotherapy for nasopharyngeal carcinoma: a diffusion tensor imaging study. Eur Arch Otorhinolaryngol. 2016;273:4453–9.

88. Connor M, Karunamuni R, McDonald C, Seibert T, White N, Moiseenko V, et al. Regional susceptibility to dose-dependent white matter damage after brain radiotherapy. Radiotherapy and Oncology. 2017;123:209–17.

89. Leng X, Fang P, Lin H, An J, Tan X, Zhang C, et al. Structural MRI research in patients with nasopharyngeal carcinoma following radiotherapy: A DTI and VBM study. Oncol Lett [Internet]. 2017 [cited 2022 Jan 16]; Available from: http://www.spandidos-publications.com/10.3892/ol.2017.6968

90. Makola M, Douglas Ris M, Mahone EM, Yeates KO, Cecil KM. Long-term effects of radiation therapy on white matter of the corpus callosum: a diffusion tensor imaging study in children. Pediatr Radiol. 2017;47:1809–16.

91. Follin C, Svärd D, van Westen D, Björkman-Burtscher IM, Sundgren PC, Fjalldal S, et al. Microstructural white matter alterations associated to neurocognitive deficits in childhood leukemia survivors treated with cranial radiotherapy – a diffusional kurtosis study. Acta Oncologica. 2019;58:1021–8.

92. Morrison MA, Hess CP, Clarke JL, Butowski N, Chang SM, Molinaro AM, et al. Risk factors of radiotherapy-induced cerebral microbleeds and serial analysis of their size compared with white matter changes: A 7T MRI study in 113 adult patients with brain tumors: Cerebral Microbleeds in Adult Brain Tumor. J Magn Reson Imaging. 2019;50:868–77.

93. Usenius T, Usenius J-P, Tenhunen M, Vainio P, Johansson R, Soimakallio S, et al. Radiation-induced changes in human brain metabolites as studied by 1H nuclear magnetic resonance spectroscopy in vivo. International Journal of Radiation Oncology*Biology*Physics. 1995;33:719–24.

94. Reddick WE, Mulhern RK, Elkin TD, Glass JO, Merchant TE, Langston JW. A hybrid neural network analysis of subtle brain volume differences in children surviving brain tumors. Magnetic Resonance Imaging. 1998;16:413–21.

95. Reddick WE, Glass JO, Palmer SL, Wu S, Gajjar A, Langston JW, et al. Atypical white matter volume development in children followingcraniospinal irradiation. Neuro-Oncology. 2005;7:12–9.

96. Faraci M, Morana G, Bagnasco F, Barra S, Polo P, Hanau G, et al. Magnetic resonance imaging in childhood leukemia survivors treated with cranial radiotherapy: A cross sectional, single center study. Pediatr Blood Cancer. 2011;57:240–6.

97. Lupo JM, Chuang CF, Chang SM, Barani IJ, Jimenez B, Hess CP, et al. 7-Tesla Susceptibility-Weighted Imaging to Assess the Effects of Radiotherapy on Normal-Appearing Brain in Patients With Glioma. International Journal of Radiation Oncology*Biology*Physics. 2011;82:e493–500.

98. Peters S, Pahl R, Claviez A, Jansen O. Detection of irreversible changes in susceptibility-weighted images after whole-brain irradiation of children. Neuroradiology. 2013;55:853–9.

99. Varon D, Simons M, Chiang F, Tedesqui G, Pacheco G, Martinez P, et al. Brain Radiation-Related Black Dots on Susceptibility-Weighted Imaging. Neuroradiol J. 2014;27:445–51.

100. Lupo JM, Molinaro AM, Essock-Burns E, Butowski N, Chang SM, Cha S, et al. The effects of anti-angiogenic therapy on the formation of radiation-induced microbleeds in normal brain tissue of patients with glioma. Neuro Oncol. 2016;18:87–95.

101. Kralik SF, Mereniuk TR, Grignon L, Shih C-S, Ho CY, Finke W, et al. Radiation-Induced Cerebral Microbleeds in Pediatric Patients With Brain Tumors Treated With Proton Radiation Therapy. International Journal of Radiation Oncology*Biology*Physics. 2018;102:1465–71.

102. Andersen PB, Krabbe K, Leffers AM, Schmiegelow M, Holm S, Laursen H, et al. Cerebral glucose metabolism in long-term survivors of childhood primary brain tumors treated with surgery and radiotherapy. 2003;9.

103. Belliveau J-G, Bauman GS, Tay KY, Ho D, Menon RS. Initial Investigation into Microbleeds and White Matter Signal Changes following Radiotherapy for Low-Grade and Benign Brain Tumors Using Ultra-High-Field MRI Techniques. AJNR Am J Neuroradiol. 2017;38:2251–6.

104. Johannesen TB, Henrik Lien H, Håkon Hole K, Lote K. Radiological and clinical assessment of long-term brain tumour survivors after radiotherapy. Radiotherapy and Oncology. 2003;69:169–76.

105. Matsumoto K, Takahashi S, Sato A, Imaizumi M. Leukoencephalopathy in childhood hematopoietic neoplasm caused by moderate-dose methotrexate and prophylactic cranial radiotherapy--an MR analysis. International Journal of Radiation Oncology*Biology*Physics. 1995;32.

106. Virta A, Patronas N, Raman R, Dwyer A, Barnett A, Bonavita S, et al. Spectroscopic imaging of radiation-induced effects in the white matter of glioma patients. Magnetic Resonance Imaging. 2000;18:851–7.

107. Rutkowski T, Tarnawski R, Sokol M, Maciejewski B. 1h-mr spectroscopy of normal brain tissue before and after postoperative radiotherapy because of primary brain tumors. International Journal of Radiation Oncology*Biology*Physics. 2003;56:1381–9.

108. Sundgren PC, Nagesh V, Elias A, Tsien C, Junck L, Gomez Hassan DM, et al. Metabolic alterations: A biomarker for radiation-induced normal brain injury-an MR spectroscopy study. Journal of Magnetic Resonance Imaging. 2009;29:291–7.

109. Rueckriegel SM, Driever PH, Bruhn H. Supratentorial Neurometabolic Alterations in Pediatric Survivors of Posterior Fossa Tumors. International Journal of Radiation Oncology*Biology*Physics. 2012;82:1135–41.

110. Wang H-Z, Qiu S-J, Lv X-F, Wang Y-Y, Liang Y, Xiong W-F, et al. Diffusion tensor imaging and 1H-MRS study on radiation-induced brain injury after nasopharyngeal carcinoma radiotherapy. Clinical Radiology. 2012;67:340–5.

111. Seibert TM, Karunamuni R, Kaifi S, Burkeen J, Connor M, Krishnan AP, et al. Cerebral Cortex Regions Selectively Vulnerable to Radiation Dose-Dependent Atrophy. International Journal of Radiation Oncology*Biology*Physics. 2017;97:910–8.

112. Karunamuni R, Bartsch H, White NS, Moiseenko V, Carmona R, Marshall DC, et al. Dose-Dependent Cortical Thinning After Partial Brain Irradiation in High-Grade Glioma. International Journal of Radiation Oncology*Biology*Physics. 2016;94:297–304.

113. Shi L, Du F-L, Sun Z-W, Zhang L, Chen Y-Y, Xie T-M, et al. Radiation-induced gray matter atrophy in patients with nasopharyngeal carcinoma after intensity modulated radiotherapy: a MRI magnetic resonance imaging voxel-based morphometry study. Quant Imaging Med Surg. 2018;8:902–9.

114. Nagtegaal SHJ, David S, Philippens MEP, Snijders TJ, Leemans A, Verhoeff JJC. Dose-dependent volume loss in subcortical deep grey matter structures after cranial radiotherapy. Clinical and Translational Radiation Oncology. 2021;26:35–41.

115. Prust MJ, Jafari-Khouzani K, Kalpathy-Cramer J, Polaskova P, Batchelor TT, Gerstner ER, et al. Standard chemoradiation for glioblastoma results in progressive brain volume loss. Neurology. 2015;85:683–91.

116. Passos J, Nzwalo H, Marques J, Azevedo A, Netto E, Nunes S, et al. Late Cerebrovascular Complications After Radiotherapy for Childhood Primary Central Nervous System Tumors. Pediatric Neurology. 2015;53:211–5.

117. Yoneoka Y, Satoh M, Akiyama K, Sano K, Fujii Y, Tanaka R. An experimental study of radiation-induced cognitive dysfunction in an adult rat model. BJR. 1999;72:1196–201.

118. Raber J, Rola R, LeFevour A, Morhardt D, Curley J, Mizumatsu S, et al. Radiation-Induced Cognitive Impairments are Associated with Changes in Indicators of Hippocampal Neurogenesis. Radiation Research. 2004;162:39–47.

119. Rola R, Raber J, Rizk A, Otsuka S, VandenBerg SR, Morhardt DR, et al. Radiation-induced impairment of hippocampal neurogenesis is associated with cognitive deficits in young mice. Experimental Neurology. 2004;188:316–30.

120. Shi L, Adams MM, Long A, Carter CC, Bennett C, Sonntag WE, et al. Spatial Learning and Memory Deficits after Whole-Brain Irradiation are Associated with Changes in NMDA Receptor Subunits in the Hippocampus. Radiation Research. 2006;166:892–9.

121. Zhao W, Payne V, Tommasi E, Diz DI, Hsu F-C, Robbins ME. Administration of the peroxisomal proliferator-activated receptor γ agonist pioglitazone during fractionated brain irradiation prevents radiation-induced cognitive impairment. International Journal of Radiation Oncology*Biology*Physics. 2007;67:6–9.

122. Brown WR, Blair RM, Moody DM, Thore CR, Ahmed S, Robbins ME, et al. Capillary loss precedes the cognitive impairment induced by fractionated whole-brain irradiation: A potential rat model of vascular dementia. Journal of the Neurological Sciences. 2007;257:67–71.

123. Atwood T, Payne VS, Zhao W, Brown WR, Wheeler KT, Zhu J-M, et al. Quantitative Magnetic Resonance Spectroscopy Reveals a Potential Relationship between Radiation-Induced Changes in Rat Brain Metabolites and Cognitive Impairment. Radiation Research. 2007;168:574–81.

124. Robbins ME, Payne V, Tommasi E, Diz DI, Hsu F-C, Brown WR, et al. The AT1 Receptor Antagonist, L-158,809, Prevents or Ameliorates Fractionated Whole-Brain Irradiation–Induced Cognitive Impairment. International Journal of Radiation Oncology*Biology*Physics. 2009;73:499–505.

125. Acharya MM, Christie L-A, Lan ML, Donovan PJ, Cotman CW, Fike JR, et al. Rescue of radiation-induced cognitive impairment through cranial transplantation of human embryonic stem cells. PNAS. 2009;106:19150–5.

126. Caceres LG, Aon Bertolino L, Saraceno GE, Zorrilla Zubilete MA, Uran SL, Capani F, et al. Hippocampal-related memory deficits and histological damage induced by neonatal ionizing radiation exposure. Role of oxidative status. Brain Research. 2010;1312:67–78.

127. Acharya MM, Christie L-A, Lan ML, Giedzinski E, Fike JR, Rosi S, et al. Human Neural Stem Cell Transplantation Ameliorates Radiation-Induced Cognitive Dysfunction. Cancer Research. 2011;71:4834–45.

128. Nageswara Rao AA, Ye H, Decker PA, Howe CL, Wetmore C. Therapeutic doses of cranial irradiation induce hippocampus-dependent cognitive deficits in young mice. J Neurooncol. 2011;105:191–8.

129. Warrington JP, Csiszar A, Mitschelen M, Lee YW, Sonntag WE. Whole Brain Radiation-Induced Impairments in Learning and Memory Are Time-Sensitive and Reversible by Systemic Hypoxia. Arai K, editor. PLoS ONE. 2012;7:e30444.

130. Acharya MM, Christie L-A, Lan ML, Limoli CL. Comparing the Functional Consequences of Human Stem Cell Transplantation in the Irradiated Rat Brain. Cell Transplant. 2013;22:55–64.

131. Belarbi K, Jopson T, Arellano C, Fike JR, Rosi S. CCR2 Deficiency Prevents Neuronal Dysfunction and Cognitive Impairments Induced by Cranial Irradiation. Cancer Research. 2013;73:1201–10.

132. Jenrow KA, Brown SL, Lapanowski K, Naei H, Kolozsvary A, Kim JH. Selective Inhibition of Microglia-Mediated Neuroinflammation Mitigates Radiation-Induced Cognitive Impairment. Radiation Research. 2013;179:549–56.

133. Parihar VK, Acharya MM, Roa DE, Bosch O, Christie L-A, Limoli CL. Defining functional changes in the brain caused by targeted stereotaxic radiosurgery. 2014;23.

134. Greene-Schloesser D, Payne V, Peiffer AM, Hsu F-C, Riddle DR, Zhao W, et al. The Peroxisomal Proliferator-Activated Receptor (PPAR) α Agonist, Fenofibrate, Prevents Fractionated Whole-Brain Irradiation-Induced Cognitive Impairment. Radiation Research. 2014;181:33.

135. Forbes ME, Paitsel M, Bourland JD, Riddle DR. Early-Delayed, Radiation-Induced Cognitive Deficits in Adult Rats are Heterogeneous and Age-Dependent. Radiation Research. 2014;182:60.

136. Peiffer AM, Creer RM, Linville C, Olson J, Kulkarni P, Brown JA, et al. Radiation-induced cognitive impairment and altered diffusion tensor imaging in a juvenile rat model of cranial radiotherapy. International Journal of Radiation Biology. 2014;90:799–806.

137. Acharya MM, Christie L-A, Hazel TG, Johe KK, Limoli CL. Transplantation of Human Fetal-Derived Neural Stem Cells Improves Cognitive Function following Cranial Irradiation. Cell Transplant. 2014;23:1255–66.

138. Baulch JE, Acharya MM, Allen BD, Ru N, Chmielewski NN, Martirosian V, et al. Cranial grafting of stem cell-derived microvesicles improves cognition and reduces neuropathology in the irradiated brain. Proc Natl Acad Sci USA. 2016;113:4836–41.

139. Acharya MM, Baulch JE, Lusardi TA, Allen BarrettD, Chmielewski NN, Baddour AAD, et al. Adenosine Kinase Inhibition Protects against Cranial Radiation-Induced Cognitive Dysfunction. Front Mol Neurosci [Internet]. 2016 [cited 2020 Jul 1];9. Available from: http://journal.frontiersin.org/Article/10.3389/fnmol.2016.00042/abstract

140. Sun R, Zhang L-Y, Chen L-S, Tian Y. Long-term outcome of changes in cognitive function of young rats after various/different doses of whole brain irradiation. Neurological Research. 2016;38:647–54.

141. Acharya MM, Green KN, Allen BD, Najafi AR, Syage A, Minasyan H, et al. Elimination of microglia improves cognitive function following cranial irradiation. Sci Rep. 2016;6:31545.

142. Brown RJ, Jun BJ, Cushman JD, Nguyen C, Beighley AH, Blanchard J, et al. Changes in Imaging and Cognition in Juvenile Rats After Whole-Brain Irradiation. International Journal of Radiation Oncology*Biology*Physics. 2016;96:470–8.

143. Feng X, Jopson TD, Paladini MS, Liu S, West BL, Gupta N, et al. Colony-stimulating factor 1 receptor blockade prevents fractionated whole-brain irradiation-induced memory deficits. J Neuroinflammation. 2016;13:215.

144. Bazyar S, Inscoe CR, Benefield T, Zhang L, Lu J, Zhou O, et al. Neurocognitive sparing of desktop microbeam irradiation. Radiat Oncol. 2017;12:127.

145. Allen BD, Acharya MM, Lu C, Giedzinski E, Chmielewski NN, Quach D, et al. Remediation of Radiation-Induced Cognitive Dysfunction through Oral Administration of the Neuroprotective Compound NSI-189. Radiation Research. 2018;189:345.

146. Bálentová S, Hajtmanová E, Filová B, Borbélyová V, Lehotský J, Adamkov M. Effects of fractionated whole-brain irradiation on cellular composition and cognitive function in the rat brain. International Journal of Radiation Biology. 2018;94:238–47.

147. Alexander TC, Butcher H, Krager K, Kiffer F, Groves T, Wang J, et al. Behavioral Effects of Focal Irradiation in a Juvenile Murine Model. Radiation Research. 2018;189:605–17.

148. Perez EC, Rodgers SP, Inoue T, Pedersen SE, Leasure JL, Gaber MW. Olfactory Memory Impairment Differs by Sex in a Rodent Model of Pediatric Radiotherapy. Front Behav Neurosci. 2018;12:158.

149. He Y, Peng Y, Chang Y, Zhu J, Li Z, Huang K, et al. Utilizing the Faxitron MultiRad 225 X-ray irradiation system for the construction of mouse chronic whole brain radiation model. Journal of Radiation Research. 2021;rrab086.

150. Sahnoune I, Inoue T, Kesler SR, Rodgers SP, Sabek OM, Pedersen SE, et al. Exercise ameliorates neurocognitive impairments in a translational model of pediatric radiotherapy. Neuro-Oncology. 2018;20:695–704.

151. Tang TT, Zawaski JA, Kesler SR, Beamish CA, Reddick WE, Glass JO, et al. A comprehensive preclinical assessment of late-term imaging markers of radiation-induced brain injury. Neuro-Oncology Advances. 2019;1:vdz012.

152. Rodgers SP, Zawaski JA, Sahnoune I, Leasure JL, Gaber MW. Radiation-Induced Growth Retardation and Microstructural and Metabolite Abnormalities in the Hippocampus. Neural Plasticity. 2016;2016:1–12.

153. Chen H, Cheng Y-S, Zhou Z-R. Long-term Brain Tissue Monitoring after Semi-brain Irradiation in Rats Using Proton Magnetic Resonance Spectroscopy: A Preliminary Study In vivo. Chinese Medical Journal. 2017;130:957–63.

154. Bálentová S, Hnilicová P, Kalenská D, Murín P, Hajtmanová E, Lehotský J, et al. Effect of whole-brain irradiation on the specific brain regions in a rat model: Metabolic and histopathological changes. NeuroToxicology. 2017;60:70–81.

155. Pérès EA, Etienne O, Grigis A, Boumezbeur F, Boussin FD, Le Bihan D. Longitudinal Study of Irradiation-Induced Brain Microstructural Alterations With S-Index, a Diffusion MRI Biomarker, and MR Spectroscopy. International Journal of Radiation Oncology*Biology*Physics. 2018;102:1244–54.

156. Hnilicová P, Bálentová S, Kalenská D, Muríň P, Hajtmanová E, Dobrota D, et al. In vivo MR study of neuro-glial hippocampal changes in a rat model of fractionated craniospinal irradiation. 2019;61:7.

157. Bálentová S, Hnilicová P, Kalenská D, Baranovičová E, Muríň P, Bittšanský M, et al. Metabolic and histopathological changes in the brain and plasma of rats exposed to fractionated whole-brain irradiation. Brain Research. 2019;1708:146–59.

158. Bálentová S, Hnilicová P, Kalenská D, Baranovičová E, Muríň P, Hajtmanová E, et al. Effect of fractionated whole-brain irradiation on brain and plasma in a rat model: Metabolic, volumetric and histopathological changes. Neurochemistry International. 2021;145:104985.

159. Beera KG, Li Y-Q, Dazai J, Stewart J, Egan S, Ahmed M, et al. Altered brain morphology after focal radiation reveals impact of off-target effects: implications for white matter development and neurogenesis. Neuro-Oncology. 2018;20:788–98.

160. de Guzman AE, Ahmed M, Li Y-Q, Wong CS, Nieman BJ. p53 Loss Mitigates Early Volume Deficits in the Brains of Irradiated Young Mice. International Journal of Radiation Oncology*Biology*Physics. 2019;103:511–20.

161. Wang S, Wu EX, Qiu D, Leung LHT, Lau H-F, Khong P-L. Longitudinal Diffusion Tensor Magnetic Resonance Imaging Study of Radiation-Induced White Matter Damage in a Rat Model. Cancer Res. 2009;69:1190–8.

162. Wang S, Qiu D, So K-F, Wu EX, Leung LHT, Gu J, et al. Radiation induced brain injury: assessment of white matter tracts in a pre-clinical animal model using diffusion tensor MR imaging. J Neurooncol. 2013;112:9–15.

163. Liu X-J, Fu W-W, Yang G-W, Liu S-E, Li Y, Duan C-F, et al. Correlation between diffusion tensor imaging and pathology in rats with brain radiation injury. 2015;6.

164. Britten RA, Wellman LL, Sanford LD. Progressive increase in the complexity and translatability of rodent testing to assess space-radiation induced cognitive impairment. Neuroscience & Biobehavioral Reviews. 2021;126:159–74.

165. Hanbury DB, Robbins ME, Bourland JD, Wheeler KT, Peiffer AM, Mitchell EL, et al. Pathology of Fractionated Whole-Brain Irradiation in Rhesus Monkeys (Macaca mulatta). Radiation Research. 2015;183:367–74.

166. Andrews RN, Dugan GO, Peiffer AM, Hawkins GA, Hanbury DB, Bourland JD, et al. White Matter is the Predilection Site of Late-Delayed Radiation-Induced Brain Injury in Non-Human Primates. Radiation Research [Internet]. 2019 [cited 2019 Feb 27]; Available from: http://www.rrjournal.org/doi/10.1667/RR15263.1

167. Robbins ME, Bourland JD, Cline JM, Wheeler KT, Deadwyler SA. A Model for Assessing Cognitive Impairment after Fractionated Whole-Brain Irradiation in Nonhuman Primates. Radiation Research. 2011;175:519–25.

168. Athanasiadi I, Perez WD, Plantenga JM, Jones-Hall Y, Perez-Torres CJ. Feasibility of a mini-pig model of radiation-induced brain injury to one cerebral hemisphere. Radiat Oncol. 2021;16:30.

169. Benczik J, Tenhunen M, Snellman M, Joensuu H, Färkkilä M, Joensuu R, et al. Late radiation effects in the dog brain: correlation of MRI and histological changes. Radiotherapy and Oncology. 2002;63:107–20.

170. Durand T, Bernier M-O, Léger I, Taillia H, Noël G, Psimaras D, et al. Cognitive outcome after radiotherapy in brain tumor: Current Opinion in Oncology. 2015;27:510–5.

171. van den Heuvel MP, Hulshoff Pol HE. Exploring the brain network: A review on resting-state fMRI functional connectivity. European Neuropsychopharmacology. 2010;20:519–34.

172. Zhao L-M, Kang Y-F, Gao J-M, Li L, Chen R-T, Zeng J-J, Zhang Y-M, Liao W. 2021. Functional Connectivity Density for Radiation Encephalopathy Prediction in Nasopharyngeal Carcinoma. Frontiers in Oncology [Internet]. [accessed 2022 Mar 14] 11. https://www.frontiersin.org/article/10.3389/fonc.2021.687127

173. Shi L, Linville MC, Iversen E, Molina DP, Yester J, Wheeler KT, Robbins ME, Brunso-Bechtold JK. 2009. Maintenance of white matter integrity in a rat model of radiation-induced cognitive impairment. Journal of the Neurological Sciences. 285(1–2):178–184. https://doi.org/10.1016/j.jns.2009.06.031

174. Rancilio NJ, Dahl S, Athanasiadi I, Perez-Torres CJ. 2017. Design, construction, and in vivo feasibility of a positioning device for irradiation of mice brains using a clinical linear accelerator and intensity modulated radiation therapy. International Journal of Radiation Biology. 93(12):1321–1326. https://doi.org/10.1080/09553002.2017.1387305

CHAPTER 3. FEASIBILITY OF A MINI-PIG MODEL OF RADIATION-INDUCED BRAIN INJURY TO ONE CEREBRAL HEMISPHERE

A version of this chapter has been previously published in *Radiation Oncology*: Athanasiadi, I., Perez, W.D., Plantenga, J.M. et al. Feasibility of a mini-pig model of radiation-induced brain injury to one cerebral hemisphere. *Radiat Oncol* 16, 30 (2021). https://doi.org/10.1186/s13014-021-01753-1

3.1 Introduction

Radiation therapy is an integral component in the treatment of intracranial tumors [1,2]. The use of advanced technologies has allowed for the delivery of higher doses of radiation to areas of the brain that are not accessible to surgery while sparing more normal tissues. Although radiation therapy has helped to improve brain cancer prognosis [1,2], the side effects caused by radiation are recognized to be significantly associated with decreased quality of life in brain cancer survivors, especially survivors of childhood brain cancer [3]. Late-onset radiation effects, which occur months to years after therapy and do not self-resolve, are the primary concern in terms of radiation-induced brain toxicity. Late-onset radiation-induced brain injury can be categorized into two broad types based on their radiological characteristics: focal and diffuse lesions [4]. Radiation necrosis is usually a focal injury that presents as a mass lesion with focal neurologic abnormalities and evidence of elevated intracranial pressure, whereas cognitive impairment is characterized by diffuse white matter injury [4,5]. Radiation necrosis and diffuse white matter injury have specific and distinct histological and MRI characteristics [6].

Prior work completed by our lab on the mouse model of radiation-induced diffuse white matter injury showed weaknesses in reproducing the exact brain injury seen in humans [7]. Although histology of the mouse brains revealed a dose-dependent change in the white matter tracts, the changes observed were subtle. Furthermore, we were unable to detect any abnormalities in T1-weighted and T2-weighted MRI images for any dose at any time point after irradiation [7]. These shortcomings, as well as the structural differences between mouse (lissencephalic) and human (gyrencephalic) brains, encouraged our investigation of other animal models with brain tissue characteristics closer to those of humans. Additionally, larger animal species are advantageous when investigating intracranial MRI diagnostic approaches since these are now

tested on clinical devices with the same protocols that can directly be used on human patients. The anatomy and size of porcine brains are well suited to address these challenges. Pigs can therefore be used to more accurately model the development of radiation-induced brain injury (RIBI).

Though there are prior reports of a pig model of RIBI [8,9], these prior works have limited clinical relevance due to how radiation was delivered (electrons instead of photons) and how the model was assessed (non-standard MRI approach). Therefore, the objective of the current study is to establish the feasibility of a RIBI pig model with equipment and approaches that reflect the current clinical scenario. Here, we describe the methods to generate a single-hemisphere RIBI model that is assessed in vivo with a standard clinical MRI approach. The advantage of this model is that all procedures are performed with clinical devices and following the same quality assurance that is performed on patients. Unlike rodent models, this pig model shows changes in anatomical MRI consistent with human RIBI. The approach described can be further adapted to either a whole-brain irradiation model with or without fractionation, or specific focal models targeting or avoiding substructures of interest, e.g., the hippocampus.

3.2 Methods

3.2.1 Animals and weekly observation

All animal procedures were approved by the Purdue Animal Care and Use Committee under protocol number 1712001655. Four male 3-month old Yucatan mini-pigs were obtained from Premier BioSource (formerly S&S Farms). All pigs were housed in pairs in a facility designated for large animal research. Water was provided ad libitum and a commercial feed ration was made available twice daily. Pigs were observed at least weekly for any overt neurological impairment. Within the first week after irradiation they were observed every 24 h to ensure no acute side effects. Weights were tacked weekly by animal care staff and showed normal weight gain. Pigs were assessed in two sets of two with the first receiving 25 Gy and the second set receiving 15 Gy. There was no explicit control group, instead the contralateral hemsphere was intended to serve as an internal control for each animal. Animal procedures were performed with the help of the Purdue Pre-Clinical Research Laboratory, a core facility of the Purdue Center for Comparative Translational Research with ample experience with pig models.

3.2.2 Anesthesia protocol

All pigs were anesthetized using a combination of tiletamine-zolazepam (3 mg/kg), detomidine (0.18 mg/kg), and butorphanol (0.12 mg/kg) administered intramuscularly. After attaining lateral recumbency, pigs were intubated with an appropriately sized endotracheal tube as determined using body weight. General anesthesia was maintained with isoflurane (1–2% inhaled) and oxygen as delivered using mechanical ventilation. Vital signs were monitored and logged throughout all procedures. All pigs received intravenous fluids (PlasmaLyte®; 5–10 mL/kg) via an intravenous catheter in the auricular vein. Butorphanol (0.2 mg/kg IV) was dosed as needed. Pigs were monitored after each procedure to ensure proper recovery from anesthesia until they were capable of standing and walking on their own.

3.2.3 Immobilization devices and CT simulation

Each anesthetized pig was positioned in sternal recumbency and immobilized using an individualized bite plate [10] and thermoplastic mask on an indexable frame (Uniframe Baseplate, Civco Medical Solutions, Orange City, IA) for radiation therapy simulation CT. The CT simulation treatment couch was positioned in the gantry and the reference isocenter was determined using CT lasers. Crosshair marks were applied to the mask using cloth tape and permanent marker over the intersection of the CT laser at three points. Radiopaque fiducial markers were affixed to the mask at the 3 laser intersection points (Suremark, Vision Line Premium Labels, V-25, Van Arsdale, Innovative Products, Pensacola, FL). Scans were acquired without contrast using a 64-slice CT scanner and 0.625 mm slice thickness (VCT 64-Slice, GE Healthcare, Milwaukee, WI).

3.2.4 MRI procedure

Subsequent to the CT scan, the pigs were imaged using a 3 T MRI unit (MAGNETOM® Prisma, Siemens Medical Solutions, Malvern, PA) using a 64-channel head coil with the pigs in sternal recumbency under general anesthesia. MR images of the brain were acquired 1 week pre-irradiation, 3 months post-irradiation, and either 4 months (P2) or 6 months (P3 and P4) post-irradiation with a consistent protocol. Included in the protocol were T1-weighted and T2-weighted images acquired using a three-dimensional Magnetization Prepared Rapid Acquisition Gradient Recalled Echo (3D MP-RAGE; TE = 4.7 ms, TR = 2080 ms, averages = 1) sequence and three-

dimensional Fast Spin Echo (3D FSE; TE = 410 ms, TR = 2800 ms, averages = 1) sequence, respectively. All scans were acquired with 0.7 mm isotropic resolution with the same geometry. The animals were then given an intravenous injection of 0.2 mL/kg of MultiHance. A period of 11 min was allotted to allow the contrast enough time to accumulate within the intracranial space before acquiring the post-contrast T1-weighted images.

3.2.5 Radiation treatment planning

CT and MRI images were imported and co-registered using the Varian Eclipse treatment planning system (Varian Eclipse v. 11.0, Varian Medical Systems, Palo Alto, CA). Transverse MRI images and CT images were used for manual brain tissue contouring. The contoured structures included brain, right and left cerebral hemispheres, cerebellum, left and right cerebellum, brainstem, cervical spinal cord, optic nerves (right and left), optic chiasm, eyes, and lenses. Diencephalon was contoured as part of the hemispheres. The planning target volume (PTV) for the first pair of pigs (P1 and P2) included the left cerebral hemisphere and left cerebellum. The PTV for the second pair of pigs (P3 and P4) included the left cerebral hemisphere only. In addition, the structures “brain minus PTV” (brain-PTV) and “brain minus PTV minus 2 mm” were created for plan evaluation and optimization, respectively.

Inverse planning for intensity modulated radiation therapy (IMRT) was used in all pigs. All treatment plans were corrected for tissue heterogeneity using a calculation algorithm (Anisotropic Analytical Algorithm, version 11.0.31, Varian Medical Systems, Palo Alto, CA). For steep dose gradient, the normal tissue objectives were applied using a distance from the target border of 0.1 cm, start dose 100%, end dose 60%, and fall off 0.9 cm. Coplanar, isocentric, non-parallel opposed beams were used with a sliding window technique. Nine angles of radiation beams were distributed entering the left hemisphere (350°, 346°, 330°, 307°, 282°, 270°, 230°, 198°, and 180°). A single dose of 25 Gy for the first pair of pigs (P1 and P2) and 15 Gy for the second pair (P3 and P4) was prescribed to the PTV, while the right side was spared as a control. The single dose of 25 Gy was selected based upon the previous pig model reports [8, 9]. The dose of 15 Gy was chosen based on matching the biological effective dose of one of the most common fractionated whole brain radiotherapy prescriptions (2 Gy × 30 fractions) under the assumption that the alpha–beta ratio of the brain is 3. The plans were evaluated for pre-treatment quality assurance using the MapCheck 2 diode array (Sun Nuclear Corporation, Melbourne, FL). Gamma

analysis and distance to agreement analysis were used to compare the planned and output absolute dose with point passing criteria of 3 mm and 3%. The plan was considered acceptable for therapy when at least 95% of all points matched. The evaluation of the plan quality included dose volume histograms (DVHs) and dose color wash for PTV coverage and doses to organs at risk (OARs). The doses to OARs were evaluated according to QUANTEC [11]. RadCalc software (LifeLine Software Inc.) was used as an independent method for verification of the monitor units (MUs). The plans were approved by a veterinary Radiation Oncologist.

The treatment parameters are reported as recommended by the ICRU [12,13,14]. Briefly, reported treatment parameters for the PTV included maximum ($D_{2\%}$), minimum ($D_{98\%}$), mean (D_{mean}), and median ($D_{50\%}$) dose. Homogeneity Index ($HI = (D_{2\%} – D_{98\%})/D_{50\%}$), Conformity Index (CI, described below) and Gradient Index (GI = brain volume receiving 50% of prescription dose divided by brain volume receiving 100% of prescription) were used to assess plans retrospectively and were not used in the process of plan approval. An HI close to 0 (zero) shows a homogeneous absorbed dose in the PTV. The CI defines how adequately a target is covered by treatment without irradiation of any tissue outside the PTV. Specifically we calculated the Paddick CI [15] defined as $CI = PTV_{PIV}^2 / (PTV \times PIV)$, where PTV_{PIV} is the volume of the PTV that is covered by 100% of the prescription dose and PIV is the brain volume receiving 100% of the prescription dose. A perfect plan has a CI score of 1. The GI is an objective tool to assess how rapidly the dose falls off outside of the PTV. A lower GI indicates steeper dose gradient and a value of < 3 could be ideal. Reported treatment parameters for the OARs (brainstem, cerebellum, spinal cord, optic nerves (right and left), and optic chiasm) included maximum ($D_{2\%}$), mean (D_{mean}), median ($D_{50\%}$), and Volume of Accepted Tolerance Dose (V_{ATD} = dose/volume limit). The maximum point dose (D_{max}) was recorded for the lenses. Treatment parameters for the cerebellum were reported only for P3 and P4, since the left side of the cerebellum was included in the PTV for P1 and P2.

3.2.6 Radiation delivery

Each pig was positioned with the same individualized device used in the CT simulation and aligned to the marked reference isocenter in the radiation therapy vault using room lasers and mask crosshair marks prior to irradiation. Cardinal direction shifts generated in the treatment planning software were applied to align the pig to the plan isocenter. Orthogonal portal MV radiographs were taken to verify the position. A computed portal radiography system was used to

develop each portal image (KODAK ACR—2000i, Onconcepts, Rochester, NY). DICOM portal images were imported into the treatment planning system, scaled, and aligned to the digital graticule in the treatment plan's digitally reconstructed radiographs. The registered images were compared using the offline review program (Varian Medical Systems, Palo Alto, CA). Images were compared for perfect visual alignment of bony structures to the digitally reconstructed radiographs created from CT images used for the IMRT planning. Position was adjusted if alignment differed by greater than 1 mm, and portal radiographs were repeated to document final positioning.

Radiation was delivered with a 6 MV linear accelerator (Varian 6EX, Varian Medical Systems, Inc. Palo Alto, CA) with a 120-leaf multileaf collimator (Millennium 120 MLC, Varian Medical Systems, Palo Alto, CA) using photons with a dose rate of 400 MU/min.

3.2.7 Necropsy

After the final MRI, pigs were euthanized by intravenous injection with pentobarbital (100–200 mg/kg). Due to neurological deficits, P1 was euthanized at 4 months and P2 at 3 months post irradiation. P3 and P4 were euthanized at 6 months as we had originally planned for all pigs. Brains were extracted by veterinary staff of the Indiana Animal Disease Diagnostic Laboratory and left in 10% neutral buffered formalin for at least 24 h. Coronal gross sections were generated to match areas of interest on the MRI datasets, embedded in paraffin, and stained with hematoxylin and eosin (H&E) and Luxol Fast Blue (LFB). The former was utilized for general pathological examination of the sections while the latter was used to evaluate white matter integrity of the irradiated hemisphere.

3.3 Results

3.3.1 Quality of half-brain treatment plan

The radiation treatment plan for each pig passed the quality assurance as described in the methods. Briefly, for the PTV dose coverage, 93% of the prescribed dose covered at least 93% of the PTV. The dose color wash and DVHs were similar in all 4 pigs. Figure 9 shows an example of dose color wash in 3 planes from P1 and P3. The prescribed dose is homogeneously distributed over the PTV and there is a steep fall-off of the dose at the PTV margins. The dosimetric

parameters for the PTV for all pigs are summarized in Table 5. The minimum, maximum, mean, and median doses to the PTV are reported as analyzed by the DVHs. The HI, CI, and GI for all four plans ranged 0.15–0.21, 0.57–0.74, and 1.9–2.7, respectively. The dosimetric parameters for the OARs for all pigs are summarized in Table 6. Briefly, doses to the spinal cord and lenses are much lower than the cut off recommended by QUANTEC for myelopathy or cataract, respectively [11]. Regarding the brainstem the high maximum ($D_{2\%}$) doses especially for P1 and P2 were seen as expected at the side adjacent to the PTV. However, the mean doses to the brainstem were low (3–11.3 Gy) in all for pigs. The optic apparatus (right and left optic nerve, optic chiasm) received doses relatively close to the prescribed doses as expected. The left optic nerve and the optic chiasm were included in the PTV and the right optic nerve was adjacent to the PTV. The dosimetric parameters for the cerebellum were reported for P3 and P4. The high maximum ($D_{2\%}$) doses were seen as expected adjacent to the PTV and the mean doses (3.4 Gy) were low. Looking more globally at the untreated parts of the brain in the brain-PTV volume, again we see the highest doses adjacent to the PTV but the mean doses are low (30 to 45% of the prescribed dose).

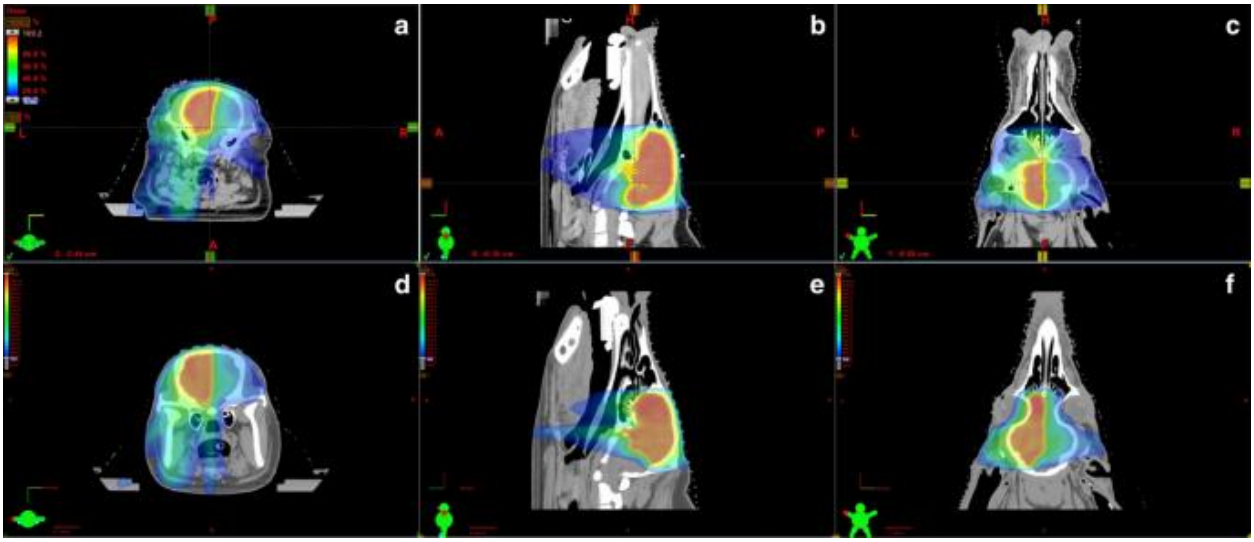

Figure 9. Treatment plan from subjects P1 and P3. Panels a–c for P1 and Panels d–f for P3 show a colorwash of the dose being delivered on the transverse (a and d), sagittal (b and e), and coronal (c and f) planes respectively. Blue areas receive ~ 10–20%, green areas ~ 50–60% and red areas ~ 100% of the target dose. The difference in coverage for the cerebellum on these plans can be best appreciated in the sagittal views.

Table 1. Summary of dosimetric results for PTV analyzed from dose-volume histogram. $D_{X\%}$ = dose (Gy) received by the x% of the volume; D_{mean} = mean dose received by the volume; HI = homogeneity index; CI = conformity index; GI = gradient index

Pigs	Volume (cm^3)	Min ($D_{98\%}$)	Max ($D_{2\%}$)	Mean (D_{mean})	Median ($D_{50\%}$)	HI	CI	GI
P1	35.4	22.8	26.8	25.3	25.5	0.16	0.74	1.9
P2	32.3	23	26.9	25.3	25.4	0.15	0.65	2.2
P3	31.0	13.4	16.4	15.1	15.1	0.20	0.57	2.6
P4	26.6	13.0	16.1	15.0	15.1	0.21	0.59	2.7

Table 2. Summary of dosimetric results for OARs analyzed from dose-volume histogram.

		P1	P2	P3	P4
Brainstem (V_{mean}=3.9 cm^3)	$D_{2\%}$ (Gy)	22.4	17.7	10.1	10.4
	D_{mean} (Gy)	11.3	9.6	3.6	3.0
	$V_{10/12}$ (%)	53/34	37/20	<3.4	<3.3
Cerebellum (V_{mean}=4.3 cm^3)	$D_{2\%}$ (Gy)			11.1	10.5
	D_{mean} (Gy)			3.4	3.4
	$V_{10/12}$ (%)			4.6	4.1
Optic chiasm (V_{mean}=0.1 cm^3)	$D_{2\%}$ (Gy)	24.7	23.7	11.0	9.3
	D_{mean} (Gy)	22.9	22.0	10.0	6.7
	$V_{6/8/10}$ (%)	1.0	1.0	≤1.0	<0.5
Left optic nerve (V_{mean}=0.1 cm^3)	$D_{2\%}$ (Gy)	22.1	23.2	10.4	7.4
	D_{mean} (Gy)	17.9	17.4	9.2	6.0
	$V_{6/8/10}$ (%)	1.0	1.0	≤1.0	≤0.5
Right optic nerve (V_{mean}=0.1 cm^3)	$D_{2\%}$ (Gy)	20.2	19.1	9.0	4.5
	D_{mean} (Gy)	16.9	14.2	8.3	3.8
	$V_{6/8/10}$ (%)	0.1	0.1	0.1	0.1

Table 2 continued

Spinal cord (V_{mean}=3.7 cm^3)	$D_{2\%}$ (Gy)	5.5	3.3	<1	<1
	D_{mean} (Gy)	1.0	0.6	0.2	0.2
	$V_{8/10/12}$ (%)	<0.3	0	0	0
Left lens (V_{mean}=0.2 cm^3)	D_{max} (Gy)	3.4	1.4	<0.1	<0.1
Right lens (V_{mean}=0.2 cm^3)	D_{max} (Gy)	5.6	2.7	1.7	1.5
Brain – PTV (P1&P2) (V_{mean}= 30 cm^3)	$D_{2\%}$ (Gy)	22.5	18		
	D_{mean} (Gy)	11	7.7		
	$V_{10/12}$ (%)	49/35	52/32		
Brain – PTV (P3&P4) (V_{mean}= 36.6 cm^3)	$D_{2\%}$ (Gy)			10.7	11.4
	D_{mean} (Gy)			5.3	5.3
	$V_{10/12}$ (%)			≤4	≤8

3.3.2 MRI features of the irradiated pig brain

The original plan was to acquire MR images of the brain at 3 and 6 months post-irradiation on a 3 T scanner to potentially detect early-delayed pathology and late-onset RIBI. Our first group of pigs (P1 and P2) developed obvious neurological deficits (left head tilt and left circling) as early as 2 months post-irradiation. One pig (P2) had to be euthanized at 3 months post-irradiation due to inability to stand, which we believe was due to a lesion observed in the brainstem on MRI (figure not shown). The other pig (P1) was euthanized at 4 months as the neurological deficits grew significantly worse and the pig's balance was significantly impaired. Anatomical MR images of this second pig show that at 3 months post-irradiation, there is diffuse enhancement on T2-weighted imaging with minimal enhancement on post-contrast T1-weighted imaging (Fig. 10 top row) which is consistent with RIBI but occurs much sooner than expected. By 4 months post-irradiation, the observed pathology became much more extensive based on both T2-weighted and post-contrast T1-weighted enhancement (Fig. 10 middle row), with massive amounts of edema that led to a midline shift and collapse of the lateral ventricle. Our second group of pigs (P3 and

P4) showed no signs of neurological deficits throughout the entire 6 month follow-up duration. Anatomical MR images showed no abnormal T2-weighted or post-contrast T1-weighted enhancements at 3 and 6 months post-irradiation for both P3 (Fig. 10 bottom row) and P4.

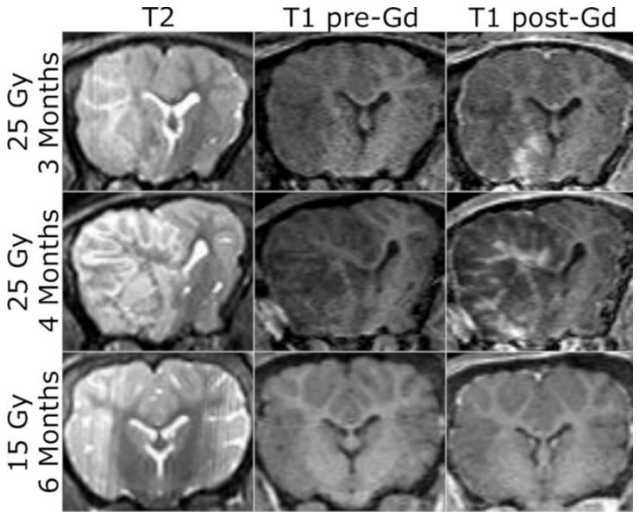

Figure 10. Anatomical MRI after irradiation of the left hemisphere of the mini-pig brain for Pig 1. Diffuse enhancement is seen on T2-weighted imaging with mass effect with foci of enhancement on post-contrast T1-weighted imaging.

3.3.3 Histological features of the irradiated pig brain

After euthanasia and macroscopic evaluation, we used hematoxylin and eosin (H&E) and Luxol Fast Blue (LFB) staining to validate our MRI findings. Macroscopic examination of the tissue before sectioning confirmed the MRI findings with obvious mass effect shifting the midline, disruption of the white matter, and likely focal hemorrhages. Examination of the H&E sections from the pigs that received a dose of 25 Gy (Fig. 11 top row) evidenced extensive cerebral (mostly unilateral) necrosis with associated inflammation (glial cells and glitter cells), vasculitis, vascular wall necrosis, thrombosis, dystrophic mineralization and loss of myelin. The contralateral hemisphere only had pathology near the midline. Though the lesions are more severe in the white matter, pathology can also be found in the gray matter. The lesions are also not homogenous suggesting that there might be a mixture of both types of pathologies consistent with the MRI. These changes are consistent with has been previously observed histologically in RIBI [16] and radiation necrosis [17]. In contrast, for pigs that received a dose of 15 Gy (Fig. 11 bottom row) no apparent pathological changes were evident on either macroscopic or microscopic examination.

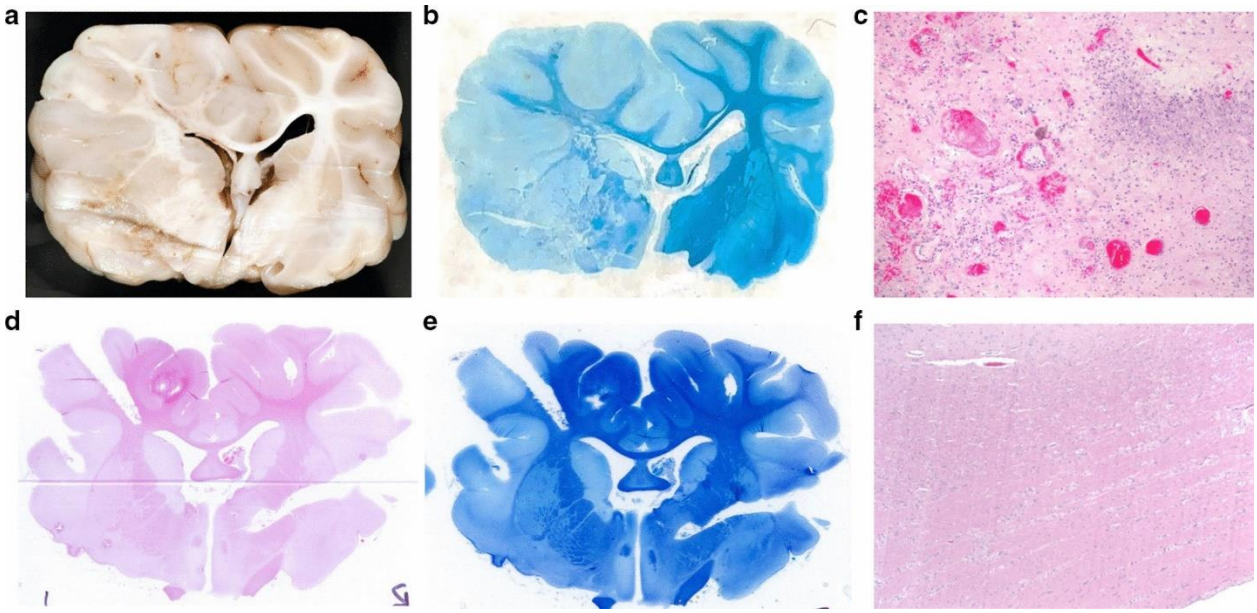

Figure 11. Histological changes in the pig brain after 25 Gy irradiation. The section was chosen to be in roughly the same location as the MRI data shown in Fig. 10. a Macroscopic examination is consistent with the MRI findings with mass effect and disrupted white matter. b Wide field picture of the Luxol-Fast Blue stained section shows clear demyelination of the left hemisphere as expected of RIBI. c × 10 magnification of the hematoxylin and eosin shows vascular changes and inflammatory infiltration suggestive of radiation necrosis. In the case of 15 Gy, wide field pictures of the H&E (d) and LFB (E) as well as × 10 magnification of the H&E (F) look normal.

3.4 Discussion

With advancements in radiation therapy techniques and improved efficacy in treating disease, the prognosis and median survival time with inoperable brain tumors is constantly improving [1, 2]. However, this also means that late adverse effects from neurocranial radiation therapy are becoming increasingly recognized [18]. Establishing an improved animal model for RIBI is imperative to facilitate the development of treatments for RIBI in both human and veterinary medicine. The use of clinical standard radiotherapy and MR imaging protocols in our study not only allows for the treatment and diagnosis of RIBI in our pig model, but also increases the translational value of the model. The model presented here improves upon the common rodent models in that pathology can be detected in MRI like in human patients. Our model also improves on prior work in pigs as that work relied on an electron beam for irradiation which led to an overestimation of the dose delivered to the brain.

Here, we present a pig model of RIBI generated with an IMRT half-brain treatment plan. The radiation treatment provides a homogeneous dose distribution throughout the PTV leading to

pathology limited to the PTV as evidenced on clinically standard MRI and histopathology. As expected, late-onset RIBI pathology was detected primarily in the irradiated hemisphere but only for those animals that received 25 Gy. RIBI pathology on MRI became more severe over time, which is consistent with previous descriptions of RIBI [18]. These results demonstrate that our clinical methodology is well-suited to produce late-onset RIBI pathology that is restricted to the irradiated regions of the pig brain. Prior reports in pig models [8, 9], were limited by the use of a 12 meV electron beam without correction for the skull which led to an overestimation of dose delivered to the brain. Our approach uses clinically relevant 6 MV photons with standard treatment planning technique (IMRT), clinical validation, and quality assurance to ensure the dose delivered is the dose that was planned. In comparison to established rodent models [7, 19], in this pig model we can detect abnormalities with anatomical MRI consistent with standard clinical approaches. Furthermore, white matter damage detected by H&E and LFB staining is not only more obvious than previously observed in the mouse brain, but it is also correlated with the anatomical lesions detected by MRI. Together, these data suggest that IMRT is a feasible treatment delivery for a pre-clinical pig model of late-onset RIBI that is more accurate than current rodent models.

3.5 Conclusions

While this work shows that a mini-pig model of RIBI is feasible, there remains some details that need to be improved upon. Work still needs to be done to optimize the target radiation dose and the time that observations are made to comprehensively study the development of diffuse white matter lesions, which have been observed in RIBI [20, 21]. Although a 25 Gy dose was able to produce clear MRI pathology in both P1 and P2, the onset was earlier than expected and the pathology progressed to radiation necrosis with unacceptably severe neurological impairment. However, a 15 Gy dose was unable to induce any MRI abnormalities or histopathology up to 6 months post-irradiation. This suggests that a suitable dose to produce diffuse lesions within a pig brain lies within the window of 15 Gy to 25 Gy. Additionally, it will be important to assess cognitive deficits in this model and how it relates to the lesions detected on MRI and histology. An additional constraint of our current results is the use of a hemispheric model where the unirradiated hemisphere serves as an internal control. A whole-brain model may be more ideal for evaluation of cognitive deficits. A major advantage of the larger pig brain and our approach is the

possibility to generate very specific irradiation plans of brain substructures. This could be leveraged for a more precise model of hippocampal-avoidance whole brain radiotherapy.

3.6 Acknowledgements

We would like to thank the following core facilities for their support in completing this work: Purdue Pre-Clinical Research Laboratory, Purdue Life Science MRI facility, Indiana Animal Disease Diagnostic Laboratory, and Purdue Histology Research Laboratory. This publication was made possible, in part, with support from the Indiana Clinical and Translational Sciences Institute funded, in part by Grant Number UL1TR002529 from the National Institutes of Health, National Center for Advancing Translational Sciences, Clinical and Translational Sciences Award. Also, the Purdue Life Science MRI facility is supported by grant S10OD012336 from the National Institutes of Health.

3.7 References

1. Stupp R, Hegi ME, Mason WP, van den Bent MJ, Taphoorn MJ, Janzer RC, et al. Effects of radiotherapy with concomitant and adjuvant temozolomide versus radiotherapy alone on survival in glioblastoma in a randomised phase III study: 5-year analysis of the EORTC-NCIC trial. The Lancet Oncology. 2009;10:459–66.

2. Evans AE, Jenkin RDT, Sposto R, Ortega JA, Wilson CB, Wara W, et al. The treatment of medulloblastoma. Results of a prospective randomized trial of radiation therapy with and without CCNU, vincristine, and prednisone. Journal of Neurosurgery. 1990;72:572–82.

3. Nwachukwu CR, Youland RS, Chioreso C, Wetjen N, NageswaraRao A, Keating G, et al. Health related quality of life (HRQOL) in long-term survivors of pediatric low grade gliomas (LGGs). J Neurooncol. 2014;121:599–607.

4. Valk PE, Dillon WP. Radiation injury of the brain. AJNR Am J Neuroradiol. 1991;12:45–62.

5. Lawrence YR, Li XA, el Naqa I, Hahn CA, Marks LB, Merchant TE, et al. Radiation dose-volume effects in the brain. Int J Radiat Oncol Biol Phys. 2010;76:S20-27.

6. Lee D-S, Yu M, Jang H-S, Kim Y-S, Choi B-O, Kang Y-N, et al. Radiation-induced brain injury: retrospective analysis of twelve pathologically proven cases. Radiation Oncology Journal. 2011;29:147.

7. Rancilio NJ, Dahl S, Athanasiadi I, Perez-Torres CJ. Design, construction, and in vivo feasibility of a positioning device for irradiation of mice brains using a clinical linear accelerator and intensity modulated radiation therapy. International Journal of Radiation Biology. 2017;93:1321–6.

8. Miot E, Hoffschir D, Alapetite C, Gaboriaud G, Pontvert D, Fetissof F, et al. Experimental MR study of cerebral radiation injury: quantitative T2 changes over time and histopathologic correlation. American Journal of Neuroradiology. 1995;16:79–85.

9. Miot-Noirault E, Akoka S, Hoffschir D, Pontvert D, Gaboriaud G, Alapetite C, et al. Potential of T2 relaxation time measurements for early detection of radiation injury to the brain: experimental study in pigs. American Journal of Neuroradiology. 1996;17:907–12.

10. Rancilio NJ, Bentley RT, Plantenga JP, Parys MM, Crespo BG, Moore GE. Safety and feasibility of stereotactic radiotherapy using computed portal radiography for canine intracranial tumors. Vet Radiol Ultrasound. 2017;

11. Bentzen SM, Constine LS, Deasy JO, Eisbruch A, Jackson A, Marks LB, et al. Quantitative Analyses of Normal Tissue Effects in the Clinic (QUANTEC): An Introduction to the Scientific Issues. Int J Radiat Oncol Biol Phys. 2010;76:S3–9.

12. Landberg T, Chavaudra J, Dobbs J, Gerard J-P, Hanks G, Horiot J-C, et al. Report 62: Prescribing Recording and Reporting Photon Beam Therapy (Supplement to ICRU report 50). J ICRU. Oxford Academic; 1999;os32:NP-NP.

13. 4. Definition of Volumes. J ICRU. Oxford Academic; 2010;10:41–53.

14. Torrens M, Chung C, Chung H-T, Hanssens P, Jaffray D, Kemeny A, et al. Standardization of terminology in stereotactic radiosurgery: Report from the Standardization Committee of the International Leksell Gamma Knife Society: special topic. J Neurosurg. 2014;121 Suppl:2–15.

15. Paddick I. A simple scoring ratio to index the conformity of radiosurgical treatment plans. Technical note. J Neurosurg. 2000;93 Suppl 3:219–22.

16. Lai R, Abrey LE, Rosenblum MK, DeAngelis LM. Treatment-induced leukoencephalopathy in primary CNS lymphoma: a clinical and autopsy study. Neurology. 2004;62:451–6.

17. Perry A, Schmidt RE. Cancer therapy-associated CNS neuropathology: an update and review of the literature. Acta Neuropathol. 2006;111:197–212.

18. Greene-Schloesser D, Robbins ME, Peiffer AM, Shaw EG, Wheeler KT, Chan MD. Radiation-induced brain injury: A review. Front Oncol. 2012;2:73.

19. Atwood T, Payne VS, Zhao W, Brown WR, Wheeler KT, Zhu J-M, et al. Quantitative Magnetic Resonance Spectroscopy Reveals a Potential Relationship between Radiation-Induced Changes in Rat Brain Metabolites and Cognitive Impairment. Radiation Research. 2007;168:574–81.

20. Reddick WE, Shan ZY, Glass JO, Helton S, Xiong X, Wu S, et al. Smaller white-matter volumes are associated with larger deficits in attention and learning among long-term survivors of acute lymphoblastic leukemia. Cancer. 2006;106:941–9.

21. Bompaire F, Lahutte M, Buffat S, Soussain C, Ardisson AE, Terziev R, et al. New insights in radiation-induced leukoencephalopathy: a prospective cross-sectional study. Support Care Cancer. 2018;26:4217–26.

CHAPTER 4. DIFFUSION, METABOLIC, AND HISTOLOGICAL CHARACTERISTICS OF A MINI-PIG MODEL OF RADIATION-INDUCED BRAIN INJURY

4.1 Introduction

Radiation therapy is commonly used to treat primary and metastatic brain tumors in adult and pediatric patients [1]. As ionizing radiation is delivered to the tumor site, surrounding healthy brain tissue is inevitably subject to irradiation as well. These normal tissue injuries typically manifest into a treatment-related side effect known as radiation-induced brain injury (RIBI), which can further be described based on the injury's time of clinical expression [2]. For instance, acute and early-delayed RIBI occur up to 6 months post-irradiation and have been found to be resolve spontaneously or with steroid administration. These early injuries therefore do not have a significant long-term impact on the patient's quality of life [3]. On the other hand, late-delayed RIBI occurs at least 6 months post-irradiation and has been shown to be irreversible and progressive [4]. Late-delayed RIBI therefore poses a major clinical problem for post-treatment care.

Non-invasive *in vivo* techniques such as diffusion tensor imaging (DTI) and magnetic resonance spectroscopy (MRS) can be used to characterize radiation-induced diffusion and metabolic changes within the brain. DTI measures the diffusion of water molecules along various tissue types in the brain. Since white matter is composed of axon fibers, the diffusion of water molecules within this tissue is highly directional. In comparison, gray matter is usually less directional and cerebrospinal fluid has no direction. Therefore, this imaging technique is most ideal for assessing the microstructural integrity of white matter since a deviation in its highly directional diffusion can be indicative of potential injury [5]. DTI studies of human patients that have previously undergone radiation therapy have exhibited decreases in fractional anisotropy (FA) values and increases in apparent diffusion coefficient (ADC) measurements after cranial irradiation [6–9]. MRS, on the other hand, identifies and quantifies the metabolites within the brain that exist in millimolar concentrations. These metabolites provide information regarding the energy status and overall viability of CNS cells. Therefore, this technique is ideal for evaluating neuronal and glial injury within the brain [10]. MRS studies of human patients that have undergone

radiation therapy have consistently shown that N-acetylaspartate (NAA) decreases after treatment [11–14].

While radiation-induced changes in diffusion and metabolic characteristics have been evidenced in human populations, they have yet to be evaluated in a mini-pig model of RIBI. Additionally, immunohistochemical (IHC) staining will be performed not only to investigate histological similarities between the mini-pig brain and human brain, but also to validate our imaging and spectroscopic findings. Therefore, the objective of this present study is to characterize the changes in diffusion, metabolite, and histological properties between the irradiated vs. unirradiated hemisphere at various time points post-irradiation.

4.2 Methods

4.2.1 Subjects

This study serves as a descriptive extension of the feasibility study described in the previous chapter. To reiterate, three-month old male Yucatan mini-pigs (n=4) were obtained and housed in pairs within a large-animal research facility throughout the duration of this experiment. A commercial feed was provided twice a day with water given ad libitum. The animals were observed on a weekly basis for signs of neurological impairment. All procedures in this study were approved by the Purdue Animal Care and Use Committee.

4.2.2 Irradiation procedure

A comprehensive protocol regarding radiation treatment planning and delivery for this single hemisphere model of RIBI has been established in the previous chapter. In short, the four pigs were split into pairs; one pair formed the 25 Gy cohort (P1 and P2) while the remaining pair formed the 15 Gy cohort (P3 and P4). A single-fraction 25 Gy dose was chosen to irradiate first cohort based on previous pig models of RIBI [15,16]. In contrast, a single-fraction 15 Gy dose was designated for the second cohort based on biological effective dose equivalency with a commonly prescribed fractionated whole brain irradiation dose (2 Gy × 30 fractions; $\alpha/\beta = 3$).

Under anesthesia, each pig was immobilized in the prone position with an individualized bite plate and a thermoplastic mask fixed on an indexable frame (Uniframe Baseplate, Civco Medical Solutions, Orange City, IA). The left hemispheres were irradiated with the corresponding

cohort-appropriate dose using a 6 MV linear accelerator (Varian 6EX, Varian Medical Systems, Inc. Palo Alto, CA) with a 120-leaf multileaf collimator (Millennium 120 MLC, Varian Medical Systems, Palo Alto, CA). The right hemisphere served as an internal control for each animal. However, it must be noted that the contralateral hemisphere does receive a small amount of irradiation and should not be assumed to be perfectly normal. Also, there is the possibility of biological processes crossing over from the irradiated to the contralateral hemisphere.

4.2.3 DTI and MRS procedure

All imaging procedures henceforth were performed in addition to the anatomical MRI acquisition described in the previous chapter. Diffusion tensor imaging (DTI) and magnetic resonance spectroscopy (MRS) were conducted using a 3T MRI unit (MAGNETOM® Prisma, Siemens Medical Solutions, Malvern, PA) at 1 week pre-irradiation, 3 months post-irradiation (P2), and either 4 months (P1) or 6 months (P3 and P4) post-irradiation. During each imaging time point, the pigs were placed under anesthesia while in the prone position and fitted with a 64-channel head coil.

DTI measurements for the 25 Gy cohort was acquired using a single-shot echo-planar imaging sequence. The following parameters were used for the DTI acquisition of the 25 Gy cohort: TR=15,300 ms, TE=87 ms, FOV=180 mm, matrix=1.3 mm x 1.3 mm, slice thickness=1.4 mm, number of slices=112, and 30 diffusion-weighting directions at a b-value= 1,000 s/mm^2 with 3 b0 images. FA maps and ADC maps for the 25 Gy cohort were computed inline during image acquisition using the sequence's MDDW diffusion mode. DTI measurements for the 15 Gy cohort were acquired using two protocols, which both possessed the following parameters: TR= 16,400 ms, TE=88 ms, FOV=180 mm, matrix=1.3 mm x 1.3 mm, slice thickness=1.4 mm, and number of slices=112. The sole difference was that the first protocol acquired 20 diffusion-weighting directions at a b-value=1,000 s/mm^2 with 1 b0 image while the second protocol acquired 12 diffusion-weighting directions at a b-value=2,000 s/mm^2 with 1 b0 image. FA maps and ADC maps for the 15 Gy cohort were computed by combining both sets of DTI acquisitions using an inhouse MATLAB program.

All DTI measurements were analyzed using ITK-SNAP software [17]. T2-weighted images, FA maps, and ADC maps were uploaded into a single workspace for each animal at each time point. Regions of interest (ROIs) were created by manually segmenting the target white matter

tract on the T2-weighted image, which thereafter ITK-SNAP automatically applied the segmentation overlay to the corresponding FA and ADC maps (Fig 12). Such target tracts are the left and right internal capsule (IC), and the left and right corpus callosum (CC). Average FA and ADC values were then calculated and exported through ITK-SNAP. This procedure was independently applied for the internal capsule and corpus callosum for both the ipsilateral and contralateral hemisphere over three consecutive imaging slices.

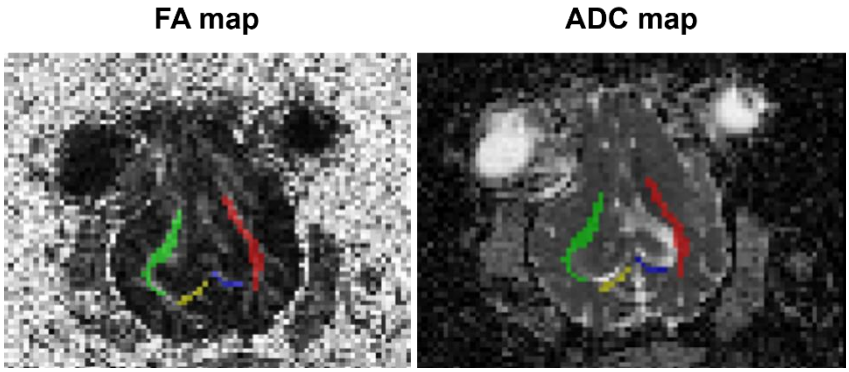

Figure 12. Representative outlines for regions of interest within the FA map (left) and ADC map (right). The green area indicates the left internal capsule, red indicates the right internal capsule, yellow indicates the left corpus callosum, and blue indicates the right corpus callosum.

Single-voxel MRS measurements were obtained using semi-LASER localization (TR=2,000 ms, TE=35 ms, averages=128, excite flip angle=90°, refocus flip angle=180°, VAPOR enabled) with previously acquired T2-weighted images as a reference for voxel placement. The volume of interest was centered in the periventricular brain region with the size of 10 x 10 x 15 mm^3 (Fig 13). Furthermore, water reference scans without water suppression were collected for frequency and phase correction. Automatic shimming with occasional manual shimming were performed to achieve optimal results.

The resulting spectra for all four animals were analyzed and quantified using LCModel (v.6.3-1B, Provencher 1993) and a basis set generated for a semi-LASER sequence with TE = 35 ms. For the purposes of this study, metabolite concentrations of N-acetylaspartate (NAA), glycerophosphocholine + phosphocholine (tCho), glutamate + glutamine (Glx), myo-inositol (mI), and creatine + phosphocreatine (tCr) for both ipsilateral and contralateral hemispheres were collected for each animal at each time point.

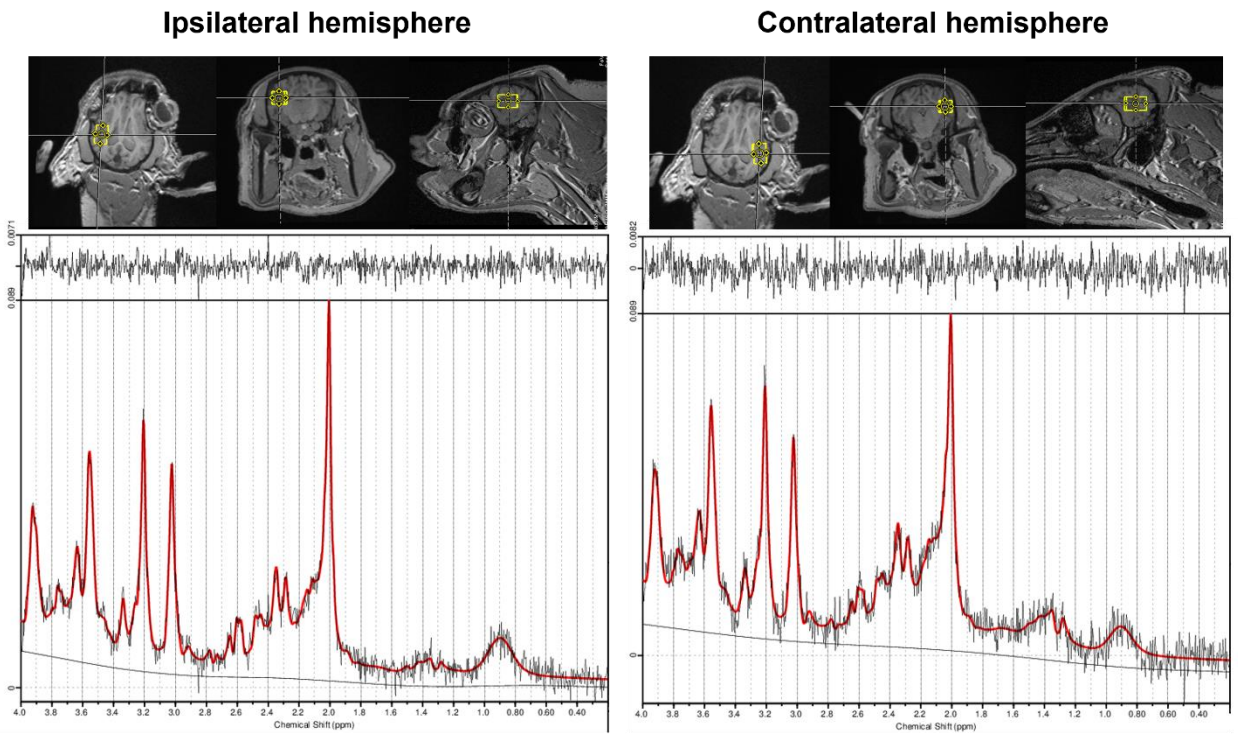

Figure 13. Representative voxel placements and their corresponding spectra within the ipsilateral and contralateral hemispheres. Voxel placements and their corresponding spectra are provided in Appendix B for all animals.

4.2.4 IHC staining procedure

IHC protocols were developed and validated by the Purdue University Histology Research Laboratory (HRL). One pig brain from the 25 Gy cohort (P1) and another from the 15 Gy cohort (P3) were chosen for examination using these histological methods. To begin, the animals were euthanized after the final imaging time point and their brain tissues were formalin-fixed, paraffin-embedded, and sectioned at 4 μm onto charged microscope slides. The slides were then incubated at 57°C for 30 minutes, immediately deparaffinized, and placed in a decloaking chamber for 20 minutes at 95°C for antigen retrieval. The tissues intended to be stained with anti-GFAP and anti-Iba-1 used EDTA as the retrieval buffer; DIVA was used for the remaining slides. Following antigen retrieval, tissues were cooled to 60°C, rinsed in Tris Buffer, and marked with a hydrophobic pen before being placed on the Biocare intelliPATH Automated IHC Staining System. Tissues underwent two blocking steps: first with 3% Hydrogen Peroxide, then with 2.5% Normal Goat Serum. The anti-C3 slides were blocked with 2.5% Normal Horse Serum. Next, the following primary antibodies were applied and incubated for 30 minutes: anti-GFAP antibodies

(ab7260; 1:1000) were used to detect astrocytes, anti-Iba-1 antibodies (ab178847; 1:8000) were used to detect microglia cells, anti-NeuN antibodies were used to identify post-mitotic neurons while anti-DCX antibodies (ab18723, 1:400) were used to identify neuronal precursor cells, anti-CD3 antibodies (A0452; 1:200) were used to mark T-cells, and anti-C3 antibodies (HM2168; 1:50) were used to mark the response of the complement system. $GFAP^+$ and Iba-1^+ cells would then comprise of the glial cell population for this study, $NeuN^+$ and DCX^+ cells would reflect the state of the neuronal population, and lastly, $CD3^+$ T-cells and $C3^+$ proteins would provide a glimpse into the animal's long-term immune response towards cranial radiation. After incubation, the slides were rinsed twice with buffer and a secondary antibody was applied for an additional 30 minutes. All antibodies, excluding anti-C3, were conjugated with Goat anti-Rabbit ImmPRESS HRP. The anti-C3 antibody was conjugated with Horse anti-Mouse 1:5 HRP. After two buffer rinses, the slides were dispensed with the chromogen, Vector ImmPACT DAB, for 5 minutes. Slides received a final buffer rinse and were removed from the automated stainer. Lastly, tissues were counterstained with Gill's II hematoxylin, dehydrated, and cover-slipped with a resinous mounting media.

The resulting slides were then imaged using an EVOS® XL (Life Technologies, Carlsbad, CA) digital inverted microscope at 20x magnification. Areas of analysis included the periventricular white matter for all cell populations, the surrounding gray matter for the glial cell population to investigate its potential influence on WM effects, and the cortical gray matter for the neuronal population to evaluate cellular effects within the cortex. As such, four images were acquired per area of analysis per hemisphere and analyzed using ImageJ software (v.1.8, NIH, Bethesda, MD). All cells were automatically counted using ImageJ's semi-automated thresholding and particle detection pipeline.

4.2.5 Statistical analysis

Statistical analyses were performed using SPSS (v.28.0, SPSS Inc., Chicago, IL). Each antibody stain was independently analyzed using a paired t-test with cell counts for the ipsilateral and contralateral hemispheres set as the comparison variables. Significance was established with $p \leq 0.05$ and corrected for multiple comparisons using the Holm-Sidak method when appropriate.

4.3 Results

The results we present here are a preliminary characterization of a mini-pig model of RIBI. Due to a sudden onset of severe neurological complications, the two pigs that had received a 25 Gy dose were euthanized at either 3 months or 4 months post-irradiation. Thus, evaluation of DTI and MRS data from the 25 Gy cohort includes data from the 0-month (P1 and P2), 3-month (P1 and P2), and 4-month (P1 only) time points. Histological evaluation of the 25 Gy cohort (P1 only) corresponds to the 4-month time point. All DTI and MRS measurements from the 15 Gy cohort includes data from the 0-month (P3 and P4), 3-month (P3 and P4), and 6-month (P3 and P4) time points. Histological evaluation of the 15 Gy cohort (P3 only) corresponds to the 6-month time point. MRS voxel placements and their respective spectra, complete tables of individual DTI and MRS data, as well as additional cohort data and their respective statistical analyses are provided in Appendix B.

4.3.1 Diffusion measurements vary between each animal with respect to time, white matter structure, and dose prescription

FA and ADC measurements undergo predictable radiation-induced changes within the ipsilateral IC of P1 after receiving a 25 Gy prescription dose. Indeed, FA values considerably and consistently decrease over time within the ipsilateral IC (0.58 ± 0.15 at 0 months, 0.29 ± 0.10 at 3 months, 0.14 ± 0.06 at 4 months) while FA values increase over time within the contralateral IC (0.41 ± 0.15 at 0 months, 0.59 ± 0.16 at 3 months, 0.62 ± 0.19 at 4 months; Fig 14a). ADC measurements, on the other hand, considerably and consistently increase over time within the ipsilateral IC (0.72 ± 0.09 at 0 months, 0.91 ± 0.15 at 3 months, 1.21 ± 0.32 at 4 months). Interestingly, ADC measurements also slightly increase over time within the contralateral IC (0.78 ± 0.20 at 0 months, 0.80 ± 0.17 at 3 months, 0.88 ± 0.34 at 4 months; Fig 14b).

Regarding the diffusion measurements within the CC of P1 after receiving a 25 Gy prescription dose, FA and ADC measurements marginally follow the typical radiation-induced assumption. Specifically, there is a slight decrease in FA between 3 to 4 months post-irradiation for both the ipsilateral CC (0.32 ± 0.11 at 0 months, 0.33 ± 0.11 at 3 months, 0.29 ± 0.11 at 4 months) and the contralateral CC (0.44 ± 0.15 at 0 months, 0.46 ± 0.14 at 3 months, 0.34 ± 0.11 at 4 months; Fig 14c). Additionally, there is an increase in ADC between 0 to 3 months post-irradiation for both the ipsilateral CC (0.94 ± 0.23 at 0 months, 1.14 ± 0.23 at 3 months, 1.10 ±

0.15 at 4 months) and the contralateral CC (0.85 ± 0.18 at 0 months, 1.11 ± 0.56 at 3 months, 1.11 ± 0.48 at 4 months; (Fig 14d).

FA and ADC measurements within both the ipsilateral and contralateral IC of P2 do not follow typical radiation-induced assumptions of diffusion after receiving a 25 Gy prescription dose. Indeed, FA values considerably increase over time within both the ipsilateral IC (0.52 ± 0.19 at 0 months, 0.61 ± 0.11 at 3 months) and the contralateral IC (0.41 ± 0.16 at 0 months, 0.67 ± 0.45 at 3 months; Fig 15a). ADC measurements, on the other hand, do not undergo any obvious radiation-induced changes from 0 to 3 months (Fig 15b).

Similar to the findings in the IC, there is a consistent change in FA measurements within both the ipsilateral and contralateral CC of P2 after receiving a 25 Gy prescription dose. Specifically, FA values considerably increase over time within the ipsilateral CC (0.35 ± 0.16 at 0 months, 0.55 ± 0.29 at 3 months) and the contralateral CC (0.38 ± 0.14 at 0 months, 0.58 ± 0.20 at 3 months; Fig 15c). ADC measurements, in contrast, decrease over time within the ipsilateral CC (0.86 ± 0.16 at 0 months, 0.75 ± 0.11 at 3 months) but not the contralateral CC (0.84 ± 0.14 at 0 months, 0.83 ± 0.20 at 3 months; Fig 15d).

FA and ADC measurements within both the ipsilateral and contralateral IC of P3 do not follow typical radiation-induced assumptions of diffusion after receiving a 15 Gy prescription dose. Indeed, there are no discernable patterns of change in both the ipsilateral and contralateral FA measurements of the IC (Fig 16a). ADC measurements, on the other hand, appear to slightly decrease between 0 to 3 months post-irradiation for both the ipsilateral IC (0.64 ± 0.09 at 0 months, 0.56 ± 0.10 at 3 months, 0.56 ± 0.06 at 6 months) and contralateral IC (0.65 ± 0.07 at 0 months, 0.58 ± 0.10 at 3 months, 0.59 ± 0.06 at 6 months; Fig 16b).

FA and ADC measurements undergo predictable radiation-induced changes over time within the ipsilateral CC of P3 after receiving a 15 Gy prescription dose. Specifically, FA values consistently decrease over time within the ipsilateral CC (0.50 ± 0.15 at 0 months, 0.45 ± 0.15 at 3 months, 0.36 ± 0.15 at 6 months) while FA values increase between 0 to 3 months within the contralateral CC (0.39 ± 0.13 at 0 months, 0.46 ± 0.19 at 3 months, 0.44 ± 0.20 at 6 months; Fig 16c). ADC measurements, in contrast, appear to consistently increase over time within the ipsilateral CC (0.75 ± 0.42 at 0 months, 0.80 ± 0.35 at 3 months, 1.09 ± 0.64 at 6 months) without any discernable patterns of change for the contralateral CC (0.94 ± 0.59 at 0 months, 0.73 ± 0.35 at 3 months, 1.16 ± 0.64 at 6 months; Fig 16d).

FA and ADC measurements within both the ipsilateral and contralateral IC of P4 do not follow typical radiation-induced assumptions of diffusion after receiving a 15 Gy prescription dose. Indeed, FA values increase between 0 to 3 months before decreasing between 3 to 6 months post-irradiation for both the ipsilateral IC (0.48 ± 0.14 at 0 months, 0.57 ± 0.20 at 3 months, 0.52 ± 0.17 at 6 months) and the contralateral IC (0.54 ± 0.15 at 0 months, 0.60 ± 0.15 at 3 months, 0.49 ± 0.16 at 6 months; Fig 17a). ADC measurements, on the other hand, do not decrease until the period between 3 to 6 months for the ipsilateral IC (0.64 ± 0.07 at 0 months, 0.64 ± 0.17 at 3 months, 0.55 ± 0.10 at 6 months) but slightly decreases between 0 to 3 months for the contralateral IC (0.64 ± 0.12 at 0 months, 0.59 ± 0.08 at 3 months, 0.60 ± 0.14 at 6 months; Fig 17b).

FA and ADC measurements within both the ipsilateral and contralateral CC of P4 do not follow typical radiation-induced assumptions of diffusion after receiving a 15 Gy prescription dose. Specifically, FA values within the ipsilateral CC decrease between 0 to 3 months before increasing between 3 to 6 months post-irradiation (0.38 ± 0.18 at 0 months, 0.35 ± 0.11 at 3 months, 0.42 ± 0.18 at 6 months). In contrast, FA values within the contralateral CC increase between 0 to 3 months before decreasing between 3 to 6 months post-irradiation (0.37 ± 0.12 at 0 months, 0.46 ± 0.16 at 3 months, 0.42 ± 0.16 at 6 months; Fig 17c). ADC measurements, on the other hand, do not undergo any obvious radiation-induced changes from 0 to 6 months (Fig 17d).

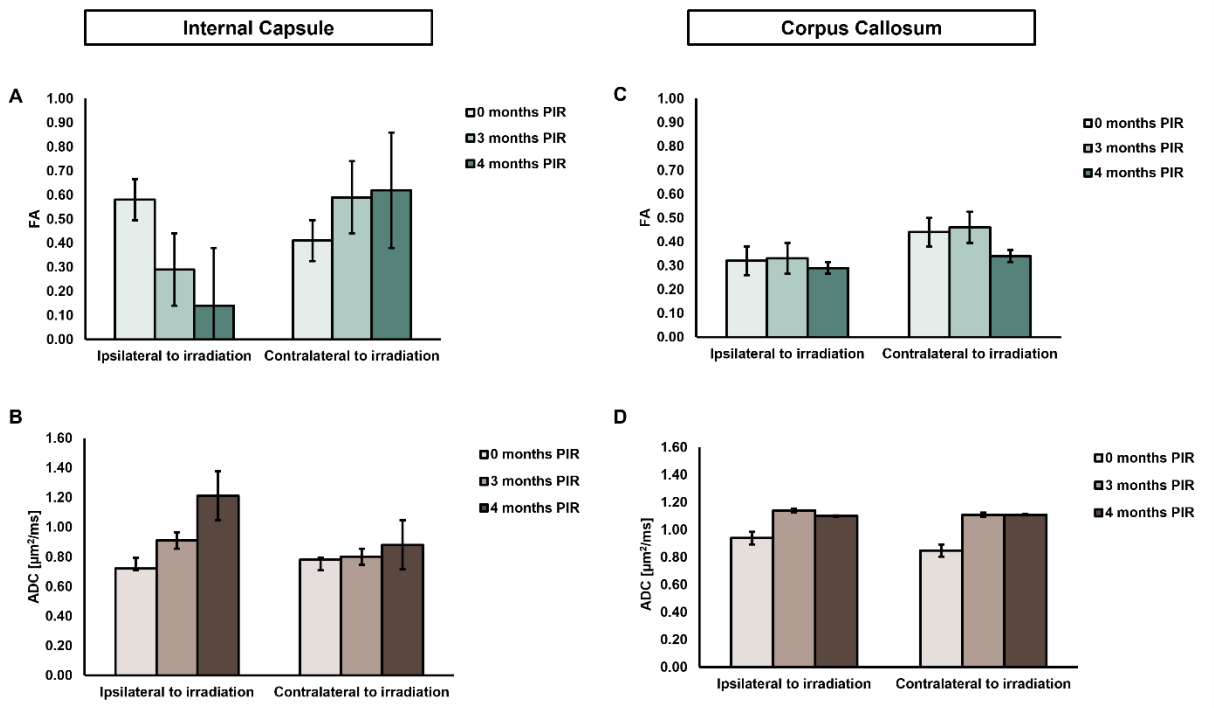

Figure 14. Changes in FA and ADC measurements over time within the internal capsule (a-b) and corpus callosum (c-d) white matter tracts after a 25 Gy irradiation (P1). Corresponding effects of the contralateral hemisphere are shown as a comparison. Error bars denote the standard error.

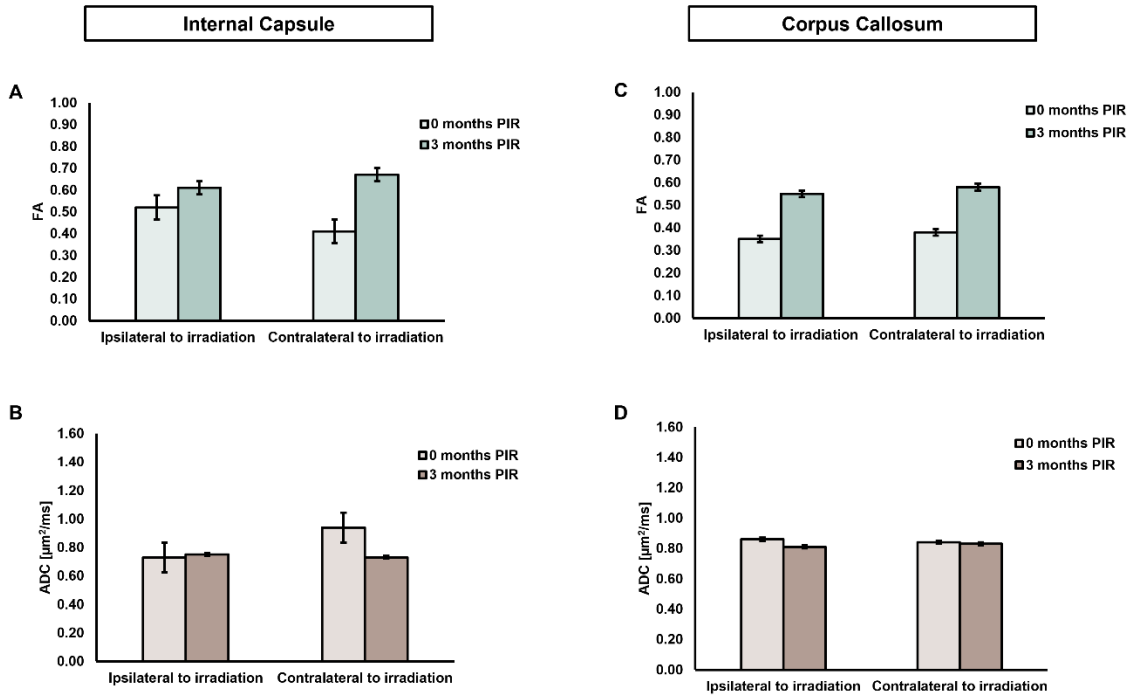

Figure 15. Changes in FA and ADC measurements over time within the internal capsule (a-b) and corpus callosum (c-d) white matter tracts after a 25 Gy irradiation (P2). Corresponding effects of the contralateral hemisphere are shown as a comparison. Error bars denote the standard error.

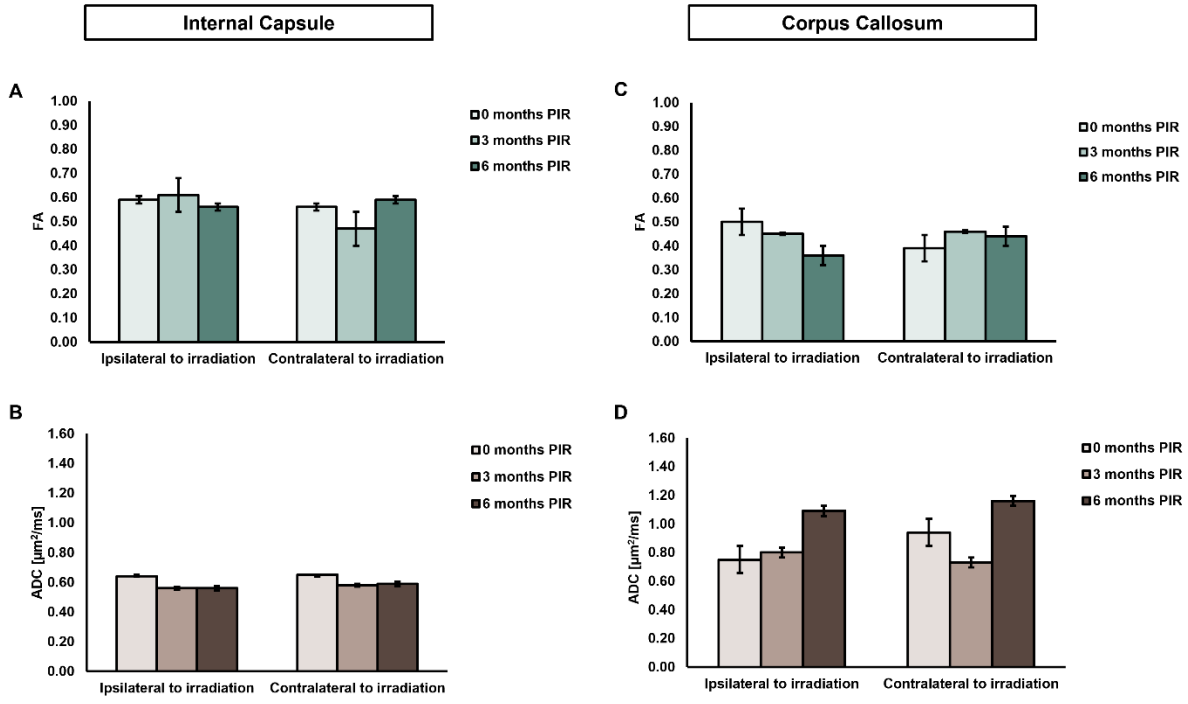

Figure 16. Changes in FA and ADC measurements over time within the internal capsule (a-b) and corpus callosum (c-d) white matter tracts after a 15 Gy irradiation (P3). Corresponding effects of the contralateral hemisphere are shown as a comparison. Error bars denote the standard error.

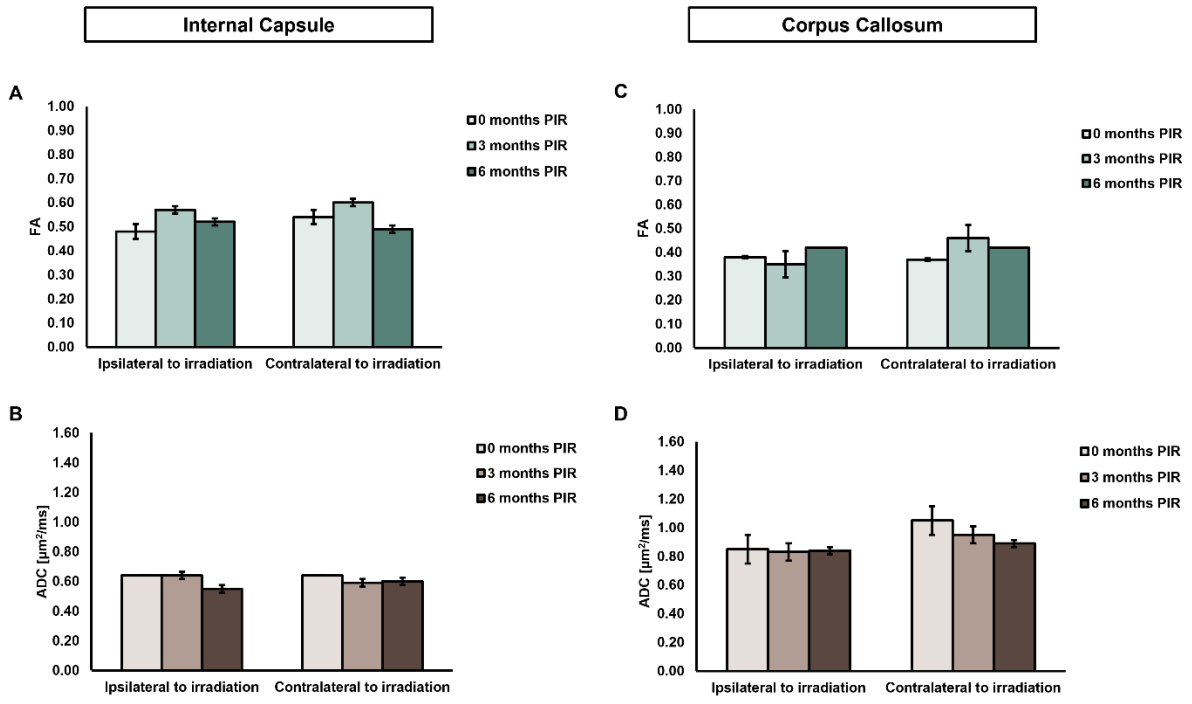

Figure 17. Changes in FA and ADC measurements over time within the internal capsule (a-b) and corpus callosum (c-d) white matter tracts after a 15 Gy irradiation (P4). Corresponding effects of the contralateral hemisphere are shown as a comparison. Error bars denote the standard error.

4.3.2 Metabolite concentrations vary between each animal with respect to time and dose prescription

MRS measurements from P1 reflect late neuronal injury, decreased membrane turnover, increased excitatory neurotransmission, loss of glial cell density, and alterations in energy metabolism up to 4 months post-irradiation. Late neuronal injury is represented by a decrease in ipsilateral NAA values between 3 to 4 months post-irradiation (3.17 at 0 months, 3.36 at 3 months, 2.30 at 4 months). There is also a slight decrease in contralateral NAA values (3.38 at 0 months, 4.92 at 3 months, 4.60 at 4 months), albeit not as much compared to the ipsilateral hemisphere (Fig 18a). Decreased membrane turnover is characterized by a slight decrease in ipsilateral tCho values over time (0.83 at 0 months, 0.74 at 3 months, 0.67 at 4 months) while contralateral tCho values increase over time (0.82 at 0 months, 1.63 at 3 months, 1.65 at 4 months; Fig 18b). Increased excitatory neurotransmission is described as an overall increase in ipsilateral Glx values over time (3.36 at 0 months, 12.44 at 3 months, 8.92 at 4 months). Interestingly, contralateral Glx values also

increase over time (6.70 at 0 months, 7.19 at 3 months, 8.31 at 4 months; Fig 18c). A loss of glial cell density is portrayed as a consistent and considerable decrease in ipsilateral mI values over time (3.94 at 0 months, 1.13 at 3 months, 0.00 at 4 months) while contralateral mI values increased between 0 to 3 months and decreased from 3 to 4 months post-irradiation (3.12 at 0 months, 4.28 at 3 months, 4.18 at 4 months; Fig 18d). An alteration in energy metabolism is expressed as an increase in ipsilateral tCr values between 0 to 3 months and a subsequent decrease in ipsilateral tCr values between 3 to 4 months post-irradiation (3.74 at 0 months, 4.87 at 3 months, 3.22 at 4 months). There is also an increase and subsequent decrease in contralateral tCr values (3.34 at 0 months, 4.02 at 3 months, 3.95 at 4 months), albeit not as obvious when compared to the ipsilateral values (Fig 18e).

MRS measurements from P2 reflect neuronal injury, increased membrane turnover, increased excitatory neurotransmission, loss of glial cell density, and increased energy metabolism up to 3 months post-irradiation. Late neuronal injury is represented by a slight decrease in ipsilateral NAA values over time (6.71 at 0 months, 6.46 at 3 months) while contralateral NAA values increase over time (6.57 at 0 months, 6.74 at 3 months; Fig 19a). Increased membrane turnover is characterized by an increase in ipsilateral tCho values over time within both the ipsilateral hemisphere (1.19 at 0 months, 1.52 at 3 months) and contralateral hemisphere (1.27 at 0 months, 1.84 at 3 months; Fig 19b). Increased excitatory neurotransmission is described as an increase in ipsilateral Glx values over time within both the ipsilateral hemisphere (5.40 at 0 months, 10.54 at 3 months) and contralateral hemisphere (7.34 at 0 months, 11.36 at 3 months; Fig 19c). A loss of glial cell density is portrayed as a decrease in ipsilateral mI values over time (5.44 at 0 months, 3.81 at 3 months) while contralateral mI values increase over time (4.79 at 0 months, 6.20 at 3 months; Fig 19d). Increased energy metabolism is expressed as an increase in ipsilateral tCr values over time within both the ipsilateral hemisphere (3.90 at 0 months, 5.62 at 3 months) and contralateral hemisphere (4.15 at 0 months, 5.35 at 3 months; Fig 19e).

MRS measurements from P3 reflect a lack of neuronal injury, increased membrane turnover, increased excitatory neurotransmission, loss of glial cell density, and early alterations in energy metabolism up to 6 months post-irradiation. A lack of neuronal injury is represented by a consistent increase in ipsilateral NAA values over time (6.37 at 0 months, 7.15 at 3 months, 7.43 at 6 months) while contralateral NAA values increase between 0 to 3 months and decrease from 3 to 6 months post-irradiation (7.24 at 0 months, 7.46 at 3 months, 6.96 at 6 months; Fig 20a).

Increased membrane turnover is characterized by a consistent increase in tCho values over time within both the ipsilateral (1.46 at 0 months, 1.87 at 3 months, 2.24 at 6 months) and contralateral hemispheres (1.86 at 0 months, 1.88 at 3 months, 2.06 at 6 months; Fig 20b). Increased excitatory neurotransmission is described as an overall increase in ipsilateral Glx values over time (8.96 at 0 months, 12.67 at 3 months, 10.77 at 6 months). Interestingly, contralateral Glx values also consistently increase over time (11.34 at 0 months, 12.37 at 3 months, 13.64 at 6 months; Fig 20c). A loss of glial cell density is portrayed as a consistent decrease in ipsilateral mI values over time (7.08 at 0 months, 6.55 at 3 months, 5.68 at 6 months) while contralateral mI values increase between 0 to 3 months and decrease between 3 to 6 months post-irradiation (6.11 at 0 months, 7.48 at 3 months, 6.27 at 6 months; Fig 20d). Early alterations in energy metabolism are expressed as an increase in ipsilateral tCr values between 0 to 3 months post-irradiation (4.21 at 0 months, 5.86 at 3 months, 5.86 at 6 months) while contralateral tCr values decrease between 0 to 3 months and increase between 3 to 6 months post-irradiation (5.48 at 0 months, 5.40 at 3 months, 5.91 at 6 months; Fig 20e).

MRS measurements from P4 reflect late neuronal injury, a late decrease in membrane turnover, increased excitatory neurotransmission, a late gain of glial cell density, and alterations in energy metabolism up to 6 months post-irradiation. Late neuronal injury is represented by a decrease in ipsilateral NAA values between 3 to 6 months post-irradiation (6.61 at 0 months, 7.37 at 3 months, 6.34 at 6 months) while contralateral NAA values increase between 3 to 6 months post-irradiation (6.91 at 0 months, 5.42 at 3 months, 7.06 at 6 months; Fig 21a). A late decrease in membrane turnover is characterized by a decrease in tCho values between 3 to 6 months post-irradiation within both the ipsilateral (1.61 at 0 months, 2.43 at 3 months, 2.19 at 6 months) and contralateral hemispheres (1.85 at 0 months, 2.01 at 3 months, 1.76 at 6 months; Fig 21b). Increased excitatory neurotransmission is described as an overall increase in ipsilateral Glx values over time (8.97 at 0 months, 15.38 at 3 months, 11.95 at 6 months) while contralateral Glx values remain overall consistent (12.90 at 0 months, 12.15 at 3 months, 12.98 at 6 months; Fig 21c). A late gain of glial cell density is portrayed as an increase in ipsilateral mI values between 3 to 6 months post-irradiation (5.65 at 0 months, 5.15 at 3 months, 5.41 at 6 months) while contralateral mI values consistently decrease over time (6.63 at 0 months, 6.49 at 3 months, 6.03 at 6 months; Fig 21d). An alteration in energy metabolism is expressed as an increase in ipsilateral tCr values between 0 to 3 months and a subsequent decrease in ipsilateral tCr values between 3 to 6 months

post-irradiation (4.59 at 0 months, 6.74 at 3 months, 4.94 at 6 months). In contrast, contralateral tCr values decrease between 0 to 3 months and subsequently increase between 3 to 6 months post-irradiation (5.10 at 0 months, 4.96 at 3 months, 5.37 at 6 months; Fig 21e).

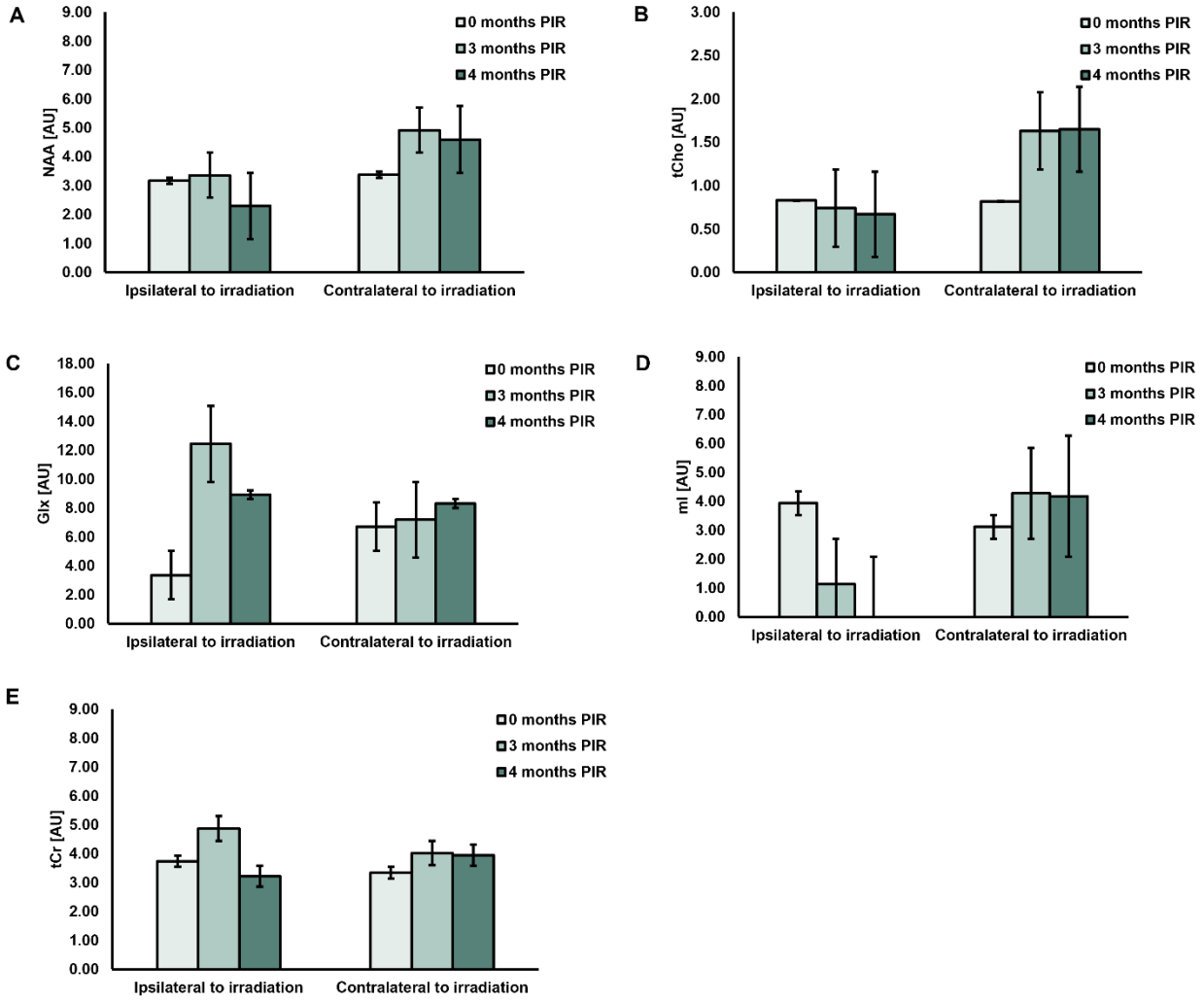

Figure 18. Changes to concentrations of (a) NAA, (b) tCho, (c) Glx, (d) mI, and (e) tCr over time after a 25 Gy irradiation (P1). Corresponding effects of the contralateral hemisphere are shown as a comparison. Error bars denote the standard error. AU is defined as arbitrary units.

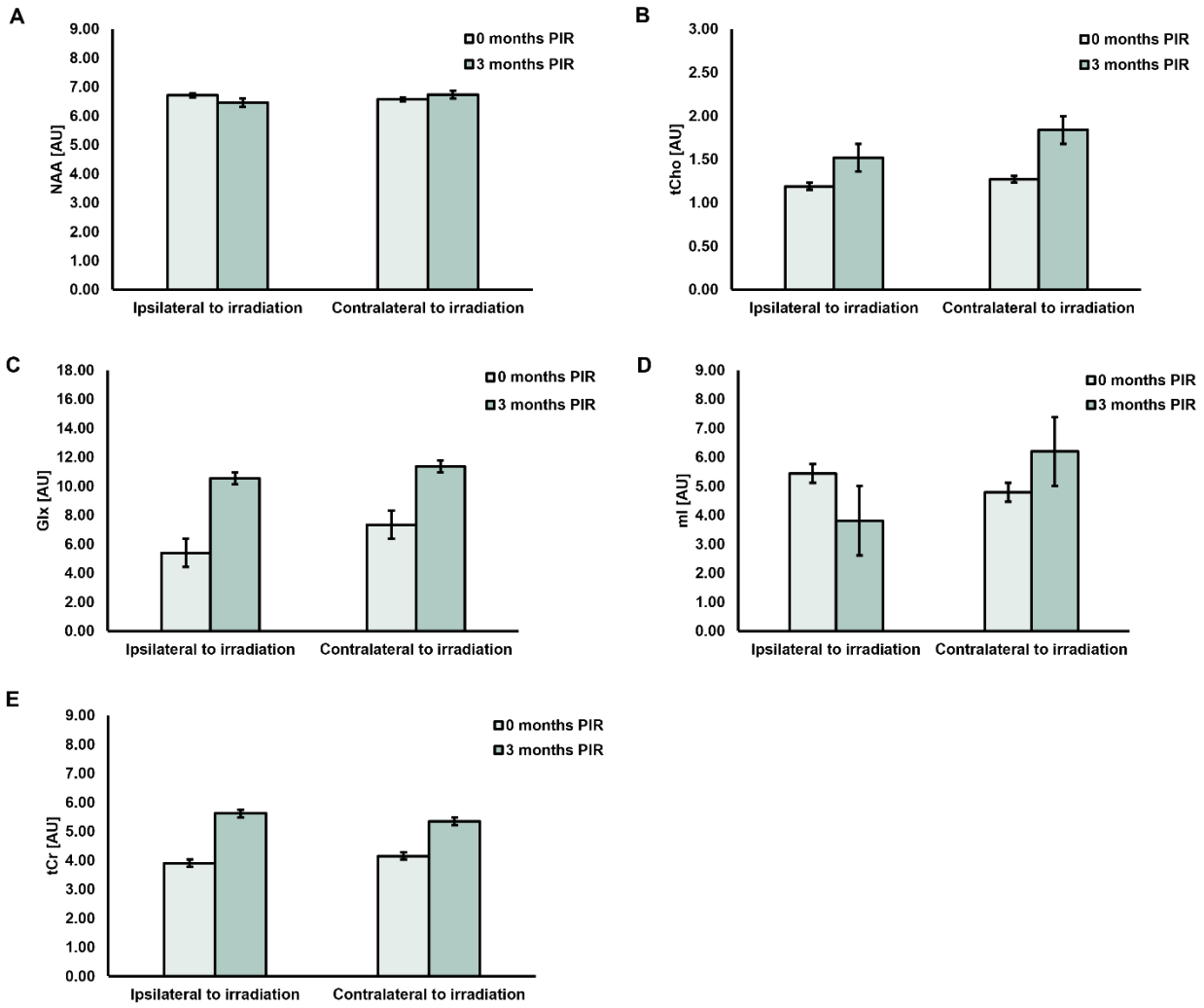

Figure 19. Changes to concentrations of (a) NAA, (b) tCho, (c) Glx, (d) mI, and (e) tCr over time after a 25 Gy irradiation (P2). Corresponding effects of the contralateral hemisphere are shown as a comparison. Error bars denote the standard error. AU is defined as arbitrary units.

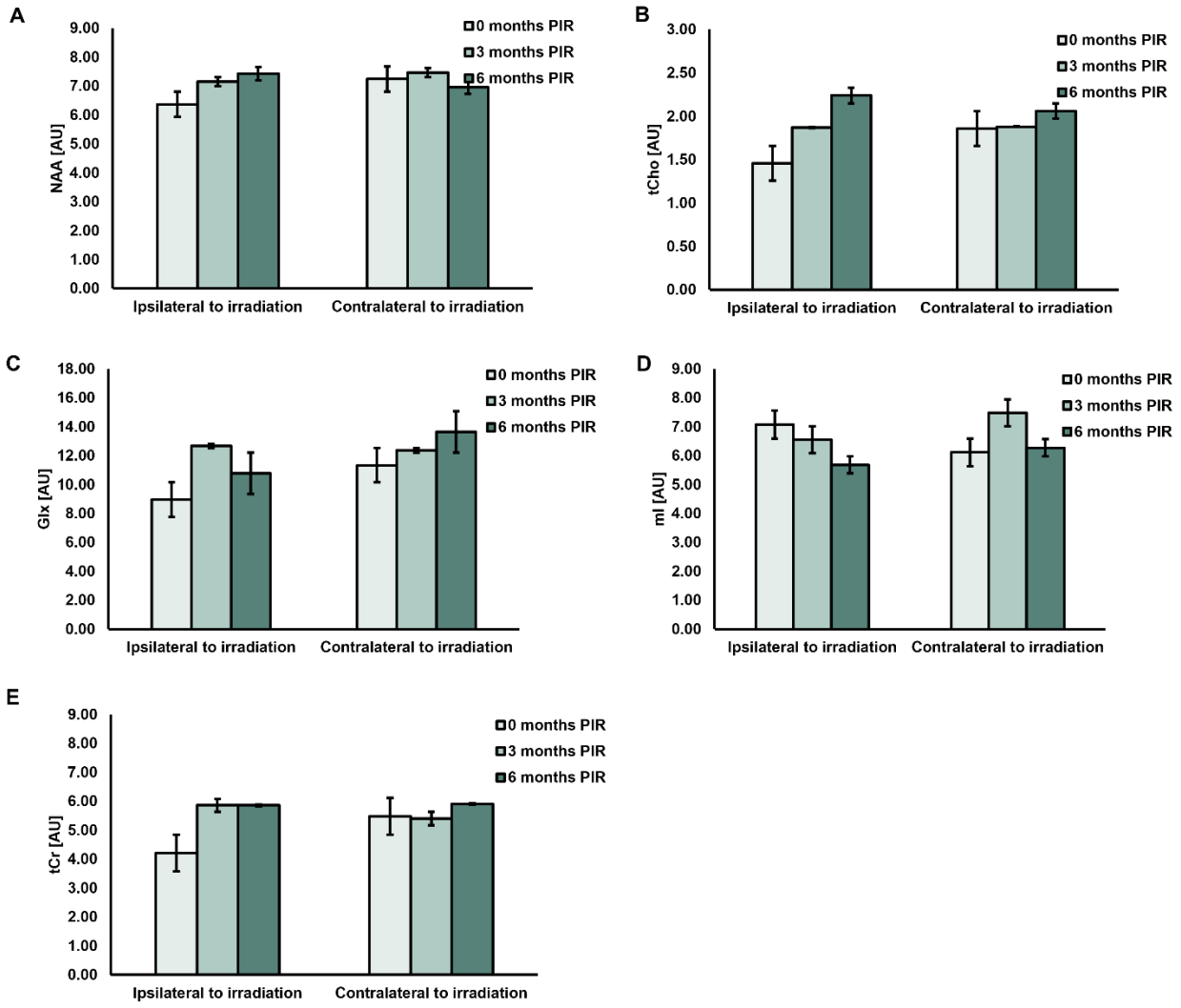

Figure 20. Changes to concentrations of (a) NAA, (b) tCho, (c) Glx, (d) mI, and (e) tCr over time after a 15 Gy irradiation (P3). Corresponding effects of the contralateral hemisphere are shown as a comparison. Error bars denote the standard error. AU is defined as arbitrary units.

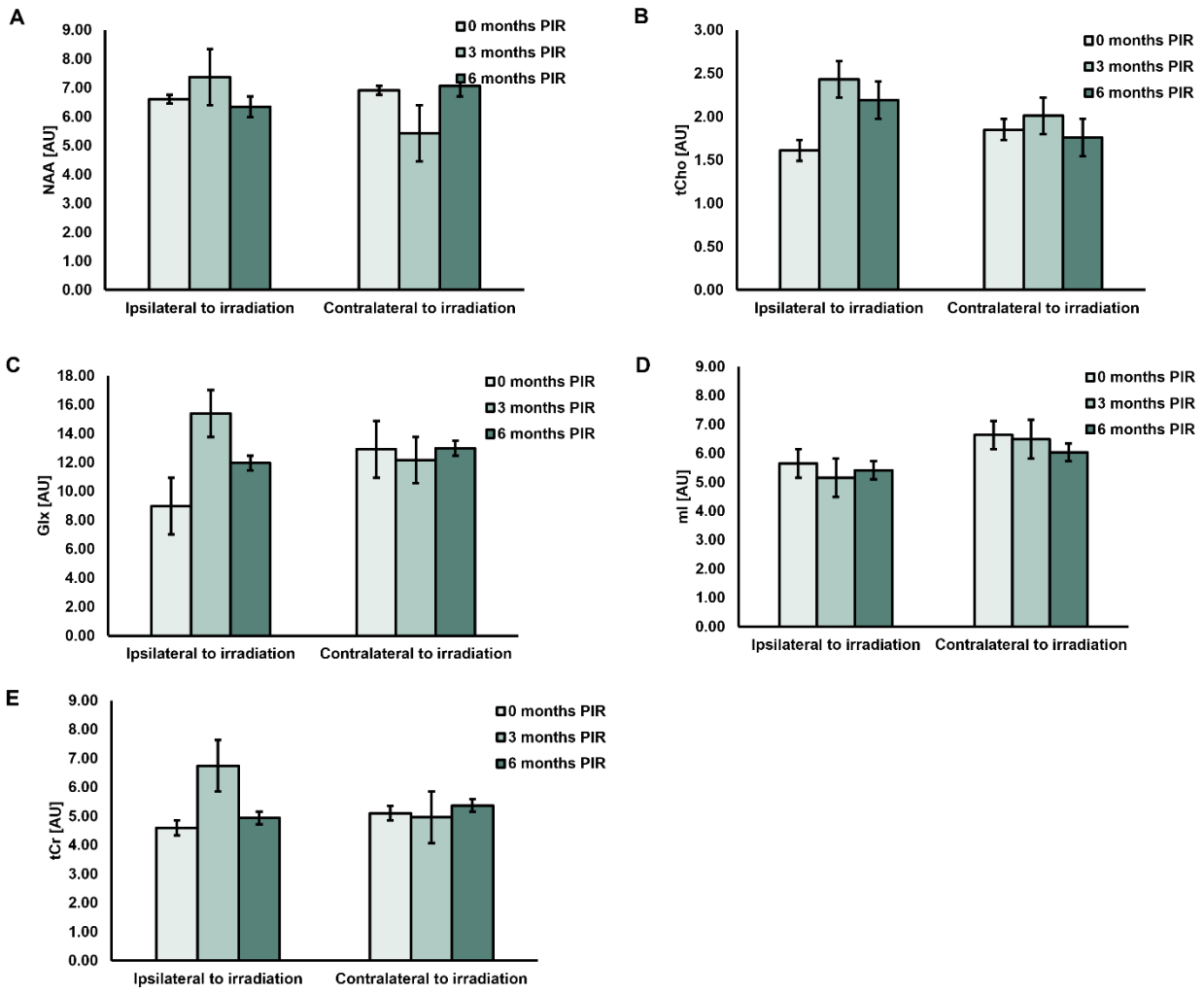

Figure 21. Changes to concentrations of (a) NAA, (b) tCho, (c) Glx, (d) mI, and (e) tCr over time after a 15 Gy irradiation (P4). Corresponding effects of the contralateral hemisphere are shown as a comparison. Error bars denote the standard error. AU is defined as arbitrary units.

4.3.3 Histological staining reveals dynamic radiation-induced changes in neuronal and glial cell populations

A 25 Gy prescription dose significantly changes the $NeuN^+$ and DCX^+ cell populations within the ipsilateral hemisphere; corresponding changes, however, do not occur for an irradiation dose of 15 Gy. A single fraction dose of 25 Gy significantly decreased the number of $NeuN^+$ cells in both white matter (WM-IRR vs WM-CTRL = $p<0.05$) and gray matter (GM-IRR vs GM-CTRL = $p<0.05$) at 3 months post-irradiation (Fig 18a). In contrast, no significant changes were observed in the number of $NeuN^+$ cells between hemispheres using a single fraction 15 Gy dose (Fig 18b).

Furthermore, a single fraction dose of 25 Gy significantly increased the number of DCX^+ cells in white matter (WM-IRR vs WM-CTRL = $p<0.05$) at 3 months post-irradiation (Fig 18c). Additionally, an increase in the number of DCX^+ cells was observed in GM at the 3-month time point, although the difference was not significant. Regarding the mini-pig that received a 15 Gy dose, no significant changes were seen in DCX^+ cells between hemispheres (Fig 18d).

Radiation elicited a significant change in $GFAP^+$ staining regardless of prescription dose; changes in Iba-1^+ staining, however, did not occur for any radiation dose. A single fraction dose of 25 Gy decreased the area of $GFAP^+$ staining within the ipsilateral WM (WM-IRR vs WM-CTRL = $p<0.05$; Fig 19a). Although no significant change in area of $GFAP^+$ staining was elicited in the GM after 25 Gy irradiation, both WM and GM regions show evidence of radiation-induced glial scarring (Fig 20). A single fraction dose of 15 Gy significantly decreased the percent area of $GFAP^+$ cells in both white matter and gray matter (WM-IRR vs WM-CTRL = $p<0.05$; GM-IRR vs GM-CTRL = $p<0.05$; Fig 19b). Interestingly, no significant changes are seen in the area of $Iba1^+$ cells after either 25 Gy (Fig 19c) or 15 Gy irradiation (Fig 19d) although the $Iba1^+$ cells appeared to display an activated morphology after irradiation (Fig 21).

Lastly, there were no detectable stains for either anti-C3 or anti-CD3 antibodies for either dose cohort.

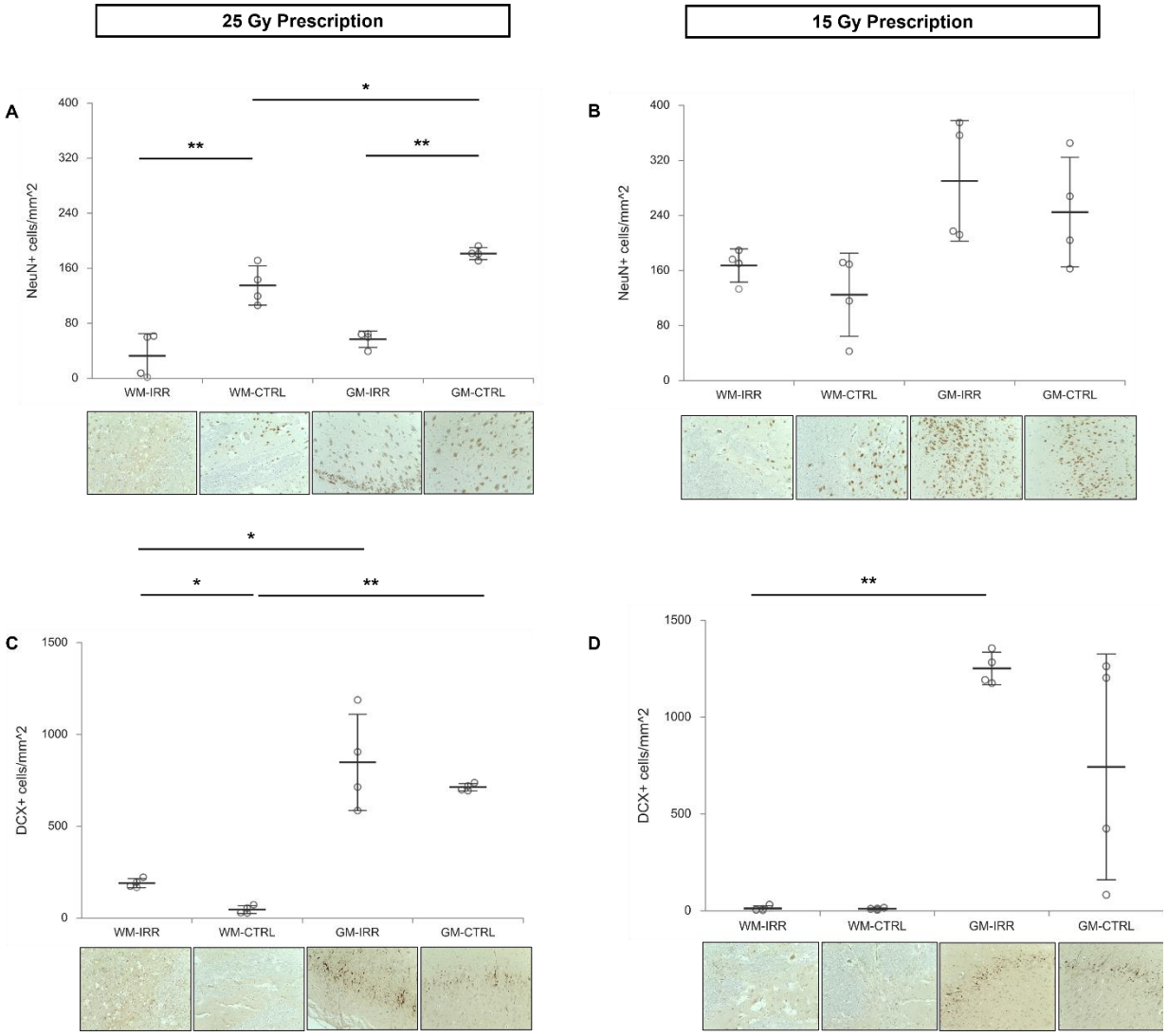

Figure 22. Effect of cranial irradiation on neuronal cell populations within the periventricular white matter (WM) and cortical gray matter (GM). (a) Changes in mature neuron cell density after a 25 Gy prescription dose within the ipsilateral hemisphere (WM-IRR and GM-IRR) are compared to the contralateral hemisphere (WM-CTRL and GM-CTRL). (b) Changes in mature neuron cell density after a 15 Gy prescription dose within the ipsilateral hemisphere are compared to the contralateral hemisphere. (c) Changes in immature neuron cell density after a 25 Gy prescription dose within the ipsilateral hemisphere are compared to the contralateral hemisphere. (d) Changes in immature neuron cell density after a 15 Gy prescription dose within the ipsilateral hemisphere are compared to the contralateral hemisphere. Error bars denote the standard error. * indicates a statistical significance of $p<0.05$. ** indicates a statistical significance of $p<0.001$.

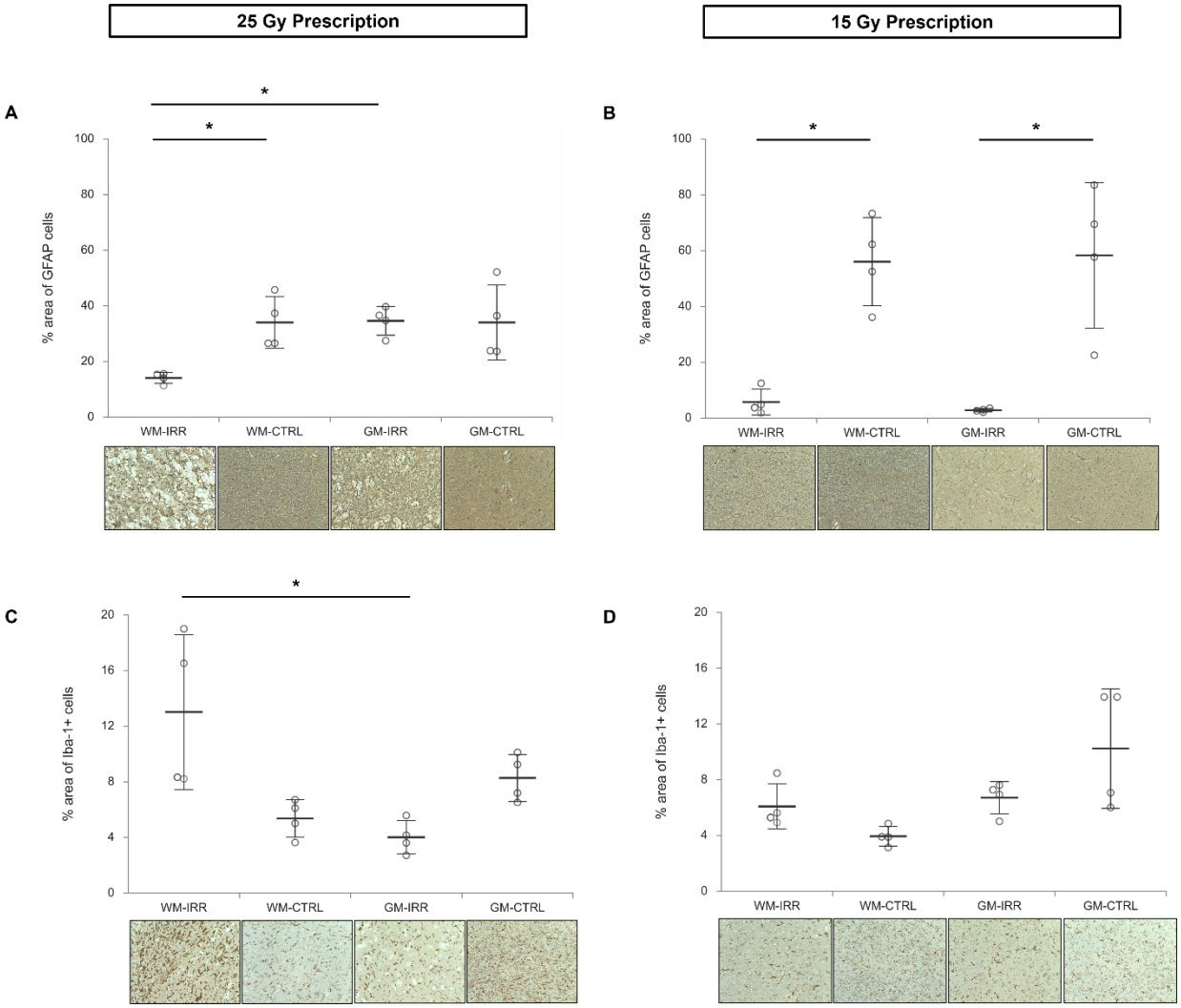

Figure 23. Effect of cranial irradiation on glial cell populations within the periventricular white matter (WM) and cortical gray matter (GM). (a) Changes in area of astrocytes after a 25 Gy prescription dose within the ipsilateral hemisphere (WM-IRR and GM-IRR) are compared to the contralateral hemisphere (WM-CTRL and GM-CTRL). (b) Changes in area of astrocytes after a 15 Gy prescription dose within the ipsilateral hemisphere are compared to the contralateral hemisphere. (c) Changes in area of microglia after a 25 Gy prescription dose within the ipsilateral hemisphere are compared to the contralateral hemisphere. (d) Changes in area of microglia after a 15 Gy prescription dose within the ipsilateral hemisphere are compared to the contralateral hemisphere. Error bars denote the standard error. * indicates a statistical significance of $p<0.05$. ** indicates a statistical significance of $p<0.001$.

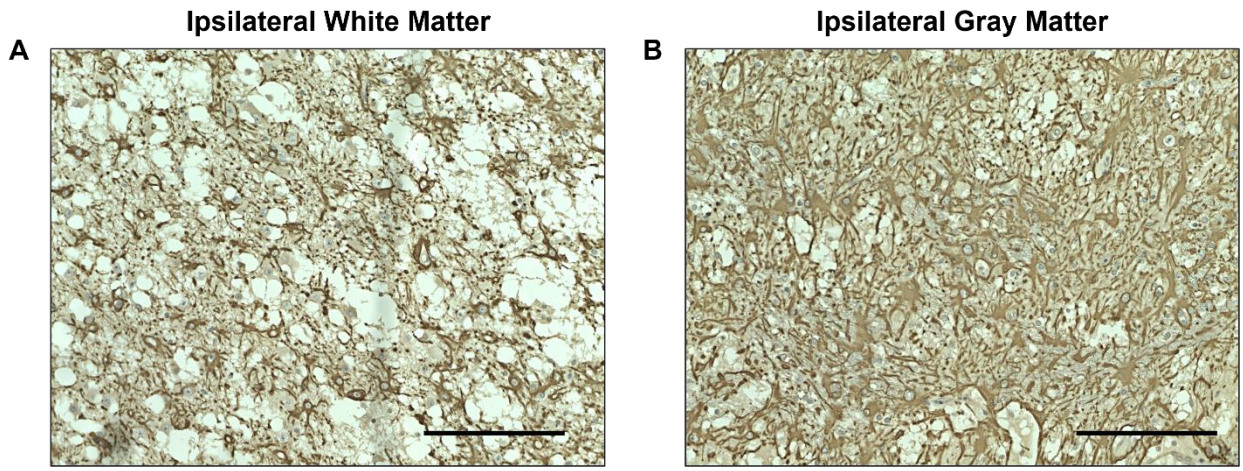

Figure 24. Evidence of glial scarring after a 25 Gy dose prescription within the ipsilateral white matter (left) and gray matter (right). Size of scale bar represents 200 µm.

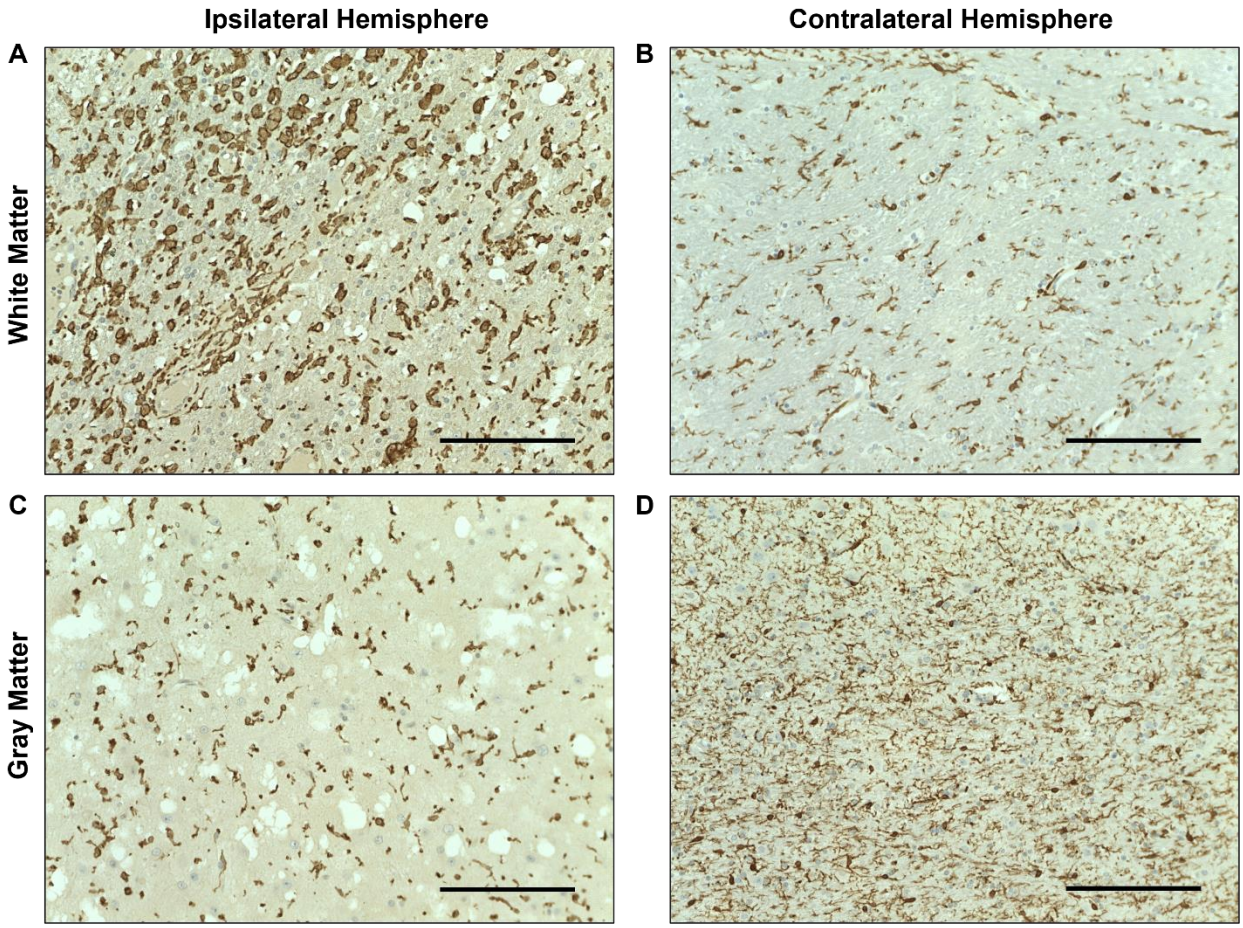

Figure 25. Evidence of microglial activation after a 25 Gy dose prescription within the ipsilateral hemisphere (a and c) with the contralateral hemisphere as comparison (b and d). Size of scale bar represents 200 µm.

4.4 Discussion

This is the first study, to our knowledge, which identifies imaging and histology changes within a preliminary preclinical model of RIBI using mini-pigs. DTI analysis reveals subject-dependent changes in FA and ADC measurements. In addition, our MRS analysis has shown that cranial irradiation induces numerous metabolic imbalances. Lastly, IHC staining is suggestive of dose-dependent neuronal loss and a diffuse astrocyte response to cranial irradiation. Together, these preliminary diffusion, metabolic, and histological characteristics provide further insight into the dynamic profile of late-delayed RIBI within a mini-pig model.

In vivo diffusion measurements show that two subjects experienced clinically relevant late effects after receiving either a 25 Gy (P1) or 15 Gy (P3) prescription dose. Specifically, a decrease in FA values and an increase in ADC values were measured in the irradiated hemisphere of both mini-pigs by the last imaging time point. Interestingly, diffusion measurements are much more variable for the contralateral hemisphere. For P1, FA increases in the IC but decreases in the CC while ADC increases in both the IC and CC. For P3, FA increases in the CC while ADC decreases in the IC. Aside from the increase in contralateral ADC values, these results suggest that the ipsilateral hemisphere is injured after cranial irradiation [6] while the contralateral hemisphere is not affected by radiation, but rather undergoes aging-related myelination as seen in early developmental studies of mini-pigs and humans [18,19].

In vivo metabolite measurements show that all subjects experienced clinically relevant late effects after receiving either a 25 Gy (P1 and P2) or 15 Gy (P3 and P4) prescription dose. A late or overall decrease in NAA, which has been reported in patients that have underwent cranial radiation therapy [11–14,20], were observed in three mini-pigs (P1, P2, and P4) up to the latest imaging time point. Changes in tCho, which also have been reported in cranially irradiated patients [11,14,20], were observed in all four mini-pigs (P1, P2, P3, and P4) up to the latest imaging time point. A late increase in mI, which has been reported in one patient study [14], was observed in one mini-pig (P4) up to the latest imaging time point. A late decrease in tCr, which has been reported in two studies of human patients [11,13], was also observed in two mini-pigs (P1 and P4) up to the latest imaging time point. Similar metabolite trends between the ipsilateral and contralateral hemispheres may be due to biological processes crossing over from the ipsilateral hemisphere. Further studies with larger sample sizes and sham controls will need to be conducted to confirm this hypothesis.

Interestingly, an increase in Glx was observed in all four mini-pigs (P1, P2, P3, and P4). Unfortunately, there is currently no data is reported regarding *in vivo* measurements of Glx in humans except for one study [12] that states there is no change in Glx/tCr post-irradiation. However, it is important to consider that potential changes (or a lack thereof) in tCr levels are not described within this study. If tCr were reported to be variable, the findings regarding Glx may be considerably different. On the other hand, Glx/Cr measurements in irradiated rodent brains have been reported to increase [21], decrease [22,23], or have no change post-irradiation [24,25]. Through the analysis of gene expression profiles, one non-human primate study has shown that regions of white matte injury exhibit impairment in glutamatergic neurotransmission [26]. One study of normal, unirradiated mini-pigs use MRS to show that Glx decreases with age [27]. Based on these data, there is thus an understanding that a post-irradiation increase of Glx departs from the normal metabolite profile observed in mini-pigs and may correspond with radiation-induced genetic changes previously observed in non-human primates. Additionally, there was a decrease in mI was observed in three mini-pigs (P1, P2, and P3). Unfortunately, radiation-induced decreases in mI have been unreported in studies of patients that have underwent cranial radiation therapy. In consideration with our histology data, there is a decrease in ipsilateral astrocytic cell density when compared to the contralateral hemisphere for both P1 and P3. While our results do reflect the underlying histology, the reasoning that underlies this post-irradiation mI decrease remains unclear.

Our histological observations of the P1 shows that lower numbers of $NeuN^+$ cells and higher numbers of DCX^+ cells present in the ipsilateral hemisphere compared to the contralateral side at 4 months post-irradiation. This indication of mature neuronal cell loss and immature neuronal cell gain was not observed in P3, which further supports the conclusion of the previous chapter that the 15 Gy dose prescription was not able to induce an experimentally adequate replication of RIBI. Additionally, density of $GFAP^+$ cells was decreased in the ipsilateral hemisphere with respect to the contralateral side for both pigs that received either the 25 Gy or 15 Gy dose. These and previous histological findings are similar to human results, which report cases of demyelination, gliosis, and white matter necrosis [28,29].

Taken together, these imaging and histological findings illustrate dynamic radiation-induced metabolic, diffusion, and histological changes that occur months after cranial irradiation. Reviews regarding neurological applications of DTI protocols suggest the loss of myelination corresponds with a decrease in FA values while the appearance of cerebral edema is associated

with an increase in ADC values [19,30]. Additionally, reviews regarding neurological applications of MRS techniques support the use of NAA as a reliable marker of neuronal density or function, tCho as a marker for membrane synthesis and degradation, Glx as a marker for excitatory neurotransmission and protein biosynthesis, mI as a marker for glial cell density, and tCr as a marker for energy buffering or shuttling [10,31,32]. By holistically evaluating post-irradiation changes within each mini-pig, it is observed that P1 experienced demyelination with an increase in edema to maintain normal intracranial pressure. Associated with these microstructural changes are late neuronal injury, decreased membrane turnover, increased excitatory neurotransmission, loss of glial cell density, and alterations in energy metabolism up. To validate these findings, histology confirms a decrease in post-mitotic neurons, neuronal precursor cells, and astrocyte area within the irradiated hemisphere. P2 presented both a lack of demyelination and edema presence. Additional metabolic changes include general neuronal injury, increased membrane turnover, increased excitatory neurotransmission, loss of glial cell density, and increased energy metabolism. P3 experienced demyelination with varying changes in edema dependent upon the white matter tract. Associated with these microstructural changes are a lack of general neuronal injury, increased membrane turnover, increased excitatory neurotransmission, loss of glial cell density, and early alterations in energy metabolism. Interestingly, histology indicates a lack of change in post-mitotic neurons and neuronal precursor cells, while astrocyte area decreased within the irradiated hemisphere. Finally, P4 presented an overall lack of demyelination and edema presence. Additional metabolic changes include late neuronal injury, a late decrease in membrane turnover, increased excitatory neurotransmission, a late gain of glial cell density, and alterations in energy metabolism. Comparing our results to the results from DTI and MRS studies of normal, unirradiated mini-pigs, we see that our results are a departure from the clinical expectation and the species' norm [18,27]. The biological significance of our results remains unclear since this is the first study, to our knowledge, that reports late-delayed effects of RIBI in a mini-pig model. As such, additional mini-pig studies using comprehensive biological and genetic assays along with these imaging techniques will greatly enhance the current understanding of RIBI development in intermediate pre-clinical animal models.

One limitation of this study would be its lack of sham control to isolate age-dependent effects. Future studies should incorporate larger sample sizes with sham controls in order to confirm the current data regarding age-dependent effects of the mini-pig brain. Additionally, sham

controls would rule out the need for half-hemispheric radiation plans, allowing us to explore other radiation treatment options such as whole brain radiotherapy. Another limitation is the lack of tissue delineation within the voxel from our spectroscopic findings. While this can ideally be performed using segmented tissue probability maps of normal mini-pig brains, severe edema and intracranial pressure experienced by the 25 Gy cohort has created difficulties in image registration. Therefore, future developments in image segmentation may allow for a more detailed analysis of the origin of our metabolite signals.

4.5 Conclusion

In summary, the current study describes the use of DTI, MRS, and IHC to characterize late-delayed changes within the mini-pig brain after either 25 Gy or 15 Gy irradiation. FA and ADC maps of the DTI data indicate that microstructural damage within major WM tracts was induced in both dose cohorts. Surprisingly, MRS results demonstrate abnormal metabolite changes in Glx for both dose cohorts and in tCr for only the 25 Gy cohort. Finally, histology shows that a 25 Gy dose was able to induce changes in both neuronal subpopulations and astrocytes while a 15 Gy dose was only capable of inducing changes in astrocytes. While this sample of four mini-pigs is not fully representative of a complete preclinical model of late-delayed RIBI, this preliminary study has established a clinically relevant model of RIBI which additional studies can build upon. Understanding the long-term effects of radiation on normal-appearing brain parenchyma is an important step in ultimately creating a reliable preclinical model of RIBI with replicable endpoints.

4.6 Acknowledgements

The author(s) acknowledge the assistance of MacKenzie McIntosh and the Purdue University Histology Research Laboratory, a core facility of the NIH-funded Indiana Clinical and Translational Science Institute. This publication was made possible, in part, with support from the Indiana Clinical and Translational Sciences Institute funded, in part by Grant Number UL1TR002529 from the National Institutes of Health, National Center for Advancing Translational Sciences, Clinical and Translational Sciences Award. Also, the Purdue Life Science MRI facility is supported by grant S10OD012336 from the National Institutes of Health.

4.7 References

1. Greene-Schloesser D, Robbins ME, Peiffer AM, Shaw EG, Wheeler KT, Chan MD. Radiation-induced brain injury: A review. Front Oncol [Internet]. 2012 [cited 2022 Mar 11];2. Available from: http://journal.frontiersin.org/article/10.3389/fonc.2012.00073/abstract

2. Tofilon PJ, Fike JR. The Radioresponse of the Central Nervous System: A Dynamic Process. Radiation Research. 2000;153:357–70.

3. Durand T, Bernier M-O, Léger I, Taillia H, Noël G, Psimaras D, et al. Cognitive outcome after radiotherapy in brain tumor. Current Opinion in Oncology. 2015;27:510–5.

4. Turnquist C, Harris BT, Harris CC. Radiation-induced brain injury: current concepts and therapeutic strategies targeting neuroinflammation. Neuro-Oncology Advances. 2020;2:vdaa057.

5. Alexander AL, Lee JE, Lazar M, Field AS. Diffusion tensor imaging of the brain. DIFFUSION TENSOR IMAGING. 2007;4:14.

6. Makola M, Douglas Ris M, Mahone EM, Yeates KO, Cecil KM. Long-term effects of radiation therapy on white matter of the corpus callosum: a diffusion tensor imaging study in children. Pediatr Radiol. 2017;47:1809–16.

7. Khong P-L, Leung LHT, Fung ASM, Fong DYT, Qiu D, Kwong DLW, et al. White Matter Anisotropy in Post-Treatment Childhood Cancer Survivors: Preliminary Evidence of Association With Neurocognitive Function. JCO. 2006;24:884–90.

8. King TZ, Wang L, Mao H. Disruption of White Matter Integrity in Adult Survivors of Childhood Brain Tumors: Correlates with Long-Term Intellectual Outcomes. Frasch MG, editor. PLoS ONE. 2015;10:e0131744.

9. Ravn S, Holmberg M, Sørensen P, Frøkjær JB, Carl J. Differences in supratentorial white matter diffusion after radiotherapy – new biomarker of normal brain tissue damage? Acta Oncologica. 2013;52:1314–9.

10. van der Graaf M. In vivo magnetic resonance spectroscopy: basic methodology and clinical applications. Eur Biophys J. 2010;39:527–40.

11. Virta A, Patronas N, Raman R, Dwyer A, Barnett A, Bonavita S, et al. Spectroscopic imaging of radiation-induced effects in the white matter of glioma patients. Magnetic Resonance Imaging. 2000;18:851–7.

12. Follin C, Erfurth EM, Johansson A, Lätt J, Sundgren PC, Österberg K, et al. Impaired brain metabolism and neurocognitive function in childhood leukemia survivors despite complete hormone supplementation in adulthood. Psychoneuroendocrinology. 2016;73:157–65.

13. Rueckriegel SM, Driever PH, Bruhn H. Supratentorial Neurometabolic Alterations in Pediatric Survivors of Posterior Fossa Tumors. International Journal of Radiation Oncology*Biology*Physics. 2012;82:1135–41.

14. Rutkowski T, Tarnawski R, Sokol M, Maciejewski B. 1h-mr spectroscopy of normal brain tissue before and after postoperative radiotherapy because of primary brain tumors. International Journal of Radiation Oncology*Biology*Physics. 2003;56:1381–9.

15. Miot E, Hoffschir D, Alapetite C, Gaboriaud G, Pontvert D, Fetissof F, et al. Experimental MR Study of Cerebral Radiation Injury: Quantitative T2 Changes over Time and Histopathologic Correlation. 1995;12.

16. Miot-Noirault E, Akoka S, Hoffschir D, Pontvert D, Gaboriaud G, Alapetite C, et al. Potential of T2 Relaxation Time Measurements for Early Detection of Radiation Injury to the Brain: Experimental Study in Pigs. 1996;6.

17. Yushkevich PA, Piven J, Hazlett HC, Smith RG, Ho S, Gee JC, et al. User-guided 3D active contour segmentation of anatomical structures: Significantly improved efficiency and reliability. NeuroImage. 2006;31:1116–28.

18. Ryan MC, Sherman P, Rowland LM, Wijtenburg SA, Acheson A, Fieremans E, et al. Miniature pig model of human adolescent brain white matter development. Journal of Neuroscience Methods. 2018;296:99–108.

19. Rollins NK. Using ADC to Study the Brain in Early Childhood: Not for the Uninitiated. Radiology. 2021;298:425–6.

20. Sundgren PC. MR Spectroscopy in Radiation Injury. AJNR Am J Neuroradiol. 2009;30:1469–76.

21. Atwood T, Payne VS, Zhao W, Brown WR, Wheeler KT, Zhu J-M, et al. Quantitative Magnetic Resonance Spectroscopy Reveals a Potential Relationship between Radiation-Induced Changes in Rat Brain Metabolites and Cognitive Impairment. Radiation Research. 2007;168:574–81.

22. Brown RJ, Jun BJ, Cushman JD, Nguyen C, Beighley AH, Blanchard J, et al. Changes in Imaging and Cognition in Juvenile Rats After Whole-Brain Irradiation. International Journal of Radiation Oncology*Biology*Physics. 2016;96:470–8.

23. Bálentová S, Hnilicová P, Kalenská D, Baranovičová E, Muríň P, Hajtmanová E, et al. Effect of fractionated whole-brain irradiation on brain and plasma in a rat model: Metabolic, volumetric and histopathological changes. Neurochemistry International. 2021;145:104985.

24. Robbins ME, Payne V, Tommasi E, Diz DI, Hsu F-C, Brown WR, et al. The AT1 Receptor Antagonist, L-158,809, Prevents or Ameliorates Fractionated Whole-Brain Irradiation–Induced Cognitive Impairment. International Journal of Radiation Oncology*Biology*Physics. 2009;73:499–505.

25. Bálentová S, Hnilicová P, Kalenská D, Murín P, Hajtmanová E, Lehotský J, et al. Effect of whole-brain irradiation on the specific brain regions in a rat model: Metabolic and histopathological changes. NeuroToxicology. 2017;60:70–81.

26. Andrews RN, Dugan GO, Peiffer AM, Hawkins GA, Hanbury DB, Bourland JD, et al. White Matter is the Predilection Site of Late-Delayed Radiation-Induced Brain Injury in Non-Human Primates. Radiation Research. 2019;191:217.

27. Ryan MC, Kochunov P, Sherman PM, Rowland LM, Wijtenburg SA, Acheson A, et al. Miniature pig magnetic resonance spectroscopy model of normal adolescent brain development. Journal of Neuroscience Methods. 2018;308:173–82.

28. Lai R, Abrey LE, Rosenblum MK, DeAngelis LM. Treatment-induced leukoencephalopathy in primary CNS lymphoma: A clinical and autopsy study. Neurology. 2004;62:451–6.

29. Oi S, Kokunai T, Ijichi A. Radiation-induced Brain Damage in Children. Neurologia medico-chirurgica. 1990;30:36–42.

30. Tae W-S, Ham B-J, Pyun S-B, Kang S-H, Kim B-J. Current Clinical Applications of Diffusion-Tensor Imaging in Neurological Disorders. J Clin Neurol. 2018;14:129.

31. Quarantelli M. MRI/MRS in neuroinflammation: methodology and applications. Clin Transl Imaging. 2015;3:475–89.

32. Bertholdo D, Watcharakorn A, Castillo M. Brain Proton Magnetic Resonance Spectroscopy. Neuroimaging Clinics of North America. 2013;23:359–80.

CHAPTER 5. CONCLUSIONS

5.1 Summary of Research

The objective of Aim 1 was to determine the accuracy of current rodent models of late-delayed radiation-induced brain injury with respect to the data derived from human patients at least 6 months post-treatment. To achieve this, a thorough search was conducted on PubMed, Web of Science, and Scopus to identify studies that performed cognitive assessments and magnetic resonance imaging techniques on either humans or rodents after cranial radiation therapy. A qualitative synthesis of the data was henceforth reported on 153 relevant studies. In summary, cognitive deficits in humans were found to manifest across multiple domains after brain irradiation. Additionally, radiological evidence in humans highlight various neuroimaging-detectable changes post-irradiation. It was unclear, however, whether these findings reflected ground truth or research interests. Rodent models did not comprehensively reproduce characteristics of cognitive and radiological injury as currently identified in humans.

The objective of Aim 2 was to establish a mini-pig model of late-delayed radiation-induced brain injury based on the current clinical standard of diagnosis. To achieve this, a hemispheric mini-pig model of RIBI was generated with a clinical 6 MV photon irradiator and evaluated with a clinical 3T MRI. Two pairs of Yucatan mini-pigs each received either 15 Gy or 25 Gy to the left brain hemisphere. For the mini-pigs that received 25 Gy, MRI revealed diffuse white matter pathology consistent with the human disease that progressed to outright radiation necrosis and severe brain swelling. Histology was consistent with the final MRI evaluation. The pigs that received a 15 Gy dose appeared normal all the way to 6 months post-irradiation with no obvious lesions on MRI or histopathology.

The objective of Aim 3 was to examine characteristic changes in diffusion properties, metabolite concentrations, and histological appearances within our mini-pig model late-delayed radiation-induced brain injury. To achieve this, diffusion tensor imaging (DTI), magnetic resonance spectroscopy (MRS), and immunohistochemical (IHC) staining were performed in addition to the imaging and histological methods previously described in Aim 2. FA and ADC maps generated from DTI data revealed microstructural damage within major WM tracts for both the 25 Gy cohort at 3 months and 4 months post-irradiation and the 15 Gy dose cohort at 6 months

post-irradiation. MRS results demonstrated post-irradiation changes in metabolites such as NAA, tCho, Glx, mI, and tCr for both the 25 Gy dose cohort at 3 months and 4 months post-irradiation and the 15 Gy dose cohort at 6 months post-irradiation. Finally, IHC stains presented changes in both neuronal subpopulations and astrocytes after a 25 Gy dose at 4 months post-irradiation and a change in only astrocytes after a 15 Gy dose at 6 months post-irradiation.

5.2 Impact

As set forth in Aim 1, the work detailed in Chapter 2 represents the first systematic review to comprehensively address the long-term radiological and cognitive differences between rodent and human brains after cranial irradiation. The intention of such work was to formalize the current cognitive and radiological assessments used to evaluate RIBI, to describe the relationships between and within cognitive and radiological findings of RIBI in humans, and to ultimately deduce whether current rodent models of RIBI can replicate the cognitive and radiological evidence reported in humans. The implication of the resulting findings suggests there are currently many inconsistencies in measuring cognitive and radiological signs of RIBI, which lead to incongruencies in rodent modeling of RIBI. Furthermore, our review provides alternative considerations for future studies of RIBI, such as incorporating primate-equivalent cognitive assessments for rodent models that are currently used outside the field of RIBI, standardizing neurocognitive tests for patients that have undergone radiotherapy, and implementing more advanced MRI techniques in human studies of RIBI.

As set forth in Aims 2 and 3, the work detailed in Chapters 3 and 4 represent the first mini-pig model developed that uses current clinical approaches for radiation dose planning and delivery as well as advanced research approaches for post-treatment follow-up. Specifically, this current mini-pig model uses IMRT for radiation dose planning, a 6 MV linear accelerator for radiation delivery, anatomical MRI to confirm the presence of RIBI according to the current clinical standard of diagnosis, DTI for follow-up regarding diffusion-related changes, MRS for follow-up regarding metabolite changes, and immunohistochemical staining to validate imaging findings. In contrast, previous research used electron beam radiotherapy, anatomical MRI, and general histological methods to develop their mini-pig model of RIBI [1,2]. The intention of such work was to replicate clinically relevant, MRI-detectable white matter injuries that have previously been shown to be undetectable in rodent models of RIBI [3–5]. Continued development and use of our

mini-pig model could provide greater insight into the mechanism of late-delayed RIBI. It is our hope that such findings may provide a foundation for translational work into early diagnosis and treatment of RIBI in order to ultimately improve the quality of life for pediatric cancer survivors.

5.3 Limitations

One limitation, concerning Chapter 3 and 4, is the small sample size used to develop and characterize our preliminary mini-pig model of RIBI. A total sample of 4 mini-pigs, divided into two equal cohorts, has made it difficult to produce consistent results due to inherent differences in the response of individual animals to cranial irradiation. However, these preliminary studies have laid the groundwork for future studies to improve upon. Additional studies with sham controls and larger cohorts, with varying increments of prescribed doses between 15 Gy and 25 Gy, are necessary to confirm our present findings and to elucidate previously missed patterns.

Another limitation, regarding Chapter 3 and 4, is the lack of tumor pathology in our preliminary preclinical model of RIBI. Normal tissue injuries in patient brains may be different due to the tumor microenvironment and multimodality treatments (i.e., surgery, radiotherapy, and chemotherapy). Although our current model is free from these clinical complexities, the ideal situation would be to individually introduce these factors in future studies to more fully replicate the clinical scenario. However, there will always be unique complicating factors inherent to humans, such as pre-existing health complications and lifestyle factors, that will most likely render the creation of a “perfect” preclinical model an impossible task.

5.4 Future Directions

Additional advanced magnetic resonance imaging techniques could be incorporated into future studies to collect more detailed and specific data regarding post-irradiation changes within brain tissue. One of such imaging methods include neurite orientation dispersion and density imaging (NODDI) [6], which has yet to be implemented in a RIBI study. In short, NODDI would provide researchers and clinicians additional information regarding the microstructural architecture of axons and dendrites. Another imaging method is magnetic resonance spectroscopic imaging (MRSI) [7], which has currently only been described in one RIBI study [8]. In short, MRSI would allow researchers and clinicians to visualize the spatial distribution of metabolites

throughout the brain as opposed to only a small, single volume. Once a future iteration this mini-pig model is capable of consistently replicating more accurate human-like manifestations of RIBI, the use of NODDI and MRSI would be incredibly informative in further describing the pathophysiology of RIBI.

Exploring the genetic effects of RIBI pathophysiology within our mini-pig model would be another interesting direction to pursue. Through a comprehensive analysis of genome-wide expression profiles derived from a rodent model of RIBI, it has shown that irradiated microglia share similar patterns of transcriptional changes that occur in aged microglia [9]. This finding suggests that cranial irradiation may artificially induce the brain to take on an aged phenotype. As a hypothesis, this mechanism could explain the clinical and radiological manifestations of microvascular injuries, demyelination, and cognitive deficits, which can all be found in a normal, aging population. The incorporation of such genetic techniques in future mini-pig models, correlated with NODDI and MRSI, can help form a much-needed holistic understanding of RIBI pathophysiology.

5.5 References

1. Miot E, Hoffschir D, Alapetite C, Gaboriaud G, Pontvert D, Fetissof F, et al. Experimental MR Study of Cerebral Radiation Injury: Quantitative T2 Changes over Time and Histopathologic Correlation. 1995;12.

2. Miot-Noirault E, Akoka S, Hoffschir D, Pontvert D, Gaboriaud G, Alapetite C, et al. Potential of T2 Relaxation Time Measurements for Early Detection of Radiation Injury to the Brain: Experimental Study in Pigs. 1996;6.

3. Atwood T, Payne VS, Zhao W, Brown WR, Wheeler KT, Zhu J-M, et al. Quantitative Magnetic Resonance Spectroscopy Reveals a Potential Relationship between Radiation-Induced Changes in Rat Brain Metabolites and Cognitive Impairment. Radiation Research. 2007;168:574–81.

4. Shi L, Linville MC, Iversen E, Molina DP, Yester J, Wheeler KT, et al. Maintenance of white matter integrity in a rat model of radiation-induced cognitive impairment. Journal of the Neurological Sciences. 2009;285:178–84.

5. Rancilio NJ, Dahl S, Athanasiadi I, Perez-Torres CJ. Design, construction, and in vivo feasibility of a positioning device for irradiation of mice brains using a clinical linear accelerator and intensity modulated radiation therapy. International Journal of Radiation Biology. 2017;93:1321–6.

6. Zhang H, Schneider T, Wheeler-Kingshott CA, Alexander DC. NODDI: Practical in vivo neurite orientation dispersion and density imaging of the human brain. NeuroImage. 2012;61:1000–16.

7. Posse S, Otazo R, Dager SR, Alger J. MR spectroscopic imaging: Principles and recent advances. J Magn Reson Imaging. 2013;37:1301–25.

8. Virta A, Patronas N, Raman R, Dwyer A, Barnett A, Bonavita S, et al. Spectroscopic imaging of radiation-induced effects in the white matter of glioma patients. Magnetic Resonance Imaging. 2000;18:851–7.

9. Li MD, Burns TC, Kumar S, Morgan AA, Sloan SA, Palmer TD. Aging-like changes in the transcriptome of irradiated microglia: Transcriptome of Irradiated Microglia. Glia. 2015;63:754–67.

APPENDIX A. SUPPORTING INFORMATION FOR CHAPTER 2

PubMed Search String

(human OR (rat OR mouse OR mice OR rodent)) AND (brain OR cranial) AND ("radiation-induced") AND ((neuroimag* OR magnetic AND resonance) OR (behavior OR cogniti*))

Baseline Characteristics of Included Human (Table A.1) and Rodent (Table A.2) Studies

Table A.1. Baseline characteristics of included human studies.

Author	Age Demographic	# CRT Patients	% Male	Tumor Type	Irradiated Volume	Total RT Dose [Gy]	Dose/ Fraction [Gy]	Cog. RIBI	Rad. RIBI	RIBI Mea-sure-ment
Agbahiwe (2017)	Pediatric	10	50	Primary brain tumor	Whole brain (n=8), local field (n=2)	23.4-36, 54-59.4	N/A	None	None	6 months
Alirezaei (2021)	Adult	10	50	Primary brain tumor	Local field	54	1.8	X	X	6 months
Andersen (2003)	Pediatric	9	55.5	Primary brain tumor	Whole brain (n=4), local field (n=5)	25-56, 31-54	1.7-1.8, 1.7-2		X	192 months
Anderson (1997)	Pediatric	100	45	Acute lymphoblastic leukemia	Whole brain	18-24	N/A	X		60 months
Aoyama (2007)	Adult	132	74.5	Brain metastasis	Whole brain (n=65), local field (n=67)	30, 18-25	3, 18-25	X		15.8 months
Armstrong (2002)	Adult	26	58	Primary brain tumor	Local field	54-63	1.8-2	X	X	30 months

Table A.1 continued

Author	Age Demographic	# CRT Patients	% Male	Tumor Type	Irradiated Volume	Total RT Dose [Gy]	Dose/ Fraction [Gy]	Cog. RIBI	Rad. RIBI	RIBI Mea-sure-ment
Armstrong (2016)	Pediatric	35	60	Primary brain tumor	Whole brain (n=19), local field (n=16)	52-56	1.8	X		60 months
Belliveau (2017)	N/A	10	20	Primary brain tumor	Local field	N/A	N/A		X	26 months
Bian (2019)	Adult	18	55.5	Primary brain tumor	Local field	54-60	1.8-2	None	X	6 months
Bojaxhiu (2017)	Pediatric	171	59	Primary brain tumor	Local field	40-74.1	1.5-2		X	14.5 months
Bompaire (2018)	Adult	40	37.5	Primary brain tumor or brain metastasis	Whole brain (n=14), local field (n=26)	30-60	1.5-3	X	X	36 months
Brown (2020)	Adult	257	42	Brain metastasis	Whole brain	30	3	X		7.9 months

Table A.1 continued

Author	Age Demographic	# CRT Patients	% Male	Tumor Type	Irradiated Volume	Total RT Dose [Gy]	Dose/ Fraction [Gy]	Cog. RIBI	Rad. RIBI	RIBI Mea-sure-ment
Buizza (2021)	Adult	46	37	Primary brain tumor	Local field	50.4-66.0	N/A		X	6 months
Butler (2013)	Pediatric	444	56.5	Primary brain tumor or acute lymphoblastic leukemia	N/A	N/A	N/A	X		12 months
Chang (2009)	Adult	58	50	Brain metastasis	Whole brain (n=28), local field (n=30)	30, 15-20	2.5, 15-20	X		9.5 months
Chapman (2012)	Adult	10	90	Primary brain tumor	Local field	50.4-59.4	1.8	X	X	7 months
Chapman (2016)	Adult	27	56	Primary brain tumor	Local field	50.4-70	2	X	X	6 months
Connor (2016)	Adult	15	60	Primary brain tumor	Local field	60	2		X	6 months
Connor (2017)	Adult	49	N/A	Primary brain tumor	Local field	60	2		X	12 months

Table A.1 continued

Author	Age Demographic	# CRT Patients	% Male	Tumor Type	Irradiated Volume	Total RT Dose [Gy]	Dose/ Fraction [Gy]	Cog. RIBI	Rad. RIBI	RIBI Mea-sure-ment
Corn (2008)	Pediatric	156	N/A	Brain metastasis	Whole brain	37.5	2.5	X		6 months
Correa (2012)	Adult	24	70	Primary brain tumor	Whole brain	36-59.4	N/A	X	X	42.5 months
Davidson (2000)	Pediatric	14	N/A	Primary brain tumor or acute lymphoblastic leukemia	N/A	N/A	N/A	X	X	93 months
Dietrich (2001)	Pediatric	28	55	Primary brain tumor	Whole brain (n=21), local field (n=7)	24-45, 35-57	N/A		X	45.6 months
Douw (2009)	Adult	32	56	Primary brain tumor	Local field	30-69	1.6-2.5	X	X	144 months
Duan (2016)	Adult	37	78.4	Nasopharyngeal carcinoma	Local field	66-74	1.8-2		X	6 months
Edelmann (2014)	Pediatric	39	46	Acute lymphoblastic leukemia	Whole brain	15-25	N/A	X	X	287 months

Table A.1 continued

Author	Age Demographic	# CRT Patients	% Male	Tumor Type	Irradiated Volume	Total RT Dose [Gy]	Dose/ Fraction [Gy]	Cog. RIBI	Rad. RIBI	RIBI Mea-sure-ment
Faraci (2011)	Pediatric	24	44	Acute lymphoblastic leukemia	Whole brain	18-24	N/A		X	132 months
Follin (2016)	Pediatric	38	45	Acute lymphoblastic leukemia	Whole brain	18-30	N/A	X	X	408 months
Follin (2019)	Pediatric	38	45	Acute lymphoblastic leukemia	Whole brain	18-30	N/A		X	408 months
Greenberger (2014)	Pediatric	32	53.1	Primary brain tumor	Local field	48.6-54	1.8	None		91 months
Haris (2008)	Adult	5	60	Primary brain tumor	Local field	54	1.8		X	8 months
Hope (2015)	Adult	18	77.7	Primary brain tumor	Local field	30	2		X	6 months
Hua (2012)	Pediatric	20	60	Primary brain tumor	Local field	54-59.4	1.8		X	42 months
Johannesen (2003)	Pediatric and Adult	33	45	Primary brain tumor	Affected hemisphere	45-59	1.8		X	157 months
Karunamuni (2015)	Adult	15	66.7	Primary brain tumor	Local field	60	2		X	12 months

Table A.1 continued

Author	Age Demographic	# CRT Patients	% Male	Tumor Type	Irradiated Volume	Total RT Dose [Gy]	Dose/ Fraction [Gy]	Cog. RIBI	Rad. RIBI	RIBI Mea-sure-ment
Khong (2006)	Pediatric	21	71.4	Primary brain tumor or acute lymphoblastic leukemia	Whole brain	23.4-40, 12-24	1.8-2	X	X	39 months
King (2015)	Pediatric	14	50	Primary brain tumor	N/A	50.4-59.4	N/A	X	X	164 months
Kralik (2018)	Pediatric	76	63	Primary brain tumor	Local field	30-59.4	N/A		X	8 months
Krull (2013)	Pediatric	353	48.7	Acute lymphoblastic leukemia	Whole brain	18-24	N/A	X		312 months
Lee (2004)	Adult	10	50	Primary brain tumor	Local field	53.1-66.9	1.8-2		None	N/A
Leng (2017)	Adult	70	76	Nasopharyngeal carcinoma	Local field	66-74	1.8-2		X	6 months
Lin (2017)	Adult	20	75	Nasopharyngeal carcinoma	Local field	66-76	2		X	11 months
Lin (2021)	Adult	120	62.5	Primary brain tumor	Local field	68-70	2.1-2.2	X	X	6 months
Lupo (2011)	Adult	19	N/A	Primary brain tumor	Local field	N/A	N/A		X	56.4 months
Lupo (2016)	Adult	16	N/A	Primary brain tumor	Local field	N/A	N/A		X	8 months
Lv (2014)	Adult	30	66.6	Nasopharyngeal carcinoma	Local field	58-76	2		None	7.6 months

Table A.1 continued

Author	Age Demographic	# CRT Patients	% Male	Tumor Type	Irradiated Volume	Total RT Dose [Gy]	Dose/ Fraction [Gy]	Cog. RIBI	Rad. RIBI	RIBI Mea-sure-ment
MacLean (1995)	Pediatric	37	67.5	Acute lymphoblastic leukemia	Whole brain	18	1.8	X		9.6 months
Makola (2017)	Pediatric	14	85.7	Primary brain tumor	Whole brain (n=10), local field (n=4)	48-57	N/A		X	24 months
Matsumoto (1995)	Pediatric	38	50	Acute lymphoblastic leukemia	Whole brain	18-24	2		X	18 months
Merchant (2014)	Pediatric	58	68.9	Primary brain tumor	Whole brain	23.4-39.6	N/A	X		60 months
Miura (2017)	Adult	12	66.6	Primary brain tumor	Whole brain (n=9), local field (n=3)	45-78	N/A		X	237.6 months
Monaco (2013)	Adult	68	50	Brain metastasis (non-small cell lung cancer)	Whole brain (n=37), local field (n=31)	30	3		X	12.8 months

Table A.1 continued

Author	Age Demographic	# CRT Patients	% Male	Tumor Type	Irradiated Volume	Total RT Dose [Gy]	Dose/ Fraction [Gy]	Cog. RIBI	Rad. RIBI	RIBI Mea-sure-ment
Moretti (2005)	Adult	34	N/A	Primary brain tumor	N/A	20-65	N/A	X		12 months
Morrison (2019)	Adult	91	70	Primary brain tumor	Local field	N/A	N/A		X	60 months
Morrison (2021)	Pediatric	19	57.9	Primary brain tumor	Whole brain (n=12), local field (n=7)	18-59.4	N/A	X	X	12 months
Mulhern (1992)	Pediatric	19	57	Acute lymphoblastic leukemia	Whole brain	18-24	N/A	X		55 months
Mulhern (2001)	Pediatric	42	61	Primary brain tumor	Local field	49-54	N/A	X	X	48 months
Mulhern (2004)	Pediatric	37	54	Primary brain tumor	Whole brain (n=24), local field (n=13)	23.4-59.4	1.8	X	X	68 months
Nagesh (2008)	Adult	25	68	Primary brain tumor	Local field	50-81	1.8-2.7		X	10 months

Table A.1 continued

Author	Age Demographic	# CRT Patients	% Male	Tumor Type	Irradiated Volume	Total RT Dose [Gy]	Dose/ Fraction [Gy]	Cog. RIBI	Rad. RIBI	RIBI Mea-sure-ment
Nagtegaal (2021)	Adult	31	61.3	Primary brain tumor	Local field	50.4-60	1.8-2		X	12 months
Neu (2018)	Pediatric	40	45	Primary brain tumor	Whole brain (n=33), local field (n=7)	54.3-54.9	N/A		X	162 months
Omuro (2005)	Adult	129	56	Primary central nervous system lymphoma	Whole brain	3.6-59.4	N/A	X	X	43 months
Passos (2015)	Pediatric	33	58	Primary brain tumor	Whole brain (n=22), local field (n=11)	17.3-46.7	N/A		X	183 months
Passos (2017)	Pediatric	132	61.4	Primary brain tumor	Whole brain (n=71), local field (n=61)	19.8-53.2	N/A		X	133 months
Peters (2013)	Pediatric	7	N/A	Primary brain tumor	N/A	N/A	N/A		X	21 months
Phillips (2020)	N/A	101	45.5	Acute lymphoblastic leukemia	Whole brain	18-24	N/A		X	324 months

Table A.1 continued

Author	Age Demographic	# CRT Patients	% Male	Tumor Type	Irradiated Volume	Total RT Dose [Gy]	Dose/ Fraction [Gy]	Cog. RIBI	Rad. RIBI	RIBI Mea-sure-ment
Prust (2015)	Adult	14	42.8	Primary brain tumor	Local field	60	2		X	8 months
Radcliffe (1994)	Pediatric	24	75	Primary brain tumor	Whole brain	24-56	N/A	X		12 months
Rashid (2017)	Pediatric	12	N/A	Primary brain tumor	Whole brain	18-59.4	N/A	X	X	6 months
Ravn (2013)	Adult	19	47	Primary brain tumor	N/A	N/A	N/A		X	55 months
Reddick (1998)	Pediatric	56	62.5	Primary brain tumor	Whole brain, local field	25-65	N/A		X	12 months
Reddick (2003)	Pediatric	40	55	Primary brain tumor	Whole brain (n=24), local field (n=16)	23.4-59.4	N/A	X	X	68 months
Reddick (2005)	Pediatric	52	67.3	Primary brain tumor	Whole brain	50.8-59.4	1.8		X	30 months
Reddick (2014)	Pediatric	383	55	Primary brain tumor or acute lymphoblastic leukemia	N/A	N/A	N/A	X	X	N/A

Table A.1 continued

Author	Age Demographic	# CRT Patients	% Male	Tumor Type	Irradiated Volume	Total RT Dose [Gy]	Dose/ Fraction [Gy]	Cog. RIBI	Rad. RIBI	RIBI Mea-sure-ment
Redmond (2018)	Pediatric	20	70	Primary brain tumor	Whole brain (n=2), local field (n=18)	12.0-54	N/A	X	X	6 months
Riggs (2014)	Pediatric	20	65	Primary brain tumor	Whole brain	23.4-59.4	N/A	X	X	61 months
Roddy (2016)	Pediatric	110	54	Primary brain tumor	Whole brain (n=52), local field (n=53)	24-66.7	N/A	X	X	43 months
Roongpiboonsopit (2017)	Pediatric and Adult	27	66.7	Primary brain tumor	Whole brain	54-54.9	1.8		X	49 months
Roth (2020)	Pediatric	70	58.5	Primary brain tumor	Whole brain (n=37), local field (n=33)	45-60	N/A	X		62 months
Rueckriegel (2010)	Pediatric	17	70.5	Primary brain tumor	Whole brain	24-32	N/A		X	40 months
Rueckriegel (2012)	Pediatric	24	N/A	Primary brain tumor	Whole brain	24-32	N/A		X	45 months
Rutkowski (2003)	Adult	43	65	Primary brain tumor	Local field	60	2		X	9 months

Table A.1 continued

Author	Age Demographic	# CRT Patients	% Male	Tumor Type	Irradiated Volume	Total RT Dose [Gy]	Dose/ Fraction [Gy]	Cog. RIBI	Rad. RIBI	RIBI Mea-sure-ment
Schatz (2000)	Pediatric	18	50	Acute lymphoblastic leukemia	Whole brain	18-24	N/A	X		N/A
Schatz (2004)	Pediatric	21	53	Acute lymphoblastic leukemia	N/A	N/A	N/A	X		N/A
Schuitema (2013)	Pediatric	44	52.3	Acute lymphoblastic leukemia	Whole brain	15-25	N/A	X	X	300 months
Schuitema (2015)	Pediatric	50	52	Acute lymphoblastic leukemia	Whole brain	15-25	N/A	X		300 months
Seibert (2017)	Adult	54	69	Primary brain tumor	Local field	50.4-60	1.8-2		X	12 months
Shi (2018)	Adult	40	80	Nasopharyngeal carcinoma	Local field	68.8-70.4	N/A		X	12 months
Simó (2016)	Adult	11	91	Small cell lung cancer	Whole brain	25-36	2-3	X	X	36 months
Stokes (2015)	Adult	65	N/A	Brain metastasis	Whole brain (n=35), local field (n=30)	16-50.4	2		X	13 months
Sundgren (2009)	Adult	11	91	Primary brain tumor	Local field	50.4-59.4	1.8		X	6 months

Table A.1 continued

Author	Age Demographic	# CRT Patients	% Male	Tumor Type	Irradiated Volume	Total RT Dose [Gy]	Dose/ Fraction [Gy]	Cog. RIBI	Rad. RIBI	RIBI Mea-sure-ment
Tang (2012)	Adult	46	76.1	Nasopharyngeal carcinoma	Local field	68-76	2	X		72 months
Tanino (2013)	Pediatric	34	53	Primary brain tumor or brain metastasis	Whole brain (n=22), local field (n=12)	24-60	2		X	29 months
Tibbs (2020)	Adult	44	57	Primary brain tumor	Local field	54-70	1.8-2	X	X	6 months
Trifiletti (2015)	Adult	103	58.2	Brain metastasis	Whole brain (n=31), local field (n=72)	12-45	3		X	14 months
Tringale (2019)	Adult	22	50	Primary brain tumor	Local field	50.4-60	1.8-2	X	X	6 months
Twaddle (1983)	Pediatric	23	N/A	Acute lymphoblastic leukemia	Whole brain	24	2	X		70 months
Usenius (1995)	Adult	8	37.5	Primary brain tumor	N/A	40-60	1.8-4		X	60 months
Varon (2014)	Pediatric and Adult	12	58.3	Primary brain tumor or brain metastasis	Whole brain (n=10), local field (n=2)	45-54	N/A		X	32 months

Table A.1 continued

Author	Age Demographic	# CRT Patients	% Male	Tumor Type	Irradiated Volume	Total RT Dose [Gy]	Dose/ Fraction [Gy]	Cog. RIBI	Rad. RIBI	RIBI Mea-sure-ment
Virta (2000)	Adult	9	44.4	Primary brain tumor	Local field	55-70.4	N/A		X	58 months
Wahl (2017)	Adult	13	N/A	Primary brain tumor	Local field	60	2		X	27 months
Wang (2012)	Pediatric and Adult	48	66.7	Nasopharyngeal carcinoma	Local field	68-75	2.1-2.2		X	6 months
Wang (2016)	Adult	40	55	Nasopharyngeal carcinoma	Local field	66-73	2.2		X	N/A
Xiong (2013)	Adult	55	69	Nasopharyngeal carcinoma	N/A	66-74	1.8-2		X	6 months
Zhong (2015)	Adult	48	45.8	Brain metastasis	Whole brain	30	3		X	6 months
Zhu (2016)	Adult	32	45.5	Primary brain tumor	Local field	50.4-70	N/A		X	N/A

Table A.2. Baseline characteristics of included rodent studies.

Author	Species	Age Demographic	# Subjects	% Male	Irradiated Volume	Total RT Dose [Gy]	Dose/ Fraction [Gy]	Cog. RIBI	Rad. RIBI	RIBI Mea-sure-ment
Acharya (2009)	Rat	Early Adulthood	20	100	Whole brain	10	10	X		4 months
Acharya (2011)	Rat	Early Adulthood	41	100	Whole brain	10	10	X		1 month
Acharya (2013)	Rat	Early Adulthood	26	100	Whole brain	10	10	X		1 month
Acharya (2014)	Rat	Early Adulthood	21	100	Whole brain	10	10	X		1 month
Acharya (2016)	Mouse	Early Adulthood	20	100	Whole brain	9	9	X		1.5 months
Acharya (2016)	Rat	Early Adulthood	20	100	Whole brain	10	10	X		1 month
Alexander (2018)	Mouse	Early Adolescence	20	100	Whole brain	20	10	X		1 month
Allen (2018)	Rat	Early Adulthood	30	N/A	Whole brain	27	9	X		1 month
Atwood (2007)	Rat	Early Adulthood	46	100	Whole brain	45	5	X	X	12 months
Balentova (2017)	Rat	Early Adulthood	14	100	Whole brain	35	5		X	4 months
Balentova (2018)	Rat	Early Adulthood	25	100	Whole brain	20	5	X		4 months
Balentova (2019)	Rat	Early Adulthood	20	100	Whole brain	40	9		X	3.5 months

Table A.2. Baseline characteristics of included rodent studies.

Author	Species	Age Demographic	# Subjects	% Male	Irradiated Volume	Total RT Dose [Gy]	Dose/ Fraction [Gy]	Cog. RIBI	Rad. RIBI	RIBI Mea-sure-ment
Balentova (2021)	Rat	Early Adulthood	10	100	Whole brain	32	8		X	2 months
Baulch (2016)	Rat	Early Adulthood	20	100	Whole brain	10	10	X		1 month
Bazyar (2017)	Mouse	Early Adulthood	16	100	Hippocamp us	10	10	X		8 months
Beera (2018)	Mouse	Early Adolescence	44	N/A	Whole brain (n=9), local field (n=35)	8	8		X	1 month
Belarbi (2013)	Mouse	Early Adulthood	20	100	Whole brain	10	10	X		2 months
Brown (2007)	Rat	Late Adolescence	23	N/A	Whole brain	40	5	X		6 months
Brown (2016)	Rat	Early Adolescence	N/A	100	Whole brain	27	3	X	X	6 months
Caceres (2010)	Rat	Early Adolescence	30	100	Whole brain	5	5	X		1 month
Chen (2017)	Rat	Early Adulthood	12	100	Single Hemisphere	30	30		X	1 month
de Guzman (2015)	Mouse	Early Adolescence	11	N/A	Whole brain	7	7		X	2.5 months
Feng (2016)	Mouse	Early Adulthood	N/A	100	Whole brain	10	3.33	X		1 month
Forbes (2014)	Rat	Adulthood	48	100	Whole brain	40	5	X		3 months

Table A.2. Baseline characteristics of included rodent studies.

Author	Species	Age Demographic	# Subjects	% Male	Irradiated Volume	Total RT Dose [Gy]	Dose/ Fraction [Gy]	Cog. RIBI	Rad. RIBI	RIBI Mea-sure-ment
Greene-Schloesser (2014)	Rat	Early Adulthood	40	100	Whole brain	40	5	X		6 months
He (2021)	Mouse	Early Adulthood	79	100	Whole brain	30	30	X	X	1.8 months
Hnilicova (2019)	Rat	Early Adulthood	14	100	Whole brain	35	5		X	4 months
Jenrow (2013)	Rat	N/A	10	100	Whole brain	10	10	X		6 months
Liu (2015)	Rat	N/A	25	0	Whole brain	20	20		X	N/A
Nageswara Rao (2011)	Mouse	Late Adolescence	11	100	Whole brain	20	4	X		1 month
Parihar (2014)	Rat	Early Adulthood	17	100	Whole brain	10	10	X		1.4 months
Peiffer (2014)	Rat	Late Adolescence	12	100	Whole brain	30	5	X	X	9 months
Pérès (2018)	Mouse	Early Adulthood	15	100	Whole brain	5	5		X	1 month
Raber (2004)	Mouse	Early Adulthood	16	100	Hippocampus	10	10	X		3 months
Robbins (2009)	Rat	Early Adulthood	40	100	Whole brain	40	5	X		6 months
Rodgers (2016)	Rat	Early Adolescence	37	100	Whole brain	20	4-20		X	3 months

Table A.2. Baseline characteristics of included rodent studies.

Author	Species	Age Demographic	# Subjects	% Male	Irradiated Volume	Total RT Dose [Gy]	Dose/ Fraction [Gy]	Cog. RIBI	Rad. RIBI	RIBI Mea-sure-ment
Rola (2004)	Mouse	Early Adolescence	20	100	Whole brain	5	5	X		3 months
Sahnoune (2018)	Rat	Early Adolescence	45	100	Whole brain	20	4	X	X	6 months
Shi (2006)	Rat	Late Adulthood	40	100	Whole brain	45	5	X		12 months
Sun (2016)	Rat	Late Adolescence	219	100	Whole brain	2, 10, 20, 30	2, 10, 20, 30	X		12 months
Tang (2019)	Rat	Late Adolescence	20	100	Whole brain	30	6	X	X	12 months
Wang (2009)	Rat	Early Adulthood	40	0	Single Hemisphere	25, 30	25, 30		X	1 month
Wang (2013)	Rat	Early Adulthood	19	0	Single Hemisphere	27.5	27.5		X	5.5 months
Warrington (2012)	Mouse	Early Adulthood	16	100	Whole brain	36	4.5	X		1 month
Yoneoka (1999)	Rat	Early Adulthood	30	100	Whole brain	40	5	X		12 months
Zhao (2007)	Rat	Early Adulthood	76	100	Whole brain	40-45	5	X		12 months

Cognitive and Radiological Findings of Human (Table A.3) and Rodent (Table A.4) Studies

Table A.3. Human studies of both cognitive and radiological radiation-induced brain injuries detected within a single cohort.

Author	Findings
Aoyama (2007)	"Most patients who had Grade 1-2 radiologic leukoencephalopathy did not show clinically meaningful signs of neurocognitive dysfunction as assessed by the MMSE. Although 12 patients (50%) developed radiologic Grade 3 (large confluent areas) or worse leukoencephalopathy, only 6 of these 12 patients had clinical abnormalities."
Armstrong (2002)	"The slopes of late treatment-related cognitive decline did not correlate significantly with the slopes of increasing radiographic hyperintensities. Selective cognitive declines (in visual memory) emerged only at 5 years, whereas ratings of clinical MRI (T2 images) showed mild accumulation of hyperintensities with post-treatment onset from 6 months to 3 years, with no further progression."
Bompaire (2018)	"On neuropsychological examination, patients displayed a global and severe cognitive decline through a subcortical frontal mode. The cognitive changes observed were not hippocampic, but related to executive dysfunction. On MRI, 68% of the patients had extensive FLAIR hyperintensities with anterior predominance, 87% had brain atrophy, T2*-weighted MRI showed small asignal areas in 53% of the patients. These abnormalities are evocative of cerebral small vessel disease. Fractional anisotropy in the corpus callosum correlated with cognitive evaluation."
Chapman (2012)	"Using receiver operating characteristic curves, early cingulum longitudinal diffusivity changes predicted for post-radiotherapy changes in verbal recall scores."
Chapman (2016)	"In a multivariate model, increased radial diffusion at the end of radiotherapy significantly predicted decline in verbal fluency 18 months after radiotherapy."
Correa (2012)	"Patients with more extensive white matter disease had lower scores on tests of set-shifting and memory."
Davidson (2000)	"In this study, children who received cranial radiation treatment and who, in many cases, had evidence of both cognitive impairment and neuroimaging abnormalities did not have significant 1H-MRS abnormalities."
Douw (2009)	"White matter hyperintensities and global cortical atrophy were associated with worse cognitive functioning in several cognitive domains."

Table A.3. Continued

Author	Findings
Edelmann (2014)	"There were significant associations between poor neurocognitive performance and brain imaging, particularly for frontal and temporal white and gray matter volume."
Follin (2016)	"Acute lymphoblastic leukemia survivors scored lower than controls in vocabulary, memory, learning capacity, spatial ability, and executive functions and attention. Compared to controls, ALL survivors had reduced white matter and gray matter volumes. Acute lymphoblastic leukemia survivors had lower levels of white matter NAA/Cr, lower levels of gray matter NAA/Cr, and higher levels of WM mI/NAA compared to controls."
Johannesen (2003)	"Compared to the matched reference group, patients with white matter changes grade 3 (52% of total sample) reported significantly worse physical, cognitive, and social function. Patients with white matter changes grade 1 and 2 did not report significantly different quality of life compared to the reference population."
Khong (2006)	"Change in the percentage of fractional anisotropy had a significant effect on FSIQ, VIQ, and PIQ after adjusting for effects of age at treatment, irradiation dose, and time interval from treatment."
King (2015)	"Lower long-term intellectual outcomes of childhood brain tumor survivors are associated with lower white matter integrity."
Lin (2021)	"Furthermore, progressive atrophy in the WM of the right ITG was positively correlated with cognitive decline over time in NPC patients post-RT"
Morrison (2021)	"Relative to other patients, CMBs developed in the individual patient at a rate which was similar to their decline in memory performance."
Mulhern (2001)	"Normal appearing white matter accounted for a significant amount of the association between age at cranial radiotherapy and IQ, factual knowledge, and verbal and nonverbal thinking, but not sustained attention or verbal memory."
Mulhern (2004)	"Reduced cerebral normal appearing white matter is significantly associated with deficits in attention among patients treated for malignant brain tumors."

Table A.3. Continued

Author	Findings
Omuro (2005)	"Neurotoxicity presented as a rapidly progressive subcortical dementia characterized by psychomotor slowing, executive and memory dysfunction, behavioral changes, gait ataxia, and incontinence. Imaging findings revealed diffuse white matter disease and cortical-subcortical atrophy."
Postma (2002)	"The presence and extent of cerebral atrophy correlated significantly with graphomotor speed, information processing capacity, and memory performance. The existence of white matter abnormalities correlated significantly with attention, information processing capacity, and memory performance."
Rashid (2017)	"These prospective data demonstrate a significant decrease in corpus callosum regional volumes after cranial radiation therapy, with associated decline in neurocognitive function, most notably in manual dexterity, attention, and working memory."
Reddick (2003)	"Significant associations were found between normal appearing white matter volumes and both attentional abilities and IQ, and between attentional abilities and IQ. Subsequent analyses supported the hypothesis that attentional abilities, but not memory, could explain a significant amount of the relationship between normal appearing white matter and IQ."
Reddick (2014)	"Decreased WMV is associated with significantly lower scores in intelligence, attention, and academic performance in survivors."
Redmond (2018)	"Within temporal white matter, across all 4 visits, after controlling for age and sex, the association between ADC and verbal learning were both significant—in both instances, performance decreasing with increased regional ADC. Within the genu, across all 4 visits, after controlling for age and sex, the association between FA and motor speed was significant. Within the corpus callosum body, across all 4 visits, after controlling for age and sex, the association between ADC and motor speed was significant, with speed decreasing with increased ADC. Similarly, the association between FA and motor speed was also marginally significant, with motor speed decreasing with decreased FA."
Riggs (2014)	"Performance on the general index of the Children's Memory Scale was significantly correlated with measures of hippocampal volume and uncinate fasciculus."

Table A.3. Continued

Author	Findings
Roddy (2016)	"In multivariable analysis, children with cerebral microbleeds performed worse on the Groton Maze Learning test compared with those without cerebral microbleeds, indicating worse executive function when cerebral microbleeds are present. Cerebral microbleeds in the frontal lobe were associated with worse performance on the Groton Maze Learning test. Presence of cerebral microbleeds in the temporal lobes affected verbal memory."
Schuitema (2013)	"Decreases in FA correlated well with neuropsychological dysfunction."
Simo (2016)	"Cognitive deterioration was correlated with gray matter density and fractional anisotropy."
Tibbs (2020)	"We found that radiation-mediated injury (lower FA, higher MD, and decreased volume with increasing RT dose) to left perisylvian white matter is significantly correlated with poorer language scores over time."
Tringale (2019)	Brain tumor patients exhibited visuospatial memory decline post-radiotherapy. Microstructural damage to critical memory regions, including the hippocampus and medial temporal lobe white matter, were associated with post-radiotherapy memory decline.

Table A.4. Rodent studies of both cognitive and radiological radiation-induced brain injuries detected within a single cohort.

Author	Findings
Atwood (2007)	"In the study reported here, radiation-induced cognitive impairment was accompanied by a significant change in rat brain metabolites at 52 weeks postirradiation, including an increase in the NAA/tCr ratio."
Brown (2016)	"The developing brains of juvenile rats given clinically relevant fractionated doses of whole brain irradiation show few abnormalities in the subacute phase but marked late cognitive alterations that may be linked with perturbed magnetic resonance spectroscopy signals measured in the corpus callosum. As for cognitive measures, the most dramatic impairments were in novel object recognition late after either dose of whole brain irradiation."
He (2021)	"...elicited chronic RBI as characterized by brain atrophy, memory and cognitive deficits…"
Peiffer (2014)	"Hippocampal performance was impaired in IR-30 (irradiated with 30 Gy) but not IR-39 (irradiated with 39 Gy) animals. While gross size differences exist, white matter integrity is preserved in rats after fWBI at 5 weeks."
Perez (2018)	"… males demonstrated odor recognition memory impairment and volume reduction in regions important for olfactory processing…"
Sahnoune (2018)	"Cranial radiation therapy caused early and lasting impairments in task acquisition, accuracy, and latency to correct response, as well as causing stunting of growth and changes in brain volume and diffusion."
Tang (2019)	"Cognitive measurements were found to be significantly correlated with six image features that included myelin integrity and local organization of the neural network."

APPENDIX B. SUPPORTING INFORMATION FOR CHAPTER 4

Magnetic Resonance Spectroscopy Voxel Placements and Corresponding LCModel Spectra

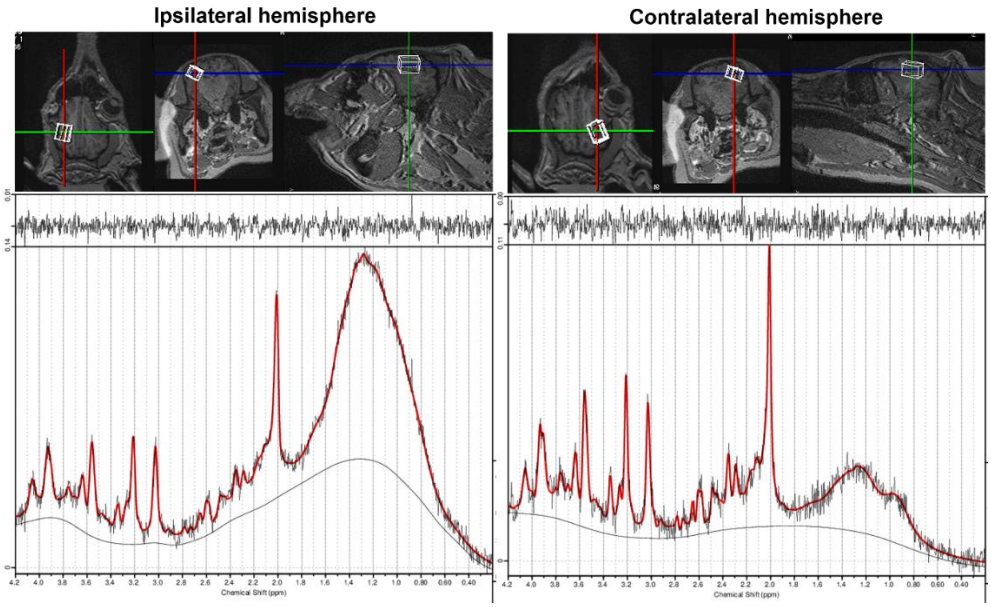

Figure B.1. Representative voxel placements and their corresponding spectra within the ipsilateral and contralateral hemispheres for P1 (25 Gy) at 0 months post-irradiation.

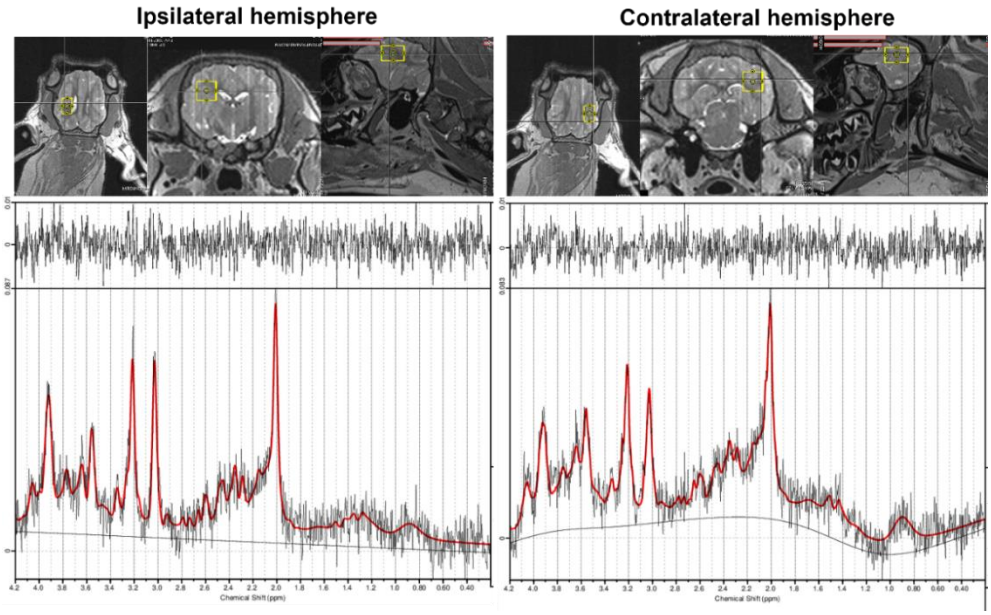

Figure B.2. Representative voxel placements and their corresponding spectra within the ipsilateral and contralateral hemispheres for P1 (25 Gy) at 3 months post-irradiation.

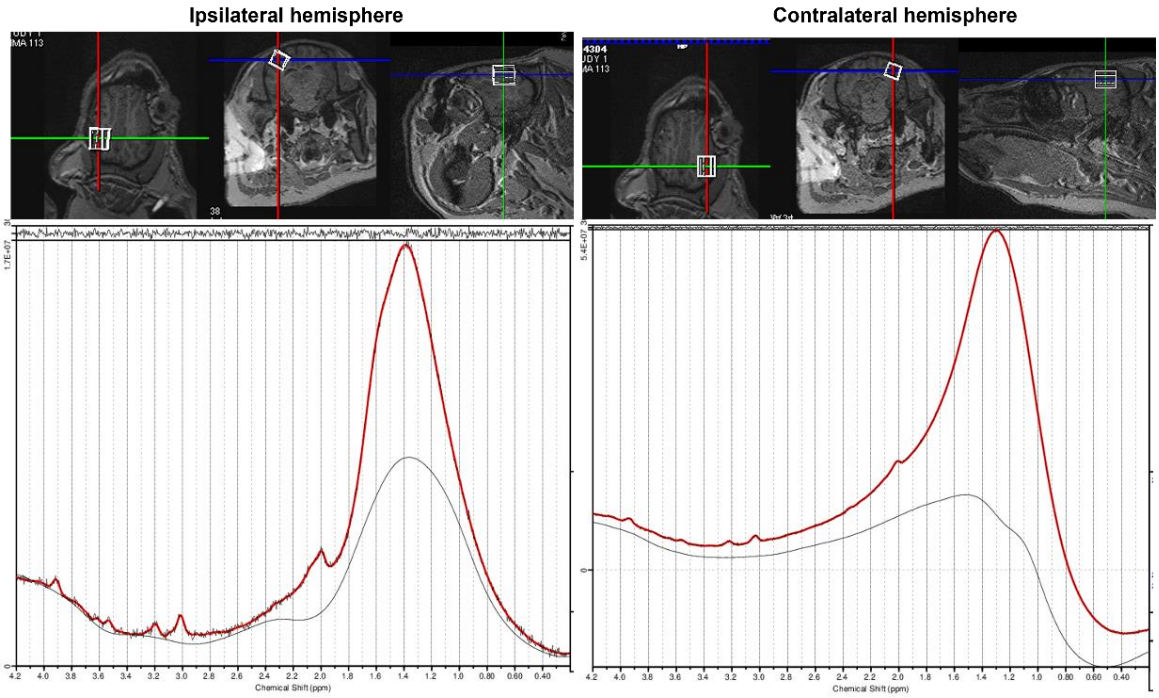

Figure B.3. Representative voxel placements and their corresponding spectra within the ipsilateral and contralateral hemispheres for P2 (25 Gy) at 0 months post-irradiation.

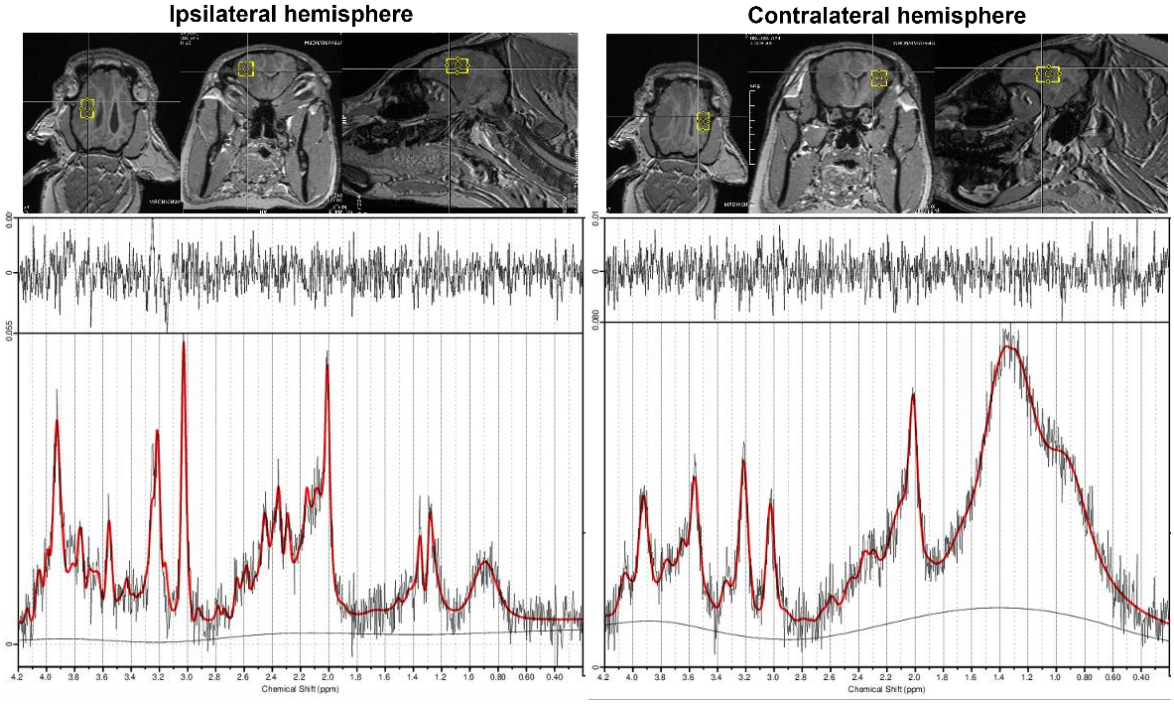

Figure B.4. Representative voxel placements and their corresponding spectra within the ipsilateral and contralateral hemispheres for P2 (25 Gy) at 3 months post-irradiation.

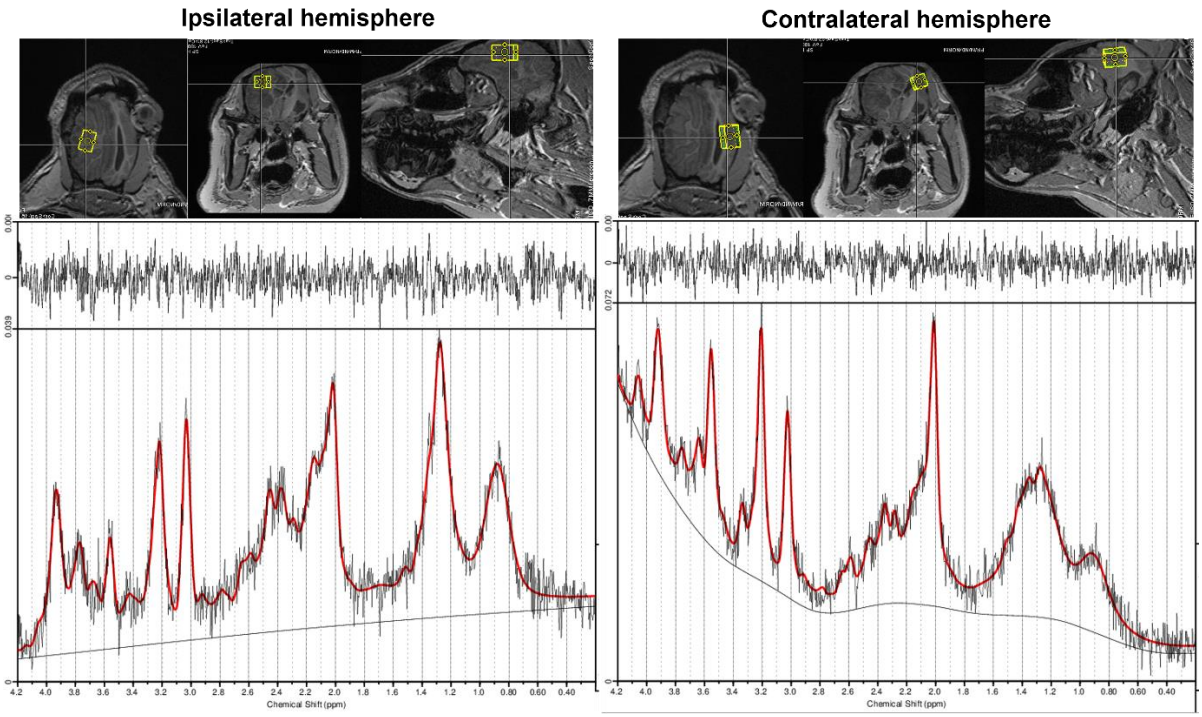

Figure B.5. Representative voxel placements and their corresponding spectra within the ipsilateral and contralateral hemispheres for P2 (25 Gy) at 4 months post-irradiation.

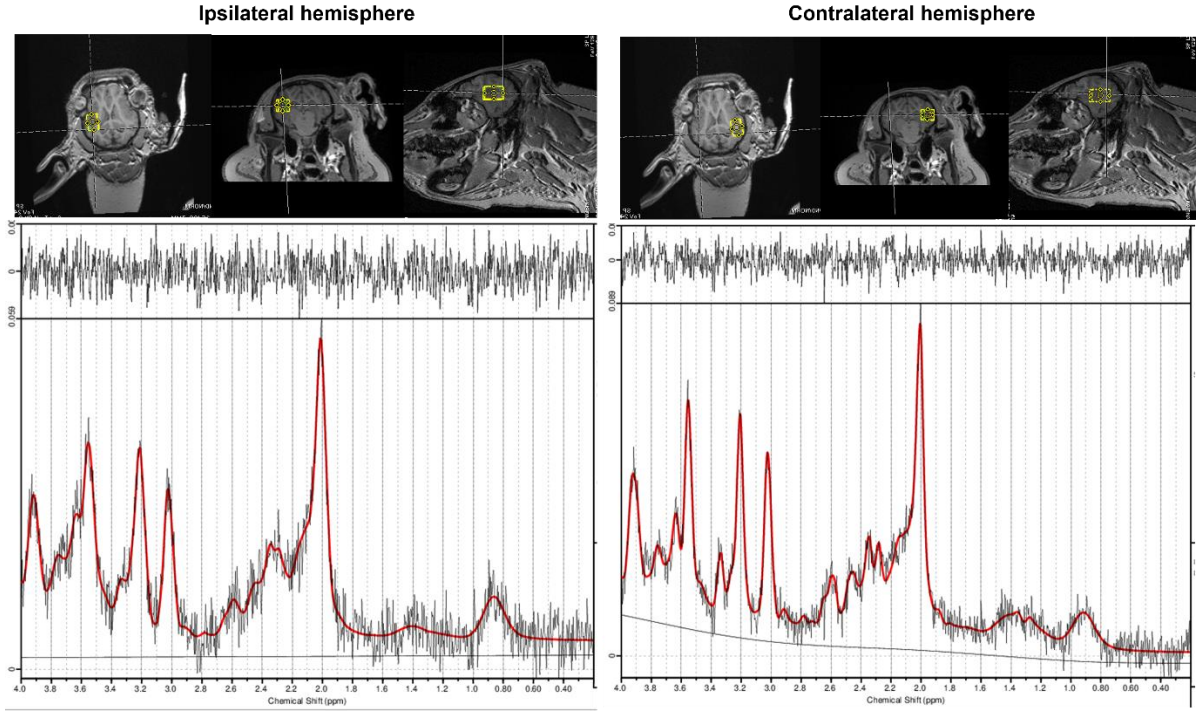

Figure B.6. Representative voxel placements and their corresponding spectra within the ipsilateral and contralateral hemispheres for P3 (15 Gy) at 0 months post-irradiation.

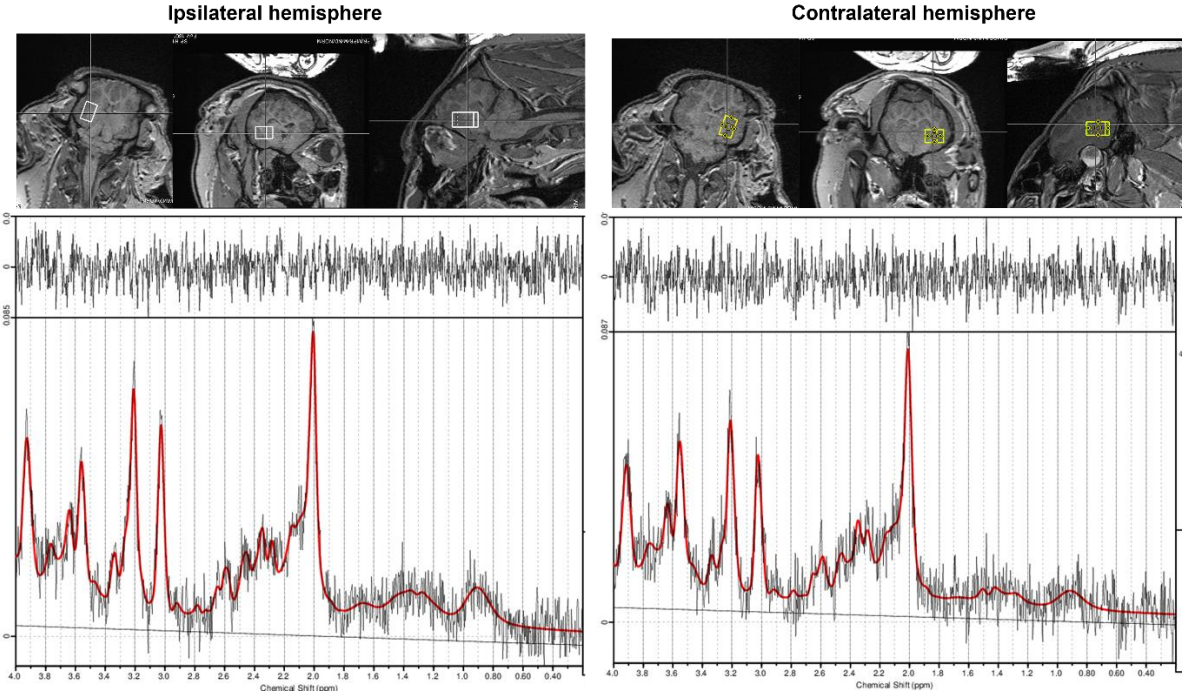

Figure B.7. Representative voxel placements and their corresponding spectra within the ipsilateral and contralateral hemispheres for P3 (15 Gy) at 3 months post-irradiation.

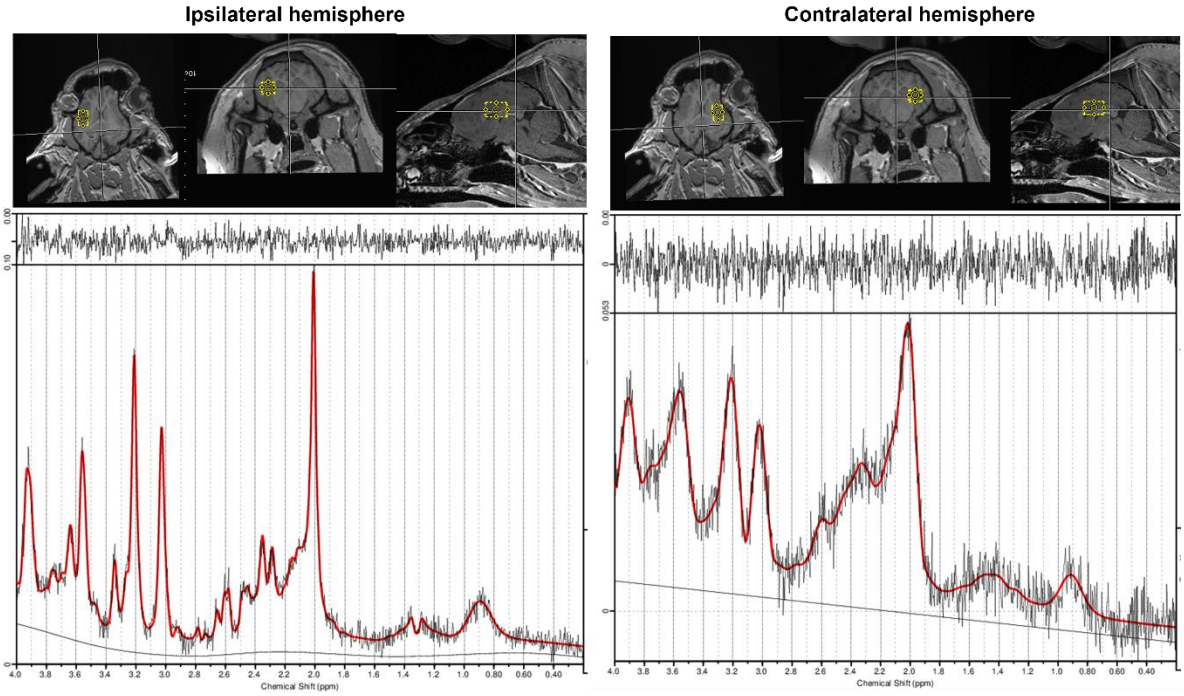

Figure B.8. Representative voxel placements and their corresponding spectra within the ipsilateral and contralateral hemispheres for P3 (15 Gy) at 6 months post-irradiation.

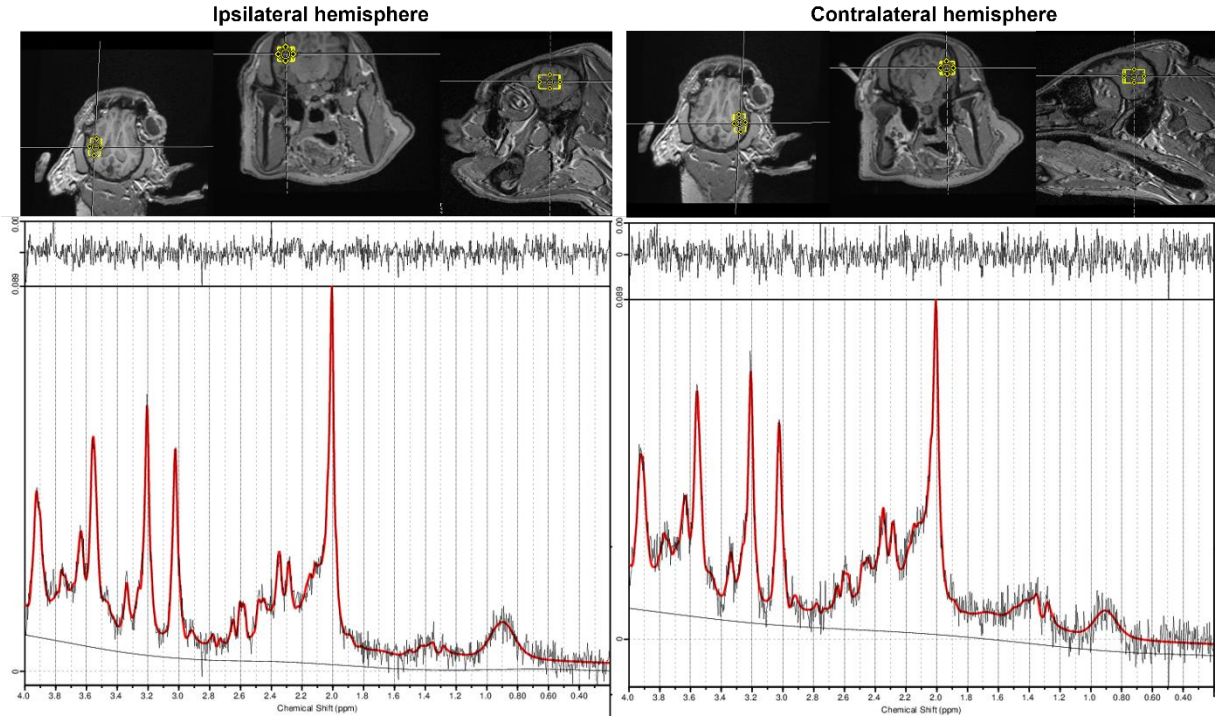

Figure B.9. Representative voxel placements and their corresponding spectra within the ipsilateral and contralateral hemispheres for P4 (15 Gy) at 0 months post-irradiation.

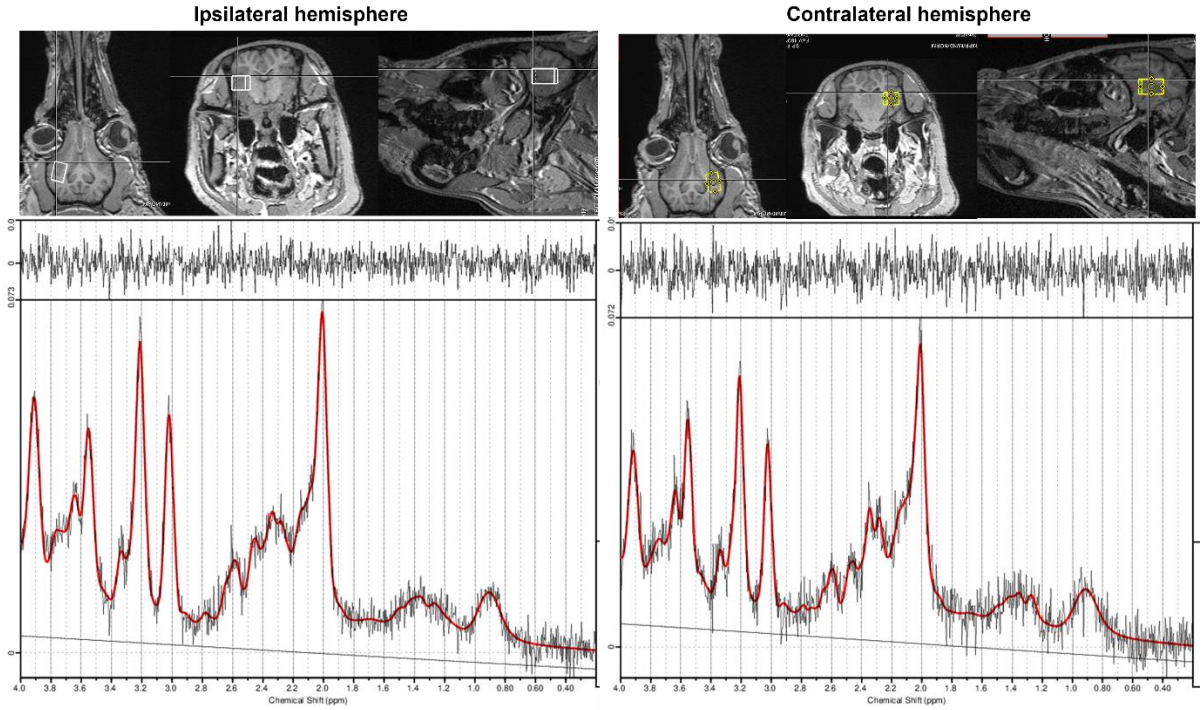

Figure B.10. Representative voxel placements and their corresponding spectra within the ipsilateral and contralateral hemispheres for P4 (15 Gy) at 3 months post-irradiation.

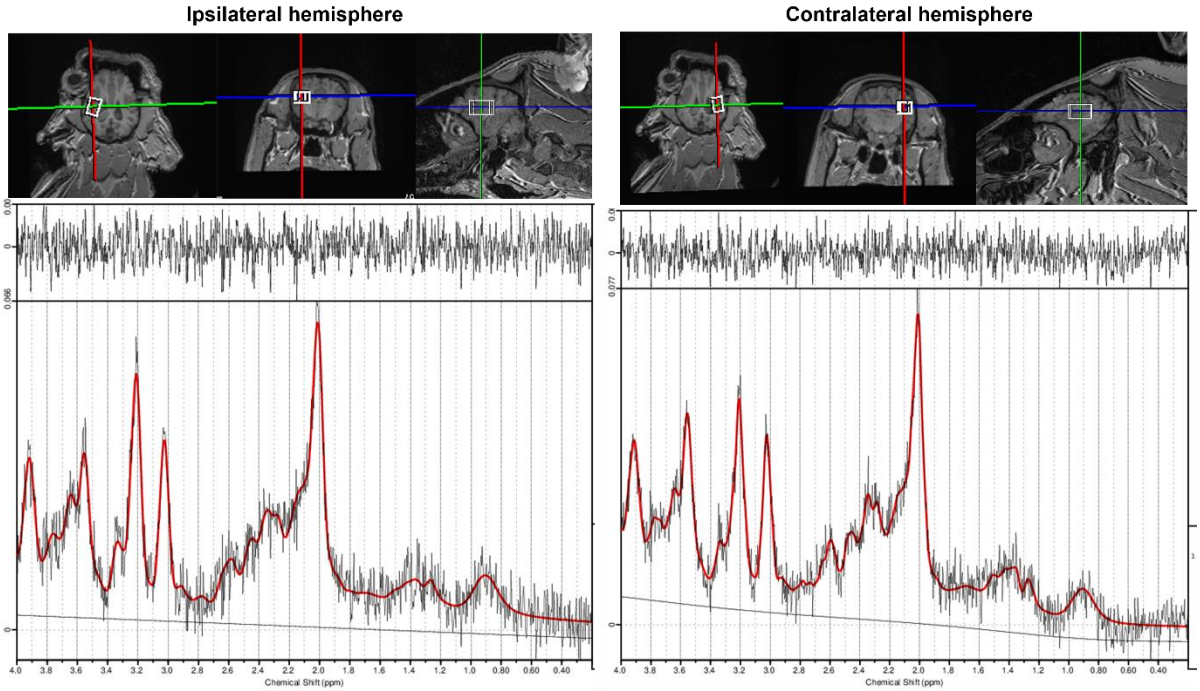

Figure B.11. Representative voxel placements and their corresponding spectra within the ipsilateral and contralateral hemispheres for P4 (15 Gy) at 6 months post-irradiation.

Statistical Analysis Methods for 25 Gy and 15 Gy Cohort Diffusion Tensor Imaging and Magnetic Resonance Spectroscopy Measurements

Statistical analyses were performed using SPSS (v.28.0, SPSS Inc., Chicago, IL). FA values, ADC values, and metabolite concentrations were independently evaluated using a repeated measures two-way ANOVA with follow-up time points and corresponding hemisphere set as independent variables. Significance was established with $p \leq 0.05$ and corrected for multiple comparisons using the Holm-Sidak method when appropriate.

Cohort Analyses of Magnetic Resonance Spectroscopy Measurements

A 25 Gy dose prescription induced significant metabolite changes pertaining to neurotransmitter function and energy metabolism. A repeated measures two-way ANOVA revealed a significant main effect of follow-up time on Glx measurements ($F(1,1)= 2008.241$, $p<0.05$, $\eta_p^2=1.000$). Indeed, mean Glx values increased over time regardless of association to the ipsilateral (0 months=4.38 AU, 3 months=11.49 AU) or contralateral hemisphere (0 months=7.02 AU, 3 months=9.27 AU) (Fig B.12c). There was also a significant interaction between follow-up time and hemisphere on the tCr measurements ($F(1,1)= 307.843$, $p<0.05$, $\eta_p^2=0.997$). Specifically, mean tCr values of the ipsilateral hemisphere increased from 3.82 AU at 0 months to 5.25 AU at 3 months; the mean tCr values of the contralateral hemisphere also increased from 3.74 AU at 0 months to 4.67 AU at 3 months (Fig B.12e).

Similar to the previous prescription, a 15 Gy dose also brought about a significant metabolite change in regard to neurotransmitter function. A repeated measures two-way ANOVA revealed a significant main effect of follow-up time on Glx measurements ($F(2,2)=28.883$, $p<0.05$, $\eta_p^2=0\ .967$). Interestingly, mean Glx values within the ipsilateral hemisphere increased from 0 months (8.96 AU) to 3 months (14.03 AU) and then decreased thereafter at 6 months (11.36 AU). Mean Glx values within the contralateral hemisphere increased over time (0 months=12.12 AU, 3 months=12.26 AU, 6 months=13.31) (Fig 13c).

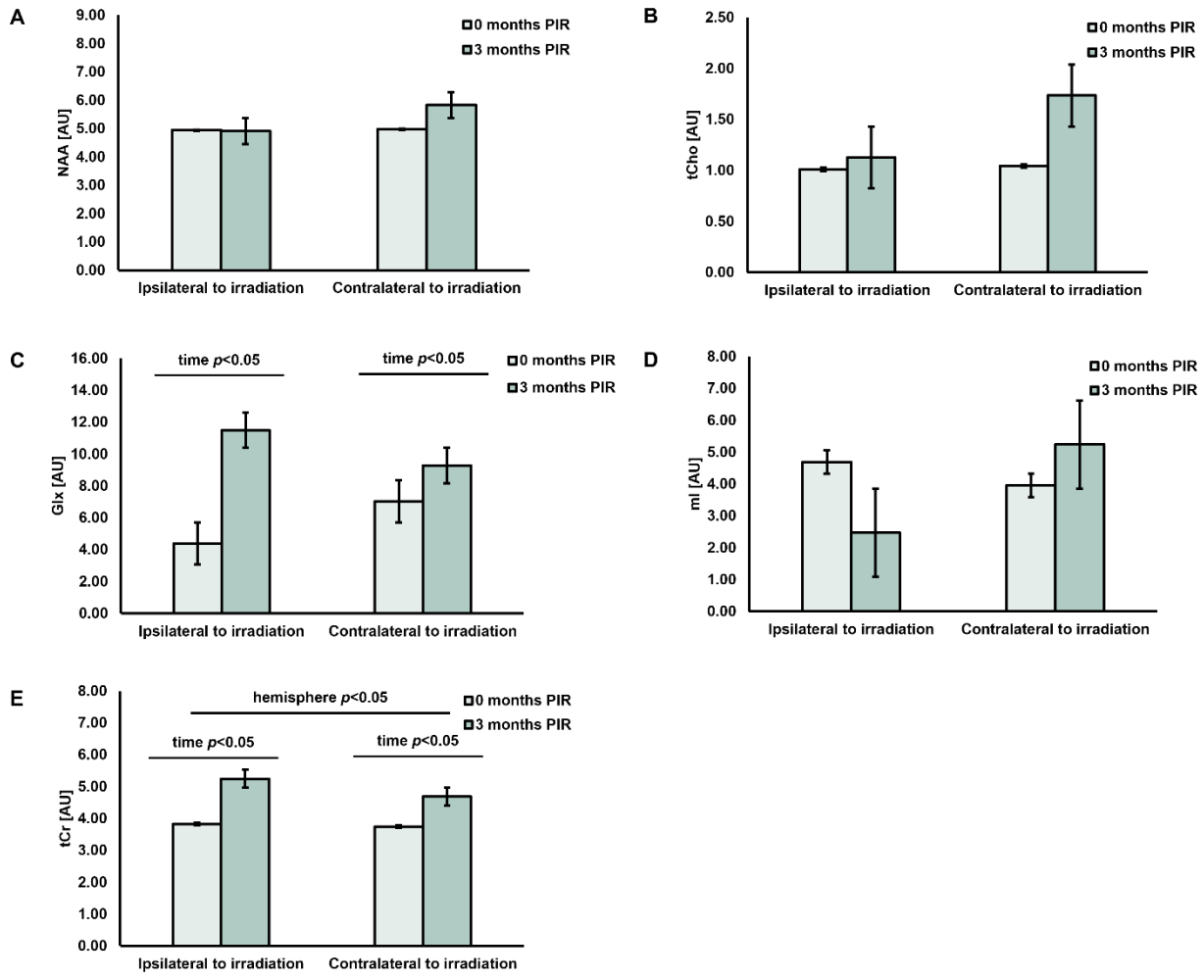

Figure B.12. Effect of 25 Gy dose prescription to concentrations of (a) NAA, (b) tCho, (c) Glx, (d) mI, and (e) tCr over time. Corresponding effects of the contralateral hemisphere are shown as a comparison. Error bars denote the standard error. AU is defined as arbitrary units.

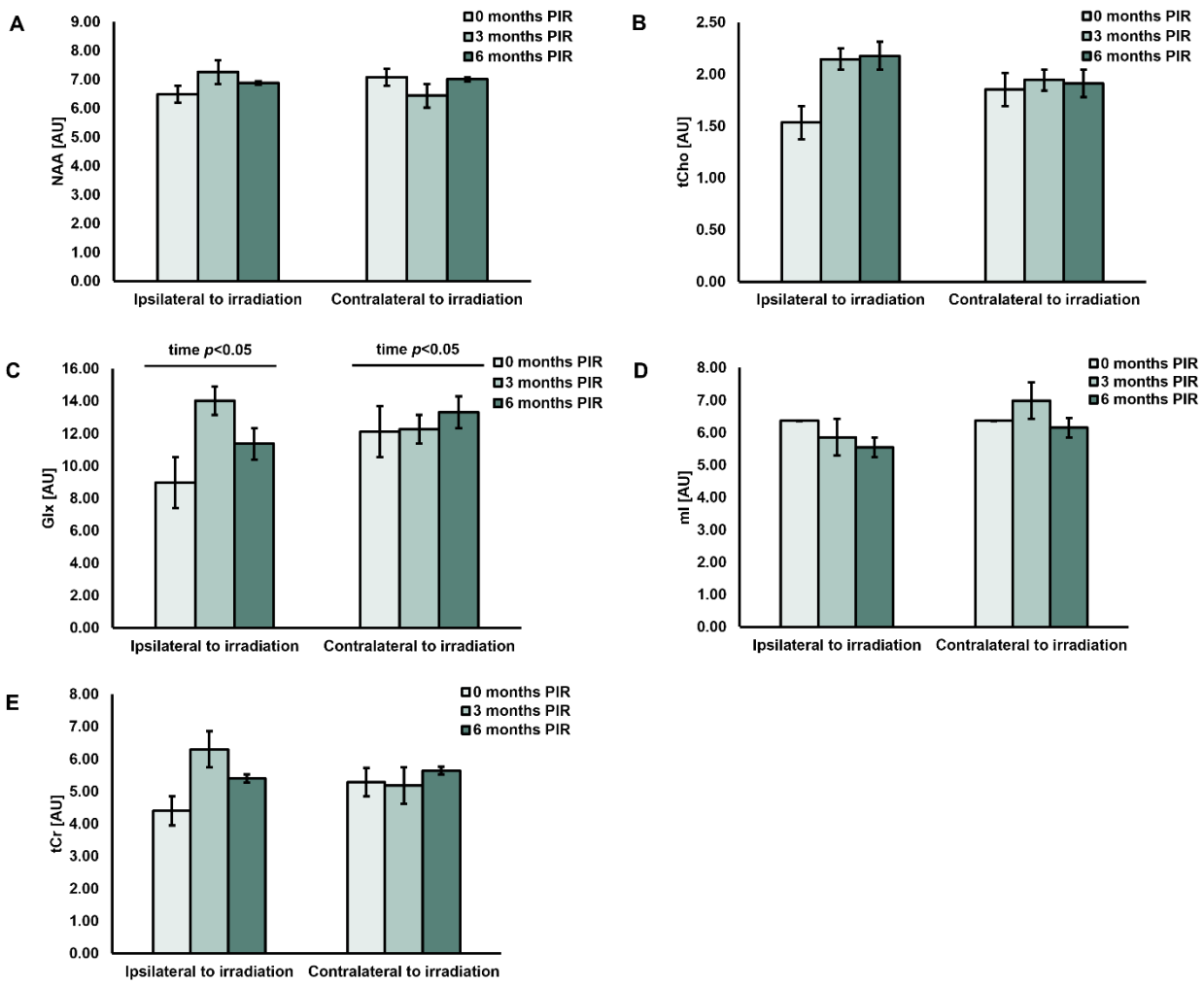

Figure B.13. Effect of 15 Gy dose prescription to concentrations of (a) NAA, (b) tCho, (c) Glx, (d) mI, and (e) tCr over time. Corresponding effects of the contralateral hemisphere are shown as a comparison. Error bars denote the standard error. AU is defined as arbitrary units.

Cohort Analyses of Diffusion Tensor Imaging Measurements

FA measurements significantly changed within the 25 Gy cohort without any significant corresponding changes in ADC. A repeated measures two-way ANOVA revealed a significant interaction between follow-up time and hemisphere on the FA of the IC ($F(1,5)=20.97$, $p<0.05$, $\eta_p^2=0.129$). Specifically, the mean FA of the ipsilateral hemisphere decreased from 0.55 at 0 months to 0.45 at 3 months; the mean FA of the contralateral hemisphere increased from 0.41 at 0 months to 0.63 at 3 months (Fig B.14a). Looking at the CC, there was a significant main effect of solely hemisphere on FA values ($F(1,5)=7.606$, $p<0.05$, $\eta_p^2=0.603$). Indeed, mean FA measurements of the ipsilateral hemisphere (0 months=0.33, 3 months=0.44) were lower than the corresponding time points within the contralateral hemisphere (0 months=0.41, 3 months=0.52) (Fig B.14c).

By way of contrast, ADC measurements significantly changed within the 15 cohort without any significant corresponding changes in FA values. A repeated measures two-way ANOVA revealed a significant main effect of follow-up time on ADC within the IC ($F(2,10)=13.046$, $p<0.05$, $\eta_p^2=0.723$). Specifically, mean ADC values decreased over time regardless of association to the ipsilateral (0 months=0.64, 3 months=0.60, 6 months=0.56) or contralateral hemisphere (0 months=0.65, 3 months=0.58, 6 months=0.59) (Fig B.15b).

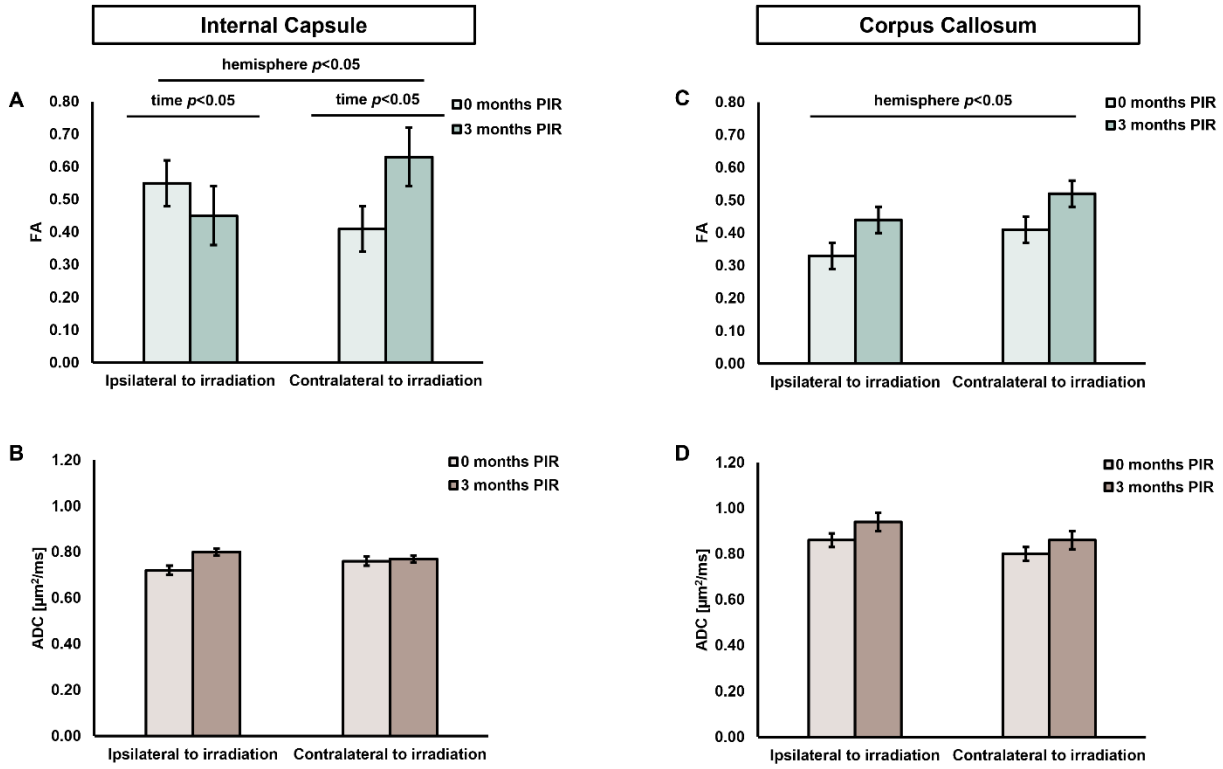

Figure B.14. Effect of 25 Gy dose prescription to FA and ADC measurements over time within the internal capsule (a-b) and corpus callosum (c-d) white matter tracts. Corresponding effects of the contralateral hemisphere are shown as a comparison. Error bars denote the standard error.

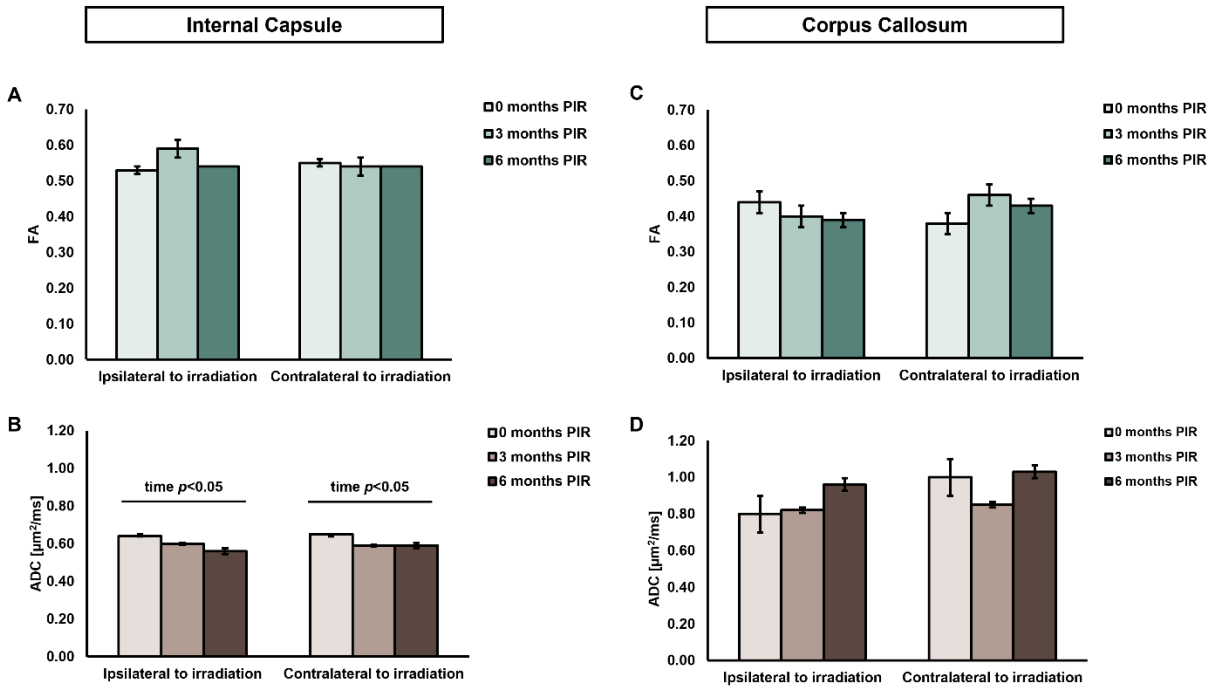

Figure B.15. Effect of 15 Gy dose prescription to FA and ADC measurements over time within the internal capsule (a-b) and corpus callosum (c-d) white matter tracts. Corresponding effects of the contralateral hemisphere are shown as a comparison. Error bars denote the standard error.

Raw Values of Magnetic Resonance Spectroscopy Measurements

Table B.1. Metabolite concentrations for P1 (25 Gy).

Metabolites	Ipsilateral		Contralateral	
	Concentration	% SD	Concentration	% SD
Baseline				
NAA	3.17	14.00	3.38	10.00
tCho	0.83	16.00	0.82	10.00
Glx	3.36	61.00	6.70	26.00
mI	3.94	17.00	3.12	17.00
tCr	3.74	9.00	3.34	7.00
3 months				
NAA	3.36	5.00	4.92	6.00
tCho	0.74	8.00	1.63	7.00
Glx	12.44	5.00	7.19	14.00
mI	1.13	31.00	4.28	15.00
tCr	4.87	3.00	4.02	6.00
4 months				
NAA	2.30	7.00	4.60	5.00
tCho	0.67	8.00	1.65	4.00
Glx	8.92	4.00	8.31	10.00
mI	0.00	999.00	4.18	9.00
tCr	3.22	4.00	3.95	4.00

Table B.2. Metabolite concentrations for P2 (25 Gy).

Metabolites	**Ipsilateral**		**Contralateral**	
	Concentration	**% SD**	**Concentration**	**% SD**
Baseline				
NAA	6.71	4.00	6.57	3.00
tCho	1.19	5.00	1.27	4.00
Glx	5.40	16.00	7.34	8.00
mI	5.44	8.00	4.79	7.00
tCr	3.90	4.00	4.15	4.00
3 months				
NAA	6.46	5.00	6.74	6.00
tCho	1.52	6.00	1.84	6.00
Glx	10.54	7.00	11.36	9.00
mI	3.81	14.00	6.20	5.00
tCr	5.62	4.00	5.35	5.00

Table B.3. Metabolite concentrations for P3 (15 Gy).

Metabolites	**Ipsilateral**		**Contralateral**	
	Concentration	**% SD**	**Concentration**	**% SD**
Baseline				
NAA	6.37	6.00	7.24	4.00
tCho	1.46	6.00	1.86	4.00
Glx	8.96	7.00	11.34	6.00
mI	7.08	3.00	6.11	8.00
tCr	4.21	5.00	5.48	3.00
3 months				
NAA	7.15	5.00	7.46	6.00
tCho	1.87	5.00	1.88	7.00
Glx	12.67	7.00	12.37	8.00
mI	6.55	4.00	7.48	12.00
tCr	5.86	4.00	5.40	5.00
6 months				
NAA	7.43	3.00	6.96	7.00
tCho	2.24	2.00	2.06	8.00
Glx	10.77	5.00	13.64	7.00
mI	5.68	6.00	6.27	17.00
tCr	5.86	2.00	5.91	4.00

Table B.4. Metabolite concentrations for P4 (15 Gy).

Metabolites	**Ipsilateral**		**Contralateral**	
	Concentration	**% SD**	**Concentration**	**% SD**
Baseline				
NAA	6.61	3.00	6.91	4.00
tCho	1.61	3.00	1.85	4.00
Glx	8.97	5.00	12.90	5.00
mI	5.65	5.00	6.63	7.00
tCr	4.59	2.00	5.10	3.00
3 months				
NAA	7.37	4.00	5.42	6.00
tCho	2.43	4.00	2.01	5.00
Glx	15.38	4.00	12.15	6.00
mI	5.15	11.00	6.49	9.00
tCr	6.74	3.00	4.96	4.00
6 months				
NAA	6.34	6.00	7.06	6.00
tCho	2.19	5.00	1.76	6.00
Glx	11.95	6.00	12.98	6.00
mI	5.41	13.00	6.03	12.00
tCr	4.94	4.00	5.37	4.00

Table B.5. Mean metabolite concentrations for P1 and P2 (25 Gy).

Metabolites	**Ipsilateral**		**Contralateral**	
	Mean ± SD	**Mean % SD**	**Mean ± SD**	**Mean % SD**
Baseline (n=2)				
NAA	4.94 ± 2.51	9.00	4.98 ± 2.26	6.50
tCho	1.01 ± 0.26	10.50	1.04 ± 0.32	7.00
Glx	4.38 ± 1.45	38.50	7.02 ± 0.45	17.00
mI	4.69 ± 1.06	12.50	3.95 ± 1.19	12.00
tCr	3.82 ± 0.11	6.50	3.74 ± 0.57	5.50
3 months (n=2)				
NAA	4.91 ± 2.19	5.00	5.83 ± 1.29	6.00
tCho	1.13 ± 0.55	7.00	1.73 ± 0.15	6.50
Glx	11.49 ± 1.34	6.00	9.27 ± 2.95	11.50
mI	2.47 ± 1.89	22.50	5.24 ± 1.36	10.00
tCr	5.25 ± 0.53	3.50	4.67 ± 0.95	6.50
4 months (n=1)				
NAA	2.30	7.00	4.60	5.00
tCho	0.67	8.00	1.65	4.00
Glx	8.92	4.00	8.31	10.00
mI	0.00	999.00	4.18	9.00
tCr	3.22	4.00	3.95	4.00

Table B.6. Mean metabolite concentrations for P3 and P4 (15 Gy).

Metabolites	**Ipsilateral**		**Contralateral**	
	Mean ± SD	**Mean % SD**	**Mean ± SD**	**Mean % SD**
Baseline (n=2)				
NAA	6.49 ± 0.17	4.50	7.07 ± 0.23	4.00
tCho	1.53 ± 0.10	4.50	1.85 ± 0.01	4.00
Glx	8.96 ± 0.01	6.00	12.12 ± 1.10	5.50
mI	6.37 ± 1.01	4.00	6.37 ± 0.36	7.50
tCr	4.40 ± 0.27	3.50	5.29 ± 0.27	3.00
3 months (n=2)				
NAA	7.26 ± 0.16	4.50	6.44 ± 1.44	6.00
tCho	2.14 ± 0.40	4.50	1.94 ± 0.09	6.00
Glx	14.03 ± 1.92	5.50	12.26 ± 0.15	7.00
mI	5.85 ± 0.99	7.50	6.99 ± 0.70	10.50
tCr	6.30 ± 0.62	3.50	5.18 ± 0.31	4.50
6 months (n=2)				
NAA	6.88 ± 0.77	4.50	7.01 ± 0.07	6.50
tCho	2.18 ± 0.08	3.50	1.91 ± 0.22	7.00
Glx	11.36 ± 0.83	5.50	13.31 ± 0.47	6.50
mI	5.54 ± 0.19	9.50	6.15 ± 0.17	14.50
tCr	5.40 ± 0.65	3.00	5.64 ± 0.39	4.00

Table B.7. Mean metabolite concentrations normalized to total creatine for P1 and P2 (25 Gy).

Metabolites	**Ipsilateral**		**Contralateral**	
	Mean ± SD	**Mean % SD**	**Mean ± SD**	**Mean % SD**
Baseline (n=2)				
NAA/tCr	1.20 ± 0.49	9.00	1.23 ± 0.31	7.50
tCho/tCr	0.26 ± 0.06	10.00	0.3 ± 0.07	7.50
Glx/tCr	1.38 ± 0.69	36.50	1.87 ± 0.19	20.50
mI/tCr	1.09 ± 0.05	11.50	1.15 ± 0.31	12.00
3 months (n=2)				
NAA/tCr	0.92 ± 0.33	5.00	1.24 ± 0.02	6.00
tCho/tCr	0.21 ± 0.08	6.50	0.37 ± 0.04	6.50
Glx/tCr	2.21 ± 0.48	6.00	1.96 ± 0.23	11.50
mI/tCr	0.46 ± 0.32	22.50	1.11 ± 0.07	10.00
4 months (n=1)				
NAA/tCr	0.71	7.00	1.17	5.00
tCho/tCr	0.21	8.00	0.42	4.00
Glx/tCr	2.77	4.00	2.10	10.00
mI/tCr	0	999.00	1.06	9.00

Table B.8. Mean metabolite concentrations normalized to total creatine for P3 and P4 (15 Gy).

Metabolites	**Ipsilateral**		**Contralateral**	
	Mean ± SD	**Mean % SD**	**Mean ± SD**	**Mean % SD**
Baseline (n=2)				
NAA/tCr	1.48 ± 0.05	4.50	1.34 ± 0.03	4.00
tCho/tCr	0.35 ± 0.00	4.50	1.86 ± 0.02	4.00
Glx/tCr	2.04 ± 0.12	6.00	2.3 ± 0.33	5.50
mI/tCr	1.46 ± 0.32	4.00	1.21 ± 0.13	7.50
3 months (n=2)				
NAA/tCr	1.16 ± 0.09	4.50	1.24 ± 0.20	6.00
tCho/tCr	0.34 ± 0.03	4.50	0.38 ± 0.04	6.00
Glx/tCr	2.22 ± 0.08	5.50	2.37 ± 0.11	7.00
mI/tCr	0.94 ± 0.25	7.50	1.35 ± 0.05	10.50
6 months (n=2)				
NAA/tCr	1.28 ± 0.01	4.50	1.25 ± 0.10	5.50
tCho/tCr	0.41 ± 0.03	3.50	0.34 ± 0.02	7.00
Glx/tCr	2.13 ± 0.41	5.50	2.36 ± 0.08	6.50
mI/tCr	1.03 ± 0.09	9.50	1.09 ± 0.04	14.50

Raw Values of Diffusion Tensor Imaging Measurements

Table B.9. Fractional anisotropy values and apparent diffusion coefficients for P1 (25 Gy).

White Matter Tracts	**Fractional Anisotropy (image mean ± image SD)**		**Apparent Diffusion Coefficient (image mean ± image SD)**	
	Ipsilateral	**Contralateral**	**Ipsilateral**	**Contralateral**
Baseline				
Internal capsule	0.58 ± 0.15	0.41 ± 0.15	0.72 ± 0.09	0.78 ± 0.20
Corpus callosum	0.32 ± 0.11	0.44 ± 0.15	0.94 ± 0.23	0.85 ± 0.18
3 months				
Internal capsule	0.29 ± 0.10	0.59 ± 0.16	0.91 ± 0.15	0.80 ± 0.17
Corpus callosum	0.33 ± 0.11	0.46 ± 0.14	1.14 ± 0.23	1.11 ± 0.56
4 months				
Internal capsule	0.14 ± 0.06	0.62 ± 0.19	1.21 ± 0.32	0.88 ± 0.34
Corpus callosum	0.29 ± 0.11	0.34 ± 0.11	1.10 ± 0.15	1.11 ± 0.48

Table B.10. Fractional anisotropy values and apparent diffusion coefficients for P2 (25 Gy).

White Matter Tracts	**Fractional Anisotropy (image mean ± image SD)**		**Apparent Diffusion Coefficient (image mean ± image SD)**	
	Ipsilateral	**Contralateral**	**Ipsilateral**	**Contralateral**
Baseline				
Internal capsule	0.52 ± 0.19	0.41 ± 0.16	0.76 ± 0.19	0.94 ± 0.16
Corpus callosum	0.35 ± 0.16	0.38 ± 0.14	0.86 ± 0.16	0.84 ± 0.14
3 months				
Internal capsule	0.61 ± 0.11	0.67 ± 0.45	0.75 ± 0.11	0.73 ± 0.45
Corpus callosum	0.55 ± 0.29	0.58 ± 0.20	0.81 ± 0.29	0.83 ± 0.20

Table B.11. Fractional anisotropy values and apparent diffusion coefficients for P3 (15 Gy).

White Matter Tracts	**Fractional Anisotropy (image mean ± image SD)**		**Apparent Diffusion Coefficient (image mean ± image SD)**	
	Ipsilateral	**Contralateral**	**Ipsilateral**	**Contralateral**
Baseline				
Internal capsule	0.59 ± 0.15	0.56 ± 0.13	0.64 ± 0.09	0.65 ± 0.07
Corpus callosum	0.50 ± 0.15	0.39 ± 0.13	0.75 ± 0.42	0.94 ± 0.59
3 months				
Internal capsule	0.61 ± 0.13	0.47 ± 0.14	0.56 ± 0.10	0.58 ± 0.10
Corpus callosum	0.45 ± 0.15	0.46 ± 0.19	0.80 ± 0.35	0.73 ± 0.35
6 months				
Internal capsule	0.56 ± 0.13	0.59 ± 0.15	0.56 ± 0.06	0.59 ± 0.06
Corpus callosum	0.36 ± 0.15	0.44 ± 0.20	1.09 ± 0.64	1.16 ± 0.64

Table B.12. Fractional anisotropy values and apparent diffusion coefficients for P4 (15 Gy).

White Matter Tracts	**Fractional Anisotropy (image mean ± image SD)**		**Apparent Diffusion Coefficient (image mean ± image SD)**	
	Ipsilateral	**Contralateral**	**Ipsilateral**	**Contralateral**
Baseline				
Internal capsule	0.48 ± 0.14	0.54 ± 0.15	0.64 ± 0.07	0.64 ± 0.12
Corpus callosum	0.38 ± 0.18	0.37 ± 0.12	0.85 ± 0.41	1.05 ± 0.57
3 months				
Internal capsule	0.57 ± 0.20	0.60 ± 0.15	0.64 ± 0.17	0.59 ± 0.08
Corpus callosum	0.35 ± 0.11	0.46 ± 0.16	0.83 ± 0.37	0.95 ± 0.57
6 months				
Internal capsule	0.52 ± 0.17	0.49 ± 0.16	0.55 ± 0.10	0.60 ± 0.14
Corpus callosum	0.42 ± 0.18	0.42 ± 0.16	0.84 ± 0.44	0.89 ± 0.40

Table B.13. Mean fractional anisotropy values and apparent diffusion coefficients for P1 and P2 (25 Gy).

White Matter Tracts	**Fractional Anisotropy (mean ± SD)**		**Apparent Diffusion Coefficient (mean ± SD)**	
	Ipsilateral	**Contralateral**	**Ipsilateral**	**Contralateral**
Baseline (n=2)				
Internal capsule	0.55 ± 0.17	0.41 ± 0.15	0.74 ± 0.14	0.86 ± 0.18
Corpus callosum	0.33 ± 0.14	0.41 ± 0.15	0.90 ± 0.20	0.84 ± 0.16
3 months (n=2)				
Internal capsule	0.45 ± 0.11	0.63 ± 0.31	0.83 ± 0.13	0.77 ± 0.31
Corpus callosum	0.44 ± 0.20	0.52 ± 0.17	0.98 ± 0.26	0.97 ± 0.38
4 months (n=1)				
Internal capsule	0.14 ± 0.06	0.62 ± 0.19	1.21 ± 0.32	0.88 ± 0.34
Corpus callosum	0.29 ± 0.11	0.34 ± 0.11	1.10 ± 0.15	1.11 ± 0.48

Table B.14. Mean fractional anisotropy values and apparent diffusion coefficients for P3 and P4 (15 Gy).

White Matter Tracts	**Fractional Anisotropy (mean ± SD)**		**Apparent Diffusion Coefficient (mean ± SD)**	
	Ipsilateral	**Contralateral**	**Ipsilateral**	**Contralateral**
Baseline (n=2)				
Internal capsule	0.53 ± 0.14	0.55 ± 0.14	0.64 ± 0.08	0.64 ± 0.10
Corpus callosum	0.44 ± 0.16	0.38 ± 0.12	0.80 ± 0.41	1.00 ± 0.58
3 months (n=2)				
Internal capsule	0.59 ± 0.17	0.53 ± 0.15	0.60 ± 0.14	0.59 ± 0.09
Corpus callosum	0.40 ± 0.13	0.46 ± 0.18	0.81 ± 0.36	0.84 ± 0.46
6 months (n=2)				
Internal capsule	0.54 ± 0.15	0.54 ± 0.16	0.56 ± 0.08	0.59 ± 0.10
Corpus callosum	0.39 ± 0.16	0.43 ± 0.18	0.96 ± 0.54	1.02 ± 0.52

Statistical Analysis for 25 Gy and 15 Gy Cohort Magnetic Resonance Spectroscopy and Diffusion Tensor Imaging Measurements

Table B.15. Results of a repeated measures two-way ANOVA for concentrations of NAA, tCho, Glx, mI, and tCr within the 25 Gy cohort.

Time				
(0 months vs. 3 months)				
	df	***F***	***p***	η_p^2
NAA	1	0.825	0.531	0.452
tCho	1	86.255	0.068	0.989
Glx	1	2008.241	0.014*	1.000
mI	1	1.726	0.414	0.633
tCr	1	17.890	0.148	0.947
Hemisphere				
(Ipsilateral vs. Contralateral)				
	df	***F***	***p***	η_p^2
NAA	1	1.382	0.449	0.580
tCho	1	7.016	0.230	0.875
Glx	1	0.033	0.886	0.032
mI	1	50.378	0.089	0.981
tCr	1	1.066	0.490	0.516
Time x Hemisphere				
	df	***F***	***p***	η_p^2
NAA	1	3.698	0.305	0.787
tCho	1	2.979	0.334	0.749
Glx	1	1.695	0.417	0.629
mI	1	56.338	0.084	0.983
tCr	1	307.843	0.036*	0.997

Table B.16. Results of a repeated measures two-way ANOVA for concentrations of NAA, tCho, Glx, mI, and tCr within the 15 Gy cohort.

Time				
(0 months vs. 3 months vs. 6 months)				
	df	***F***	***p***	η_p^2
NAA	2	0.147	0.872	0.128
tCho	2	2.109	0.322	0.678
Glx	2	28.883	0.033*	0.967
mI	2	1.633	0.380	0.620
tCr	2	3.524	0.221	0.779
Hemisphere				
(Ipsilateral vs. Contralateral)				
	df	***F***	***p***	η_p^2
NAA	1	0.019	0.912	0.019
tCho	1	0.148	0.766	0.129
Glx	1	4.300	0.286	0.811
mI	1	2.132	0.382	0.681
tCr	1	0.000	0.992	0.000
Time x Hemisphere				
	df	***F***	***p***	η_p^2
NAA	2	0.691	0.591	0.409
tCho	2	18.685	0.051	0.949
Glx	2	4.839	0.171	0.829
mI	2	1.240	0.446	0.554
tCr	2	5.682	0.150	0.850

Table B.17. Results of a repeated measures two-way ANOVA for concentrations of NAA/tCr, tCho, tCr, Glx/tCr, and mI/tCr within the 25 Gy cohort.

Time				
(0 months vs. 3 months)				
	df	***F***	***p***	η_p^2
NAA/tCr	1	0.665	0.565	0.399
tCho/tCr	1	0.148	0.766	0.129
Glx/tCr	1	3.062	0.330	0.754
mI/tCr	1	28392.250*	0.004	1.000
Hemisphere				
(Ipsilateral vs. Contralateral)				
	df	***F***	***p***	η_p^2
NAA/tCr	1	1.059	0.491	0.514
tCho/tCr	1	5.817	0.250	0.853
Glx/tCr	1	3.674	0.306	0.786
mI/tCr	1	14560.444*	0.005	1.000
Time x Hemisphere				
	df	***F***	***p***	η_p^2
NAA/tCr	1	12.045	0.179	0.923
tCho/tCr	1	1.417	0.445	0.586
Glx/tCr	1	0.448	0.624	0.310
mI/tCr	1	2.663	0.350	0.727

Table B.18. Results of a repeated measures two-way ANOVA for concentrations of NAA/tCr, tCho, tCr, Glx/tCr, and mI/tCr within the 15 Gy cohort.

Time				
(0 months vs. 3 months vs. 6 months)				
	df	***F***	***p***	η_p^2
NAA/tCr	2	2.222	0.310	0.690
tCho/tCr	2	1.07	0.483	0.517
Glx/tCr	2	1.116	0.473	0.527
mI/tCr	2	2.883	0.258	0.742
Hemisphere				
(Ipsilateral vs. Contralateral)				
	df	***F***	***p***	η_p^2
NAA/tCr	1	4.000	0.295	0.800
tCho/tCr	1	2.778	0.344	0.735
Glx/tCr	1	40.960	0.099	0.976
mI/tCr	1	0.274	0.693	0.215
Time x Hemisphere				
	df	***F***	***p***	η_p^2
NAA/tCr	2	1.762	0.362	0.638
tCho/tCr	2	4.160	0.194	0.806
Glx/tCr	2	0.041	0.961	0.039
mI/tCr	2	3.510	0.222	0.778

Table B.19. Results of a repeated measures two-way ANOVA for FA and ADC measurements within the 25 Gy cohort.

Time (0 months vs. 3 months)				
	df	***F***	***p***	η_p^2
Internal Capsule				
FA	1	1.409	0.289	0.220
ADC	1	1.787	0.239	0.263
Corpus Callosum				
FA	1	3.375	0.126	0.403
ADC	1	0.839	0.402	0.144
Hemisphere (Ipsilateral vs. Contralateral)				
	df	***F***	***p***	η_p^2
Internal Capsule				
FA	1	0.684	0.446	0.120
ADC	1	0.013	0.915	0.003
Corpus Callosum				
FA	1	7.606*	0.040	0.603
ADC	1	4.003	0.102	0.445
Time x Hemisphere				
	df	***F***	***p***	η_p^2
Internal Capsule				
FA	1	20.97*	0.006	0.807
ADC	1	5.498	0.066	0.524
Corpus Callosum				
FA	1	0.006	0.941	0.001
ADC	1	0.057	0.821	0.011

Table B.20. Results of a repeated measures two-way ANOVA for FA and ADC measurements within the 15 Gy cohort.

Time (0 months vs. 3 months vs. 6 months)				
	df	***F***	***p***	η_p^2
Internal Capsule				
FA	2	0.319	0.734	0.060
ADC	2	13.046*	0.002	0.723
Corpus Callosum				
FA	2	0.555	0.591	0.100
ADC	2	1.106	0.368	0.181
Hemisphere (Ipsilateral vs. Contralateral)				
	df	***F***	***p***	η_p^2
Internal Capsule				
FA	1	0.692	0.443	0.122
ADC	1	2.500	0.175	0.333
Corpus Callosum				
FA	1	0.870	0.394	0.148
ADC	1	1.590	0.263	0.241
Time x Hemisphere				
	df	***F***	***p***	η_p^2
Internal Capsule				
FA	2	1.701	0.231	0.254
ADC	2	2.720	0.114	0.352
Corpus Callosum				
FA	2	1.821	0.212	0.267
ADC	2	0.991	0.405	0.165